Technische Universität München
TUM School of Engineering and Design

A modular multi-fidelity scheme combining data-driven reduced order models for structural analysis under uncertainty

Catharina Julia Frederike Czech

Vollständiger Abdruck der von der TUM School of Engineering and Design der Technischen Universität München zur Erlangung einer

Doktorin der Ingenieurwissenschaften (Dr.-Ing.)

genehmigten Dissertation.

Vorsitz: Prof. Dr. ir. Daniel J. Rixen

Prüfer*innen der Dissertation:

1. Prof. Dr.-Ing. habil. Fabian Duddeck
2. Prof. Dr. Rob Hewson
3. Assoc. Prof. Dr. Joaquín Alberto Hernández Ortega

Die Dissertation wurde am 20.09.2023 bei der Technischen Universität München eingereicht und durch die TUM School of Engineering and Design am 01.02.2024 angenommen.

Abstract

In computational mechanics, deterministic parameters are commonly considered as input or boundary conditions. However, these are often simplifications of variables subject to random phenomena. When random variables significantly impact the system, probabilistic analyses inducing iterative procedures are employed to quantify their effect. Traditionally, the multi-query study repeatedly invokes the system solver with varying parameter configurations, which poses high and impractical computational expenses. Projection-based Model Order Reduction (MOR) techniques have been introduced to accelerate nonlinear Finite Element (FE) analysis. The approach assumes that an intrinsic subspace can represent the problem with fewer unknowns. For nonlinear problems, a snapshot-based method extends the physical system with data-driven strategies.

This thesis proposes a multi-fidelity scheme exploiting projection-based MOR for structural analysis. The architecture's key feature is the intertwining of intrusive and non-intrusive reduction methods. Both models are built in the same subspace, limiting the additional construction cost to a minimum. Moreover, the bi-fidelity scheme is tailored to double-loop algorithms, so analysis and optimisation under uncertainty can be performed efficiently.

The snapshot-based approaches evaluate FE training simulations through a Proper Orthogonal Decomposition (POD) to identify a reduced basis. In this new subspace, two models with significantly lower numbers of unknowns are established: the non-intrusive as the low-fidelity model and the intrusive representing the high-fidelity model. The non-intrusive MOR efficiently evaluates the coarse loop by a data-driven framework. The physics-based intrusive MOR technique is utilised to evaluate the second loop. Operating within the FE solver, the system of equations is first projected to the subspace and then solved in lower dimensions. An additional hyper-reduction step further reduces the computational effort of the intrusive model.

This thesis first compares intrusive and non-intrusive MOR techniques for crash simulations and their optimisations. To test the flexibility of the intrusive method, it is extended to statistically evaluate inhomogeneous material properties with the example of wood. Applying the proposed multi-fidelity framework in uncertainty propagation and robust design optimisation underlines the modular character.

Zusammenfassung

In einer numerischen Analyse werden Eingangs- oder Randbedingungen in der Regel als deterministische Parameter angenommen. Dabei handelt es sich häufig um Vereinfachungen von Variablen, die Zufallsphänomenen unterliegen. Wenn Zufallsvariablen, einen signifikanten Einfluss auf das System haben, werden iterative Verfahren aus der Probabilistik herangezogen, um deren Auswirkung zu bewerten. Allerdings führen die wiederholten Systemberechnungen mit variierenden Parameterkonfigurationen zu hohen und unpraktikablen Rechenzeiten. Um die Finite Elemente (FE) Modelle zu beschleunigen, werden projektionsbasierte Reduktionsmethoden in der Literatur eingeführt. Der Ansatz geht davon aus, dass ein intrinsischer Unterraum existiert, in dem das Problem mit weniger Unbekannten dargestellt werden kann. Für nicht-lineare Probleme werden Snapshot-Methoden verwendet, die den physikalischen Ansatz durch datenbasierte Methoden erweitern.

In dieser Arbeit schlagen wir ein *multi-fidelity* Schema vor, das zwei projektionsbasierte Reduktionsmethoden für strukturmechanische Probleme kombiniert. Die Verflechtung einer intrusiven und einer nicht-intrusiven Reduktionsmethode charakterisiert unsere neuartige Algorithmusarchitektur. Die reduzierten Modelle basieren dabei auf dem gleichen Unterraum, um deren Konstruktionskosten minimal zu halten. Des weiteren ist das Schema für Methoden mit zwei iterativen Schleifen zugeschnitten, damit Analysen und Optimierungen unter Unsicherheit effizient durchgeführt werden können.

Um eine passende reduzierten Basis zu identifizieren, werden Trainingssimulationen mittels *Proper Orthogonal Decomposition* ausgewertet. Auf diesem neuen Unterraum basieren zwei reduzierte Modelle: das nicht-intrusive als *low-fidelity* Modell und das intrusive als *high-fidelity* Modell. Die nicht-intrusive Modellreduktion ergibt ein datengesteuertes Ersatzmodell, das die erste Iterationsschleife effizient auswertet. Der physikalische intrusive Ansatz wird zur Bewertung der zweiten Schleife verwendet. Dazu projiziert der FE Algorithmus das Gleichungssystem zunächst auf den reduzierten Unterraum, um es in einer kleineren Dimension zu lösen. Ein zusätzlicher Hyper-Reduktionsschritt optimiert den Rechenaufwand des intrusiven Modells weiter.

Diese Arbeit vergleicht zunächst intrusive und nicht-intrusive Projektionstechniken für Crashsimulationen und deren Optimierung. Der intrusive Ansatz wird am Beispiel von Holz für inhomogene Materialeigenschaften erweitert, um die Flexibilität der Methode zu testen. Darüber hinaus unterstreicht die Anwendung des vorgeschlagenen *multi-fidelity* Schemas in einer Unsicherheitsanalyse und in einer robusten Optimierung den modularen Charakter.

Contents

Part I

Introduction

Chapter 1

Introduction

1.1. Motivation

Nowadays, the engineering world provides a great variety of digital tools and numerical methods to create and improve structural design. For structural mechanics, the Finite Element (FE) method is a highly popular numerical tool to analyse the mechanical behaviour of structures. Detailed FE models have been developed over the last decades to understand the mechanical responses of designed products. This was enabled by the steady rise in computational resources that allowed for increasingly large-scale, highly detailed, and complex mechanical simulations. To help engineers in the design process, additional methods have been developed around the classical FE analysis. For example, optimisation algorithms find an optimal design under the variation of certain design variables. Other tools, originating from statistical theories, enable engineers to safely handle present uncertainties, such as small variation due to production imprecision. These types of studies induce an iterative evaluation of the original FE model, also called multi-query analysis, under certain parameter variations.

This thesis will be based around the topic of Model Order Reduction (MOR) in the scope of iterative analysis due to uncertainties. In general, MOR techniques try to reduce the order of dimensions, consequently lowering the computational costs. The reader could question why model order reduction is still necessary if computational power constantly improves. Therefore, the topic is motivated by a practical example on the subject of vehicle safety.

Figure 1.1 Human Body Model (THUMS, version 5, (Iwamoto et al, 2002)) in a frontal impact situation (Uriot et al, 2015) analysed with LS-Dyna to investigate submarining (Go, 2021).

Crash simulations have become an integral part of vehicle safety design, which places Human Body Models (HBMs) in the car to analyse potential injuries. For frontal impacts, the lab seat belt can slip over the pelvis causing injuries to the hollow abdominal organs. To explain the phenomenon, Fig. 1.1 shows an HBM with the desired behaviour on the left and a critical position of the lab seat belt on the right. This condition, also known as submarining, can occur in reclined seating positions, either due to comfort requirements or in autonomous driving vehicles. However, submarining is difficult to predict, as it can appear under a combination of different conditions. Multiple co-depending influences between the human and the design of the seat and airbag affect the phenomenon. As safety is to be ensured for people with different physiques and ages, also deviating from the classic HBM model, further investigations are essential.

These uncertainties require an iterative study to investigate the combination of critical parameters to quantify the risk of submarining. As an example, we refer to Go et al (2023), where the influence of six parameters on an average male HBM is analysed with FE simulations. The already simplified HBM model is discretised with a mesh consisting of around $50,000$ nodes, resulting $1,500,000$ unknowns. To solve the system of equations, the processing time is approximately 20 minutes when distributed among 36 CPUs, which is common in an industrial environment. For a single analysis, this seems reasonable; however, for the high-dimensional parameter study, a few hundred simulations are required, leading to days of computing time. Such a high processing effort is unpractical, and techniques to reduce computational costs are required.

This is a realistic setting where engineers work on already available large-scale models, such as the open source HBM mentioned above. The FE analysis is highly complex, as non-linear material and large deformations must be considered. In addition, contact formulations are included, which further increase the computation time of the explicit FE analysis. The described problem exemplarily pictures the need for reduced order models in the context of multi-query analysis for large-scale and nonlinear models in structural analysis.

1.2. State of the art

In the literature, an extensive number of papers have been published on MOR. As a general and quite popular keyword, many different techniques can be found. Especially the distinction between approaches suitable for linear or nonlinear problems is not always clear at first sight. For related MOR techniques the interested reader is referred to Benner et al (2015) for an overview of parametric MOR and to Hesthaven et al (2022) for a summary suitable for transient analysis. Moreover, the collection of Benner et al (2021a,b,c) includes a large variety of MOR topics. The following paragraphs name only closely related publications and summarise similar techniques to the author's best knowledge.

In previous years, projection-based reduced order models have been identified to efficiently decrease computation time. A reduced space is constructed with a snapshot-based approach, utilising previously computed FE simulations. It combines knowledge extracted from available data with classical numerical analysis, following the trends of machine learning. This thesis addresses the practical application of data-driven and projection-based model order reduction. The selected methods are based on a linear projection method, in which the so-called snapshot matrix is reformulated via Proper Orthogonal Decomposition (POD) to identify a reduced basis (Sirovich, 1987). We apply an intrusive MOR scheme using the Galerkin projection to transform the system of equations into the reduced space. A hyper-reduction step further reduces the system via the Empirical Cubature Method (ECM) (Hernández et al, 2017) or Energy Conserving Sampling and Weighting Technique (ECSW) technique (Farhat et al, 2014). Additionally, a non-intrusive approach that combines the identified basis vectors with a weighted sum employing a regression model has been selected (Guo and Hesthaven, 2017; Swischuk et al, 2019; Yu et al, 2019; Kast et al, 2020). By Hesthaven et al (2022), this technique was named proper orthogonal decomposition with interpolation.

Reduced order models are primarily designed to decrease the computational effort for numerical analysis. To create the reduced models employed in this thesis, a construction phase is required, which is associated with upfront costs. In fact, the training phase includes full-order simulations for snapshot-based MOR techniques. These upfront costs are justifiable if the focus is on very fast real-time simulation, where offline costs are irrelevant, or if the model is evaluated repeatedly in an iterative process. This thesis concentrates on the latter, the application of reduced order models for many-query or multi-query analysis. Moreover, the focus lies on the efficient application rather than the construction of the models. We are particularly interested in combining intrusive and non-intrusive schemes to form efficient analysis under uncertainty. Therefore, a multi-fidelity architecture based on varying MOR levels shall be constructed.

To introduce multi-fidelity frameworks, Peherstorfer et al (2018) reviews varying concepts for

multi-fidelity schemes in double-loop algorithms. In particular, uncertainty propagation, inference, and optimisation are identified as useful applications. We follow these ideas and focus on uncertainty propagation and optimisation under uncertainties.

Different model managements combining high-fidelity and low-fidelity models can be categorised. The concepts are classified with adaptation, when a low-fidelity model is improved through a high-fidelity model, fusion, a combination of high- and low-fidelity models, and filtering, where a high-fidelity analysis is invoked by a low-fidelity model. In classically multi-fidelity schemes for FE analysis, a low- and high-fidelity are created with varying mesh resolutions. However, in Peherstorfer et al (2018) it is stressed that the concepts are applicable to more general fidelity schemes, such as MOR or models based on simplified physical assumptions.

In the following, we summarise multi-fidelity approaches utilising similar reduced order models, mainly focusing on POD-based techniques. A larger literature block corresponds to Multi-fidelity Models (MFMs), which create a single surrogate based on the results of different fidelity models. Afterwards, we name publications that use multi-fidelity and MOR-based architectures for uncertainty propagation. A review of related approaches for optimisations and optimisation under uncertainties finalises the literature review. The publications differ mainly in the combination of methods and their application. Therefore, the following paragraphs present an overview of available ideas rather than a progressive development of a single concept.

Multi-fidelity models

A closely related line of research investigates MFM, which incorporates high- and low-fidelity models to create a single non-intrusive surrogate. Therefore, the same model management principles are applicable (Khatouri et al, 2022). It must be stressed that we are not interested in MFM, but rather in building a framework using high- and low-fidelity models. This distinction is not always clearly visible, and therefore a few interesting approaches are named. A popular MFM is Gaussian process regression due to its inherent statistical properties. For example, cokriging (Kennedy and O'Hagan, 2000) or one of its further advances, such as hierarchical kriging (Han and Görtz, 2012), is often employed for optimisation problems. Typically, an adaptive refinement strategy improves the surrogate during the optimisation procedure.

In this class, MFM using projection-based methods have also been developed. A multi-fidelity surrogate based on gappy POD can be found in Toal (2014), which is applied to uncertainty propagation and optimisation. Unlike the POD with interpolation employed in this thesis, the gappy POD approach approximates the missing high-fidelity results using low-fidelity data. Sella et al (2023) investigate three multi-fidelity regression models for non-intrusive MOR, linearly combining a weighted reduced basis. Here, the high- and low-fidelity models are FE analyses with varying mesh resolution. As the publication investigates very sparse data, a bi-fidelity Kennedy-O'Hagan approach and data augmentation techniques are tested for the approximation of a surface pressure field. Instead of a linear regression model, Lu and Zhu

(2021) use a neural network in a similar framework. A neural network trained with high-fidelity analyses has additional features extracted from the low-fidelity model.

Kast et al (2020) apply a multi-fidelity scheme for the construction of the reduced basis, whereby the low-fidelity model helps to indicate valuable snapshot locations, then evaluated by the high-fidelity model. The multi-fidelity idea is also used in the online stage, where a cokriging algorithm is combined with the previously identified reduced basis. The non-intrusive technique is evaluated for different low-fidelity models either using a lower number of elements or a linearised solver for the structural problem under large deformations. This is in contrast to Guo et al (2022), where the high-fidelity is a full-order FE analysis and the low-fidelity model is created with an intrusive MOR technique. Here, a multi-fidelity neural network is enriched with the hyper-reduced model using the Discrete Empirical Interpolation Method (DEIM) algorithm.

In a consecutive publication by Conti et al (2023) this parametric model is extended to dynamic analysis through short-term memory networks. Such techniques belong to scientific machine learning, which also employs multi-fidelity approaches. For example, multi-fidelity deep operator networks (Lu et al, 2022), applied to optimisation studies, or multi-fidelity convolutional autoencoder (Partin et al, 2023) have been developed. Often, the additional low-fidelity model is used to extend the training set for sparse data regimes, e.g. with transfer learning approaches (Song and Tartakovsky, 2021). An interesting application shows Tao and Sun (2019), using a multi-fidelity deep learning approach for robust aerodynamic design optimisation or Balokas et al (2021), which applies a multi-fidelity neural network to quantify uncertainties of nonlinear braided composites. Interested readers can refer to Khatouri et al (2022), which presents an extensive list of MFM mainly focusing on aerospace applications.

Multi-fidelity schemes for uncertainty propagation

Next, we concentrate on multi-fidelity architectures combining multiple separate models of varying fidelity instead of one MFM surrogate. Returning to analysis under uncertainties, we first focus on uncertainty propagation based on multi-fidelity architecture. In the scope of uncertainty propagation Monte Carlo (MC) based sampling strategies are commonly used for nonlinear problems. As a prominent multi-fidelity scheme, the concept of control variate estimators has been adapted using high- and low-fidelity models, also known as Multi-fidelity Monte Carlo (MFMC) (Ng and Willcox, 2014). This evolved from the concept of multilevel MC, where hierarchical models with varying mesh resolution are invoked to estimate statistical properties. An overview of recent advances on MFMC, such as Gorodetsky et al (2020), and its closely related multi-level MC is given in Zhang (2021).

We are interested in reduced order models in the scope of control variate estimators. Early publications use a reduced basis method, which is built by greedy algorithms for control variates (Boyaval et al, 2009; Boyaval, 2012). We refer the interested reader to Chen et al (2017)

for an overview of reduced basis methods in Uncertainty Quantification (UQ). In González et al (2019) control variate estimators with a non-intrusive MOR technique are constructed as a low-fidelity model for time-invariant, linear problems. There, the reduced basis is not generated with the help of snapshots, but using model derivatives.

Moreover, the MFMC approach was extended to the optimal model management strategy that defines the number of high- and low-fidelity simulations with the solution of an optimisation problem (Peherstorfer et al, 2016). In Blonigan et al (2020) the optimal hyperparameter of an intrusive Pertrov-Galerkin projected model is investigated by applying the optimal model management scheme.

Multi-fidelity schemes for optimisation

The original publication of Ng and Willcox (2014) in fact applies MFMC within the scope of optimisation under uncertainties. Control variate estimators are used to accelerate the computation of the variance criterion, quantifying the influence of uncertain parameters. This leads to the investigation of similar projection-based MOR techniques within the scope of optimisation. An optimisation study using intrusive MOR has first been proposed by Amsallem et al (2015a). The shape of a rocket nozzle, discretised by finite differences, has been projected and hyper-reduced via gappy POD. An additional approximation of the objective function by radial basis is introduced for quantities lost within the hyper-reduction step. The optimisation problem is successfully solved by a sequential quadratic programming method.

In Scheffold et al (2018) a vibration frequency optimisation of jointed structures under contact was performed. The utilised model is created based on Galerkin projection and hyper-reduction via ECSW. Another design optimisation that combines POD-based, intrusive MOR with an equivalent static load approach can be found in Lee and Cho (2018). Here, the proper orthogonal modes of the external load are considered to define a parameterisation of the reduced order model.

Projection-based models have been incorporated within a trust region optimisation using adjoint methods (Zahr and Farhat, 2015; Zahr et al, 2019). The publications investigate optimisation under uncertainties, whereby the uncertainties are estimated with stochastic collocation based on dimension-adaptive sparse grids. A recent publication also includes the adaptive construction of a hyper-reduced model for shape optimisation (Wen and Zahr, 2023).

A two-step optimisation technique by Li et al (2018) has a comparable idea of reusing the snapshots within an intrusive and non-intrusive approach. Here, the optimisation is divided into two steps to find the minimum. The non-intrusive MOR is based on kriging with interpolative POD applied within a generic optimisation algorithm. In the consecutive step, the optimum is found with an adjoint method using an intrusive Petrov-Galerkin projected model; however, no hyper-reduction is applied. An additional domain decomposition method divides the flow

analysis of an airfoil into sensible and insensible areas, whereby only the insensible ones are reduced.

As different combinations of bi- and multi-fidelity approaches have been proposed in the literature, efficiency improvement through varying fidelity models seems promising. Non-intrusive MFMs have shown that a low-fidelity model can enrich the training process to improve the surrogate. Here, we want to investigate schemes mainly based on intrusive MOR approaches and evaluate their performance in multi-query settings for structural parametric problems. Transferring the idea to intrusive MOR, a multi-fidelity architecture, is a promising model management strategy. We want to keep the expensive construction cost of the reduced order models to a minimum. Therefore, reusing snapshots, as the decisive cost within the construction phase, is beneficial. So far, primarily multi-fidelity architectures tailored to specific examples have been developed, such as Li et al (2018). However, we are interested in a general workflow for different kinds of double-loop problems based on a modular arrangement.

1.3. Research objectives

In the development process of novel model order reduction techniques, many publications start with the reduction of a single analysis. However, a meaningful implementation for iterative studies must include a parameter space for which the reduced model is applicable. Therefore, this thesis focuses on parametric reduced order models in the scope of structural multi-query analysis such as uncertainty quantification, robustness analysis, and optimisation studies. Throughout the thesis, two groups of research questions are formulated. The first one discusses the trade-off between accuracy and efficiency for projection-based intrusive MOR methods in the scope of challenging nonlinear structural design problems. Developing a multi-fidelity scheme to further improve efficiency gains is the second research objective. In this context, a general MOR scheme based on multiple fidelity levels is proposed.

With regard to the first research aim, the overall performance, which involves the construction and execution step, is examined for parametric analyses. Therefore, we focus on the parameter space and evaluate its effect on the reduced order models. The inter- and extrapolation capabilities in the parameter space, as well as an optimisation study, investigate the performance of projection-based intrusive MOR in a practical setting.

In order to better assess the intrusive MOR method, it is compared to a non-intrusive technique which belongs to the field of surrogate models. The non-intrusive MOR approach is based on the identical subspace projection; however, it replaces the system operators by a purely data-driven regression model. The costs associated with the regression analysis are strongly reduced, along with a lower level of precision. To reach a comparable accuracy level, the non-intrusive model requires higher initial construction costs than the intrusive counterpart.

For this purpose, the construction costs are shown in correlation to the processing time of the reduced order models, and the number of model evaluations leading to overall speedups is identified. The comparison of both techniques shall give the reader a better understanding of the potential and limits of projection-based model order reduction.

It is investigated whether the intrusive MOR approach can be extended to the nonlinear analysis of inhomogeneous materials. Therefore, a workflow to create reduced order models for spatially varying material properties is proposed. The parameter space is modelled with random processes, and its effect on the reduced order models is highlighted with varying examples. In the online phase, we quantify the effects of the uncertainties with the help of probabilistic methods. Leading to a quantification of uncertainties via reduced order models, the efficiency improvements are analysed. Moreover, the applicability in terms of a low Kolmogorov n-width is investigated for the structural example to show the limits of classical linear projection.

In summary, **the applicability and performance evaluation of intrusive MOR in the scope of structural analysis under uncertainties and optimisation** is the first aim of this thesis. The following objectives can be summarised to investigate the corresponding research questions:

- Investigating the benefits and drawbacks of intrusive MOR for parametric nonlinear structural problems;
- Contrasting intrusive MOR to the non-intrusive approach by a detailed analysis of offline and online costs for structural optimisation;
- Extending the intrusive MOR approach to analyses of spatial uncertainties;
- Revealing the limitations of global POD for low Kolmogorov n-width problems in structural applications;
- Showing the reader in different practical applications, such as crashworthiness and natural fibre composites, the achievable balance between accuracy and speedups.

The second research objective concerns the development of a novel multi-fidelity scheme based on varying levels of reduced order models. Therefore, we explore the feasibility of a general multi-fidelity scheme for analysis and optimisation under uncertainty on the basis of MOR.

In Chapter 4 we propose a method that merges intrusive and non-intrusive projection-based approaches to a multi-fidelity architecture. The main idea is that with the intrusive model at hand, a complementary non-intrusive model can enhance the overall analysis with limited additional cost and implementation complexity. The training phase is discussed, and links to the methods introduced in the background theory are created. A detailed workflow description

of the application phase highlights the options between varying reduced order models and shows the full range of the proposed schemata.

Furthermore, this thesis discusses how the non-intrusive scheme can be ideally linked to the intrusive technique. Exploiting the snapshot-based approach, the non-intrusive model can constantly be improved through newly available high-fidelity analyses. During this iterative procedure, the low-fidelity model is continuously updated so that its correlation to the high-fidelity model is enhanced, and thus its approximation quality. The main benefit is attributed to the low costs of a non-intrusive model, which can consequently improve the overall efficiency gains.

To showcase the multi-fidelity scheme, the application to optimisation and analysis under uncertainties is proposed. Both schemes result in double-loop algorithms, which are especially expensive to perform. The general multi-fidelity scheme is therefore specified for a robust optimisation and uncertainty propagation using control variate estimators. The two specific analysis schemes are from different research fields to underline the modular aspect of the proposed architecture. The uncertainty quantification is based on MC simulations performed by the intrusive model. The non-intrusive model is integrated through the extension of control variate estimators, requiring a low-fidelity model. Thus, the estimator for variance and mean can be enhanced by a high number of non-intrusive analyses, as they add relatively little computational cost. This results in a double-loop algorithm utilising two fidelity levels, a common attribute with the optimisation procedure. For optimisation under uncertainties, a robustness criterion is introduced. The robustness criterion requires an additional loop in each iteration step to evaluate the variance of the performance parameter. Comparable to the uncertainty propagation, the first loop is performed by the intrusive MOR and complemented by a second analysis loop using non-intrusive techniques.

Example studies are presented in Chapters 7 and 8, to assess the outlined multi-fidelity scheme. For uncertainty propagation, the control variate estimators are demonstrated with varying choices for high- and low-fidelity models. Accuracy levels are compared, and overall efficiency gains are assessed to judge the multi-fidelity scheme. In addition, studies based on the multi-fidelity optimisation algorithm show its general applicability. The differences between absolute and robust minima are highlighted and it is shown that the proposed multi-fidelity workflow converges to the robust minima with reduced computational effort. With a final optimisation study, we showcase the potential efficiency gains of the proposed method for large-scale problems.

To summarise the previous paragraphs, the following aim and objectives can be formulated. The **development of a multi-fidelity scheme exploiting multiple levels of projection-based reduced order models** is the second research aim, which is implemented with the merged objectives:

- Proposing a multi-fidelity MOR method for highly cost intensive analysis, especially beneficial for robust design studies with double-loop algorithms;
- Development of a bi-fidelity scheme by enhancing the intrusive model with a non-intrusive surrogate;
- Adaptive construction of the snapshot-based non-intrusive model by a retraining scheme ideally utilising the iterative enlarged data set;
- Evaluation of the multi-fidelity scheme for analysis and optimisation under uncertainties with multiple structural nonlinear problems.

1.4. Associated publications

The following paragraph summarises the associated publications for this thesis. In Czech et al (2022b) the intrusive and non-intrusive MOR scheme is compared and applied to crash simulations and an optimisation study. Moreover, Czech et al (2022a) propose the multi-fidelity MOR for robust optimisation, also introduced in this thesis. If the content originates from one of the papers, a clear statement is given in the introduction of the corresponding chapters.

In multiple collaborations, the non-intrusive scheme was applied in parameter and optimisation studies, which are only briefly referred to during the script. In Pretsch et al (2023) the non-intrusive MOR techniques predict the pressure field in a multidisciplinary design optimisation for turbine blades. Within a multi-fidelity approach based on hierarchical kriging, the non-intrusive technique was used for crashworthiness optimisation (Kaps et al, 2022). Another application of the non-intrusive scheme is the parameter study of Human Body Models in Go et al (2023).

1.5. Thesis outline

Corresponding to the research objective, the thesis is structured in three main parts: the theoretical back ground, the proposed multi-fidelity algorithm, and the application chapters. First, we introduce the theoretical background required to understand the proposed methods. It is a compact introduction of relevant concepts which are essential for the following ideas and the studies conducted.

- *Chapter 2* introduces uncertainty analysis, starting with the basic concept of random variables and processes, introducing the idea of robustness analysis, followed by sample-based uncertainty propagation and robust optimisation.
- *Chapter 3* presents projection-based reduced order models for structural analysis with snapshot-based POD projection, utilised for intrusive Galerkin projection extended by hyper-reduction, and regression-based non-intrusive techniques.

The novel multi-fidelity method based on model order reduction for analysis under uncertainties is introduced in *Chapter 4*.

Next, application studies illustrate the presented reduced order models for analysis under uncertainties, in particular robustness studies.

- *Chapter 5* applies intrusive and non-intrusive MOR to crashworthiness analysis to compare and evaluate its inter- and extrapolation capabilities.
- *Chapter 6* proposes intrusive MOR for the quantification of spatial uncertainties, such as required for natural fibre composites.
- *Chapter 7* shows the proposed multi-fidelity scheme in the scope of uncertainty propagation via control variate estimators.
- *Chapter 8* highlights the multi-fidelity scheme for robust optimisation studies.

To conclude the presented work, *Chapter 9* summarises the results, including a critical reflection, and gives ideas for future work.

Part II

Background theory

Chapter 2

Structural analysis and optimisation under uncertainties

This chapter provides the theoretical background for analysis and optimisation under uncertainties, in the context of this thesis. Therefore, the basic techniques employed for this contribution are summarised from literature. To provide a comprehensive explanation, relevant methods are introduced and accompanied by further literature references. We represent a summary of the applied methods and do not show a comprehensive overview of the broad field of optimisation and analysis under uncertainties. In order to understand the connection between the selected techniques, the first section gives a brief introduction and establishes the relation between the individual theoretical sections.

2.1. Introduction to analysis and optimisation under uncertainties in structural mechanics

In classical structural analysis, we consider design parameters such as material properties or loading conditions as deterministic. However, on closer inspection, these deterministic values are often a simplification of variables under uncertainty. Especially when considering environmental effects, the deterministic assumption can become unreasonable. For example, in a naturally grown material such as beech wood, the scatter of strength values is so high that the conservative approach of selecting the worst-case scenario drastically underestimates its potential capacity (Kandler et al, 2018). In structural engineering, multiple factors can lead to analyses under uncertainty. Typically, a variation in loading conditions or a scattering of material properties through growth, production, or deterioration can induce critical uncertainties.

Another reason for performing a statistical analysis could be tolerances or imperfections in geometric shape and dimensions. In the following chapter, the relevant theoretical background for analysis and optimisation under uncertainties is presented.

In uncertainty quantification, one commonly starts with the classification of uncertainties by its origin. We differentiate between aleatoric uncertainties, which refers to an intrinsically random phenomenon, and epistemic uncertainties, describing a lack of knowledge. In this thesis, we focus on a probabilistic representation of aleatoric uncertainties and refer to Acar et al (2021); Beyer and Sendhoff (2007) for a detailed comparison of other uncertainty handling, such as possibility theory, interval approaches or fuzzy methods. The chosen techniques belong to the field of uncertainty quantification, which bridges mathematical probability theory with statistical practise (Sullivan, 2015). Section 2.2.1 introduces the concept of random variables and functions that define a parameter with statistical properties such as its probability distribution.

If a single independent random variable is not sufficient to describe the present phenomena, a set of random variables or a random process can be introduced. Section 2.2.2 explains random processes, a random function dependent on a parameter, to describe spatial or time dependencies. This concept is applied to spatial uncertainties in the scope of numerical analysis, as presented in Section 2.3 about random fields. We will focus on Gaussian normal distribution, as the specific nature of the random variables is not the primary interest in this work.

The main interest lies in forward problems, where the effects of input uncertainty on performance variables are studied (Sullivan, 2015). There are different methods to compute the effect of random input parameters on output parameters (Acar et al, 2021). In the following, we will focus on techniques applicable to robustness analysis. A robust design should be insensitive to uncertain design parameters and characterised by a low variability of the performance. A short overview of robustness measures is given in Section 2.4, which can be contrasted with the reliability of a design. Expectancy and dispersion measures are explained in Section 2.4.2, which aims to find the probability distribution of the output variables.

For this work, two specific analyses under uncertainties have been chosen: MC analysis with control variate and robust design optimisation. Both techniques use variance-based measures to evaluate robustness. As the focus lies on nonlinear problems, we apply sampling strategies to solve the probability density integral, such as the highly popular MC analysis. In Section 2.5 the MC analysis with control variate evaluates the probability distribution of a performance quantity based on a multi-fidelity analysis. In addition to the classical MC analysis, a low-fidelity model is introduced in a second loop to avoid high sampling costs. For the second type of analysis, an optimisation strategy to find a robust optimum is described in Section 2.6. To

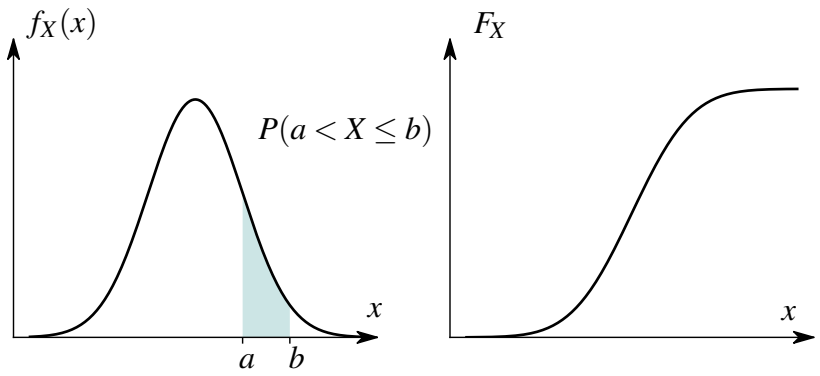

Figure 2.1 Properties of Gaussian normal distribution variable $X \sim N(\mu_X, \sigma_X)$ defined by mean μ_X and standard deviation σ_X: PDF, $f_X(x)$ on the left and CDF, F_X on the right.

achieve a robust design, the variance of the objective function is computed using a two-loop algorithm.

Both analyses, MC simulation with control variate and robust optimisation, result in multi-query or many-query simulations, which suffer from very high or even unfeasible computational costs. The double loop algorithm can be well combined with multi-fidelity schemes, which strongly increases its computational efficiency (Peherstorfer et al, 2018). To enable such multi-query analysis, an efficient implementation with reduced models is proposed in Chapter 3.

2.2. Concept of random variables and processes

In the following section, the concepts essential to random variables and processes with normal distribution are presented. We mainly follow the explanation of Papaioannou (2020), which is based on the book of Grigoriu (2002). With knowledge of Gaussian processes, the theory of random fields is introduced in Section 2.3. It also provides the background knowledge for Section 3.4.3 on Gaussian processes regression.

2.2.1. Random variables

In probability theory, a parameter with statistical properties is called a random variable X, indicated with an uppercase letter. A random variable X with $X : S \to \mathbb{R}$ of the sample space S can be observed as the outcome $X = x$. In other words, the possible values of the random variable X, are denoted by lowercase x and collected in the sample space S. An event is a subset of S. To describe the probability P for the occurrence of an event, a probability distribution is used.

We focus on continuous variables X leaving aside the discrete version of X. The character of a continuous random variable X can be quantified with Probability Density Function (PDF) and Cumulative Distribution Function (CDF). Figure 2.1 shows an example PDF on the left and its corresponding CDF denoted by F_X, on the right.

The CDF is the probability of the event $\{X \leq x\}$, such that a random realisation of X is less than the outcome x

$$F_X(x) = P(X \leq x). \tag{2.1}$$

On the other hand, PDF considers the interval between the realisation a and b and is defined as

$$\int_a^b f_X(x)dx = P(a < X \leq b) = F_X(b) - F_X(a), \tag{2.2}$$

with the following properties:

$$f_X(x) \geq 0, \qquad \int_{-\infty}^{\infty} f_X(x)dx = 1, \qquad F_X = \int_{-\infty}^{x} f_X(z)dz. \tag{2.3}$$

Note that the probability $P(X = x)$ is only computed for the discrete case of X and equals zero for a continuous variable. For this reason, the PDF is introduced, which is the integral of a probability.

In general, we are interested not only in random variables, but in functions $g(X)$ that depend on a random variable X. Therefore, the mathematical expectation $E[g(X)]$ is introduced as

$$E[g(X)] = \int_{-\infty}^{\infty} g(x) f_X(x)dx. \tag{2.4}$$

The expected or mean value μ_X is the first statistical moment and can be defined with

$$\mu_X = E[X]. \tag{2.5}$$

The second central moment gives the variance V as

$$\mathrm{V}(x) = {\sigma_X}^2 = E[(X - \mu_X)^2], \tag{2.6}$$

which represents a measure of dispersion. In engineering applications, the standard deviation, defined as the square root of the variance $\sigma_X = \sqrt{V(x)}$, is often used.

Next, the attributes of Gaussian random variables, frequently used in engineering and shown in Fig. 2.1, are specified. For a summary of other popular distributions, we refer to (Fishman, 1996). A normal random variable follows $X \sim N(\mu_X, \sigma_X)$ and is defined with mean μ_X and standard deviation σ_X. The corresponding $f_X(x)$ is stated by the equation below:

$$f_X(x) = \frac{1}{\sigma_X \sqrt{2\pi}} \exp\left[-\frac{(x - \mu_X)^2}{2{\sigma_X}^2}\right]. \tag{2.7}$$

With these basic concepts on random variables, we conclude the section and refer to text

books such as Fishman (1996); Grigoriu (2002); Sullivan (2015) for a comprehensive introduction.

2.2.2. Gaussian processes

A Gaussian process is formally defined as 'a collection of random variables, any finite number of which have a joint Gaussian distribution' by Rasmussen and Williams (2006) and can be completely defined by its mean and covariance function.

A Gaussian process comprises a collection of random variables that can be expressed by a random vector $\mathbf{X} = [X_1, X_2, ..., X_d]$ of dimension d. In the second part of the definition, the term 'multivariate joint Gaussian distribution' is introduced. The distribution of multiple random variables, for example the random variable X_i and X_j can be represented by its joint distribution. The probability $P(X_i, X_j)$ of the occurrence of the joint event $\{X_i \leq x_i \cap X_j \leq x_j\}$ is denoted by the bi-variate joint CDF. The bi-variate distribution refers to two dimensions, while the multivariate joint distribution applies to any d-dimensional random vector.

The jointly modelled random variables can also be quantified by the covariance metric Cov. It is the counterpart to the variance for multidimensional cases and describes the linear dependence of a random variable X_i to X_j, such as

$$Cov[X_i, X_j] = E[(X_i - \mu_i)(X_j - \mu_j)]. \tag{2.8}$$

If $Cov[X_i, X_j] = 0$ the random variables are uncorrelated, whereas for $Cov[X_i, X_j] = 1$ they are fully correlated. A dimensionless correlation coefficient ρ_{ij} is the covariance normalised by its standard deviations $\rho_{ij} = \frac{Cov[X_i, X_j]}{\sigma_i \sigma_j}$.

Our main interest lies in random processes, so far only random variables and vectors have been introduced. A random process is a function $X(z)$ indexed by a parameter $z \in \Omega$. The parameter z could describe a time or space dependency in the domain Ω. Similarly to the definition of random variables, $x(z)$ is a realisation or outcome of the random process $X(z)$. Moreover, the function $X(z_i)$ evaluated for every $z_i \in \Omega$ gives a random variable. If Ω is a finite set, in other words a vector $\mathbf{z} \in \Omega^n$ the random process results in a random vector $[X(z_1), X(z_2), ..., X(z_n)]^T$.

For two variables $\mathbf{z}, \mathbf{z}' \in \Omega$ the auto-covariance function is defined as

$$R_{XX}(\mathbf{z}, \mathbf{z}') = E[(X(\mathbf{z}) - \mu_X(\mathbf{z}))(X(\mathbf{z}') - \mu_X(\mathbf{z}'))]. \tag{2.9}$$

Whereby, the covariance function

$$\kappa(\mathbf{z}, \mathbf{z}') = E[X(\mathbf{z})X(\mathbf{z}')], \tag{2.10}$$

is equal to the auto-covariance function if the mean function is zero. Then, a Gaussian random process can be completely described by mean $\mu_X(\mathbf{z})$ and covariance function $\kappa(\mathbf{z},\mathbf{z}')$:

$$f(\mathbf{z}) \sim GP(\mu_X(\mathbf{z}), \kappa(\mathbf{z},\mathbf{z}')). \tag{2.11}$$

For stationary processes, also called homogeneous processes, it is assumed that the mean $\mu_X(\mathbf{z}) = {\mu_X}^0$ is constant.

2.3. Modelling of spatial uncertainties with Gaussian random fields

To model spatially varying properties, the concept of random fields has been developed. The comprehensive book of Vanmarcke (2010) summarises the methods affiliated to random fields and applies them to the in-depth material variation of soil profiles for civil engineers.

2.3.1. Spatial uncertainties

Random field and random process, as defined in Section 2.2.2, are synonyms, although the term random field is mostly used for spatial problems. This implies that a random function $X(\mathbf{z})$ referring to Eq. (2.11) depends on the spatial coordinates $\mathbf{z}$ of a one-, two-, or three-dimensional problem. In the following, a random field will be denoted by $H(\mathbf{z},\theta)$ to highlight its dependency on random phenomena indicated by θ. Moreover, the correlation function as explained below describes the spatial correlation of the uncertain parameter. This is in contrast to, e.g. Gaussian process regression where the kernel represents the correlation of arbitrary data points. In addition, the discretisation of random fields via Karhunen Loève (KL) expansion is briefly described, so that the analytical formulation of random fields is applicable within a numerical framework. We restrict ourselves to stationary Gaussian random fields with a normal distribution of $X \sim N(\mu_X = 0, \sigma_X = 1)$.

2.3.2. Correlation function

Commonly, the correlation function exploits a relative distance measure to describe spatial dependencies. To compute the correlation function, the covariance function of Eq. (2.10) is normalised by the standard deviation. The correlation is $0 \leq C(z_i,z_j) \leq 1$, so that the fully correlated points have a correlation of one. Multiple different correlation characteristics are available, for example, an exponential correlation function could be formulated:

$$C(z_i,z_j) = \exp\left(-\frac{||z_i - z_j||^2}{l_c^2}\right), \tag{2.12}$$

with the distance $d = ||z_i - z_j||$ between two arbitrary points z_i and z_j and the dimensionless correlation length l_c. We assume an isotropic kernel such that the correlation length is equally defined in all dimensions. The choice of correlation length depends greatly on the specific

problem. To illustrate the effect of the correlation length, Fig. 2.2 shows three realisations of a random field with an exponential correlation function of Eq. (2.12) and two varying correlation lengths. Influenced by the outcome of the random function, each realisation results in a different curve, however, the effect of a higher and lower value of l_c is clearly visible when comparing the left and right graph.

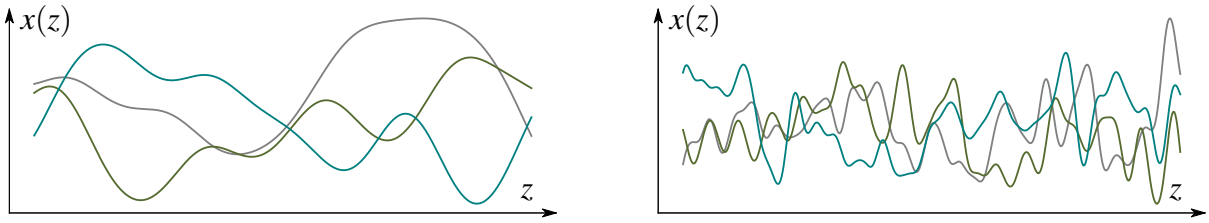

(a) Three realisations $x(z)$ of a random process with correlation length $l_c = 10$.

(b) Three realisations $x(z)$ of a random process with correlation length $l_c = 2$.

Figure 2.2 One-dimensional random field with exponential correlation function and two different correlation lengths.

2.3.3. Discretisation of Gaussian random fields

In general, random fields are continuous quantities, but must be discretised for computational use in FE analysis (Vanmarcke, 2010). For an overview of discretisation methods, we refer to Sudret and Der Kiureghian (2000). Here, the KL expansion is chosen, which utilises the orthogonal eigenvectors of the auto-covariance function. The numerical solution of the KL expansion follows Betz et al (2014) and is here only summarised.

As the KL expansion is a series expansion, the continuous random field, $H(\mathbf{z},\theta)$, shall be created by a set of shape functions ϕ and a random vector $\mathbf{b}$ (Li and Der Kiureghian, 1993). Thus, $\mathbf{b}(\theta)$ contains random variables that must be uncorrelated to ensure unbiased results. It reads as

$$H(\mathbf{z},\theta) = \sum_{i=1}^{\infty} b_i(\theta)\,\phi_i(\mathbf{z}), \tag{2.13}$$

where ϕ_i are the corresponding eigenfunctions of the auto-covariance function $C(z_i,z_j)$ with its eigenvalues λ_i. Next, a truncated random field $\hat{H}(\mathbf{z},\theta)$ is formulated as

$$\hat{H}(\mathbf{z},\theta) = \sum_{i=1}^{M} \eta_i(\theta)\,\sqrt{\lambda_i}\,\phi_i(\mathbf{z}). \tag{2.14}$$

The KL expansion captures the variation by a finite number of eigenfunctions, whereby $\sqrt{\lambda_i}$ can be interpreted as its standard deviation. Note that $\eta_i = b_i(\theta)/\sqrt{\lambda_i}$ is a normalisation of the random variable b_i by the standard deviation. In addition, the KL expansion is truncated after M terms, as it can be approximated by the first modes. This follows the same idea as the truncated matrices of Eq. (3.5); in fact, Singular Value Decomposition (SVD) and KL expansion refer to the same concept.

The computation of the required eigenfunctions $\hat{\phi}_k(z)$ is not trivial and a numerical approximation is needed (Betz et al, 2014). Therefore, an analysis of the eigenvalues of the correlation matrix $\mathbf{C} \in \mathbb{R}^{N \times N}$ is used to compute its eigenvectors $\hat{\phi}$ and eigenvalues $\hat{\lambda}_k$. The dimension N refers to the number of unknowns associated with the numerical analysis. A random field with mean value $\mu_X = 0$ and standard deviation $\sigma_X = 1$ can be approximated as

$$\hat{H}(\mathbf{z}, \theta) = \sum_{i=1}^{M} \frac{\eta_i(\theta)}{\sqrt{\hat{\lambda}_i}} \sum_{j=1}^{N} \hat{\phi}_i(z_j)\, C(z, z_j). \tag{2.15}$$

One can conclude that with a defined covariance function (or correlation function) the random process can be described for joint Gaussian distributed variables. As a consecutive step, the field is discretised via KL expansion for an efficient application in numerical settings.

2.4. Robustness analysis

For uncertainty propagation, the identification of uncertain variables and the selection of a suitable representation by random variables or fields are the first steps. The theoretical background was given in the previous sections. This allows proceeding with the evaluation of the system and the impact of the statistical design parameters. We focus on forward problems, where we investigate the effect of a random input X on an output or a performance quantity $y = g(X)$.

In particular, our interest lies in the design of robust structures, leaving aside the concept of reliability. From a methodology point of view, robustness differs significantly from reliability analysis. Reliability refers to the circumvention of catastrophic failure in rare events and deals with small probabilities (Acar et al, 2021). On the contrary, a robust design should be insensitive to uncertain design parameters, i.e., have a low variability of the performance variable (Huang and Du, 2007; Chen et al, 1996).

2.4.1. Robustness classifications

Robustness is a collective term for varying research questions and associated methods. The first concepts of robust design methodologies were published by Genichi Taguchi in 1986 focusing on quality improvement. A recent review of robustness metrics for mechanical design identifies four different regions of robustness analysis (Göhler et al, 2016). The first class, called sensitivity, merely investigates the influence of one parameter on the output function, whereas the second class identifies a feasible design space. The third category uses functional expectancy and variance to describe robustness. The probability of fulfilling a robustness criterion with statistical variations of independent variables is the fourth class, which requires detailed knowledge about, e.g., variables' dependencies and functional limits. Here, we focus on the analysis of functional expectancy and variance. Hence, a robust optimisation intro-

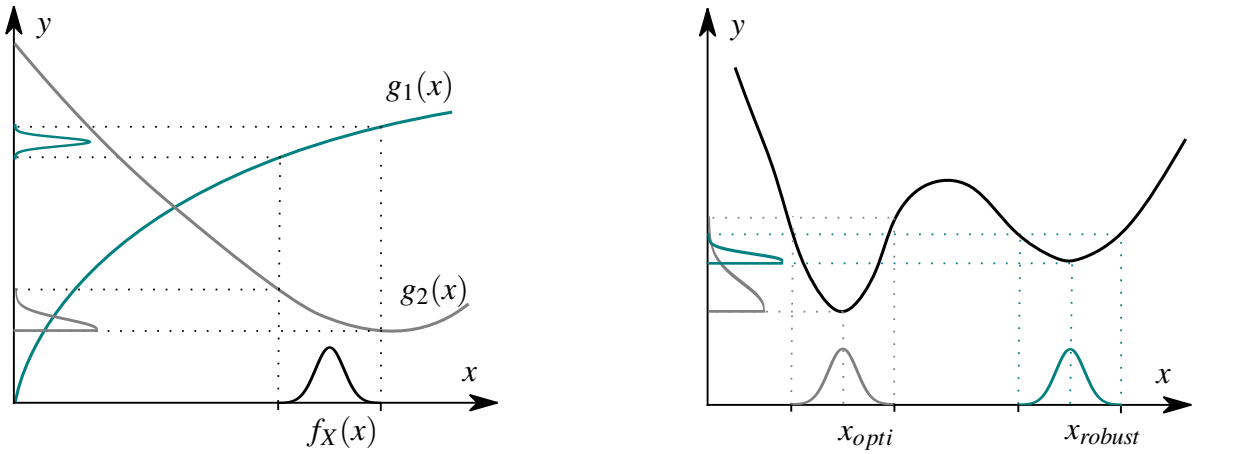

(a) Dependencies between random input quantity X defined by PDF with $f_X(x)$ and two exemplary systems $y = g(x)$ resulting in different distributions of the unknown y.

(b) Concept of a robust optimisation including random input variables X: absolute minimum x_{opti} and robust minimum x_{robust} by considering a low variability of y.

Figure 2.3 Conceptional ideas of robustness analysis based on expectancy and dispersion measure of a) the distribution of a performance quantity b) robust optimisation.

duced in Section 2.6, as well as the second-order statistic estimations with control variates from Section 2.5 belong to the third category.

2.4.2. Expectancy and dispersion measure

Ullah et al (2022) categorises classical robustness metrics as functions of the output performance parameter. With a "minimax criterion", also called set-based models (Kochenderfer and Wheeler, 2019), the distribution limits are identified as the worst-case scenario (Jurecka, 2007). On the contrary, the probability measures approximate the distribution of the output quantity. In this work, the so-called composite criterion is adopted, which is based on the approximation of expectation and dispersion. Figure 2.3 illustrates the composite criterion for two different scenarios: the distribution of a performance quantity in 2.3a and the concept of robust minima referring to 2.3b.

To explain the robustness metric, Fig. 2.3a shows the effect of a random input parameter on two examples with outputs $g_1(x)$ and $g_2(x)$. On the x-axis, the realisations x of a random variable X with PDF $f_X(x)$ are depicted. For forward problems, the distribution of the input parameter X is known, and the distribution of the output parameter y shall be investigated. In Fig. 2.3a the varying output distributions corresponding to $g_1(x)$ and $g_1(x)$ are visualised in grey and blue. These distributions are not known, and therefore a robustness metric is introduced to evaluate its important properties, such as mean and variance. We focus on problems with nonlinear dependencies between input x and output quantity y, which must be evaluated with numerical analysis and circumvent the application of analytical propagation methods. Therefore, we apply sampling strategies to solve the probability density integral, such as the highly popular Monte Carlo analysis and an extension with control variate, presented in the Section 2.5.

The right hand side of Fig. 2.3 illustrates the idea of a robust optimum. Within an optimisation process, one searches for the minimum of a performance parameter y under the variation of design parameters X, here a random variable. A robust optimum adds the variability of the performance measure to the original problem. Therefore, the dispersion-based robustness criterion is incorporated into the optimisation.

In Fig. 2.3b the conventional optimum is found at x_{opti}, which differs from the robust optimum x_{robust}. The robust optimum x_{robust} finds a compromise between absolute minima and a reduced standard deviation compared to x_{opti}. To estimate statistical properties, sampling techniques are required, which form a double-loop algorithm. The overall scheme for robust optimisation is presented as the second main analysis under uncertainties in Section 2.4.

2.5. Double-loop Monte Carlo analysis

As a first example of second-order statistics, the estimation of mean and variance through control variates are discussed. The theory is based on a classical Monte Carlo analysis, which is shortly reviewed. Afterwards, control variates are presented, incorporating a second analysis loop to improve its efficiency.

2.5.1. Monte Carlo analysis

Monte Carlo analysis is one of the most frequently used tools to analyse the moments and distributions of random variables and functions. It benefits from its general applicability to any numerical analysis through its non-intrusive nature and its simplicity. Hereby, the statistical moments are approximated by a sampling strategy. Samples of an input random vector X are created such that $x_i, i = 1,...,n$ and a numerical analysis is performed to obtain the corresponding quantity of interest $\mathbf{y}_i, i = 1,...,n$. This set of samples is then analysed using statistical methods. The mean $\mu_1 = E[Y]$ and variance $\mu_2 = E[(Y - E[Y])^2]$ of the response can be estimated with n number of samples, as

$$\hat{\mu}_1 = \frac{1}{n}\sum_i^n y_i, \tag{2.16}$$

and

$$\hat{\mu}_2 = \frac{1}{n-1}\sum_i^n (y_i - \hat{\mu}_1)^2. \tag{2.17}$$

Equations (2.16) and (2.17) are unbiased estimators, which implies that the mean of the estimator is equal to the actual quantity, when n approaches infinity. Furthermore, the variance of the estimators, can be interpreted as the mean squared error. Equations (2.18) and (2.19) formulate them as

$$V[\hat{\mu}_1] = \frac{\hat{\mu}_2(y)}{n}, \tag{2.18}$$

$$V[\hat{\mu}_2] = \frac{\hat{\mu}_4(y)}{n} - \frac{(n-3)\hat{\mu}_2^2(y)}{(n-1)n}, \tag{2.19}$$

with the approximated central moments $\hat{\mu}_4$ and $\hat{\mu}_2^2$ given in Appendix A.

The main disadvantage of MC analysis is the computational burden resulting from a large number of numerical analyses. To reduce computational effort, different improvements have been developed. One of the options is to adjust the sampling of the random input vector for a better dispersion in the output space. Prominent advanced sampling techniques are subset simulation, Markov Chain Monte Carlo, or directional sampling (Fishman, 1996). Another approach taken here is to introduce a multi-fidelity or multi-level scheme to reduce the costs associated with MC simulations.

2.5.2. Control variate estimators

The key idea of multi-level or multi-fidelity schemes is to introduce correlated low-fidelity models that assist in approximating the distribution at relatively low costs. The low-fidelity model is a simpler model that approximates the system with less computational effort, along with reduced accuracy. In engineering applications, the high-fidelity model corresponds to the original FE analysis, while a model discretised with a coarser mesh is often used as the low-fidelity model. The concept of control variate adapts the idea of a two-level analysis for second-order statistics based on MC simulations (Fishman, 1996). The double-loop algorithm stems from the introduction of the low-fidelity model. When extending the idea to multiple low-fidelity models, further research can be found under the key word of multi-fidelity MC or multi-level MC, referring to models with varying mesh resolutions (Zhang, 2021).

Control variate estimator for mean

In the following, we refer to the explanations of González et al (2019) to introduce control variate for engineering problems. Suppose that the response of interest y computed by the high-fidelity model is complemented by an additional low-fidelity approximation $\tilde{y}$. To evaluate the mean μ_1 the high-fidelity y and low-fidelity response $\tilde{y}$ are combined, such as:

$$\mu_1 = E[y] - \beta E[\tilde{y}] + \beta E[\tilde{y}], \tag{2.20}$$

with a so-called control parameter β. The addition and subtraction of the low-fidelity model in Eq. (2.20) is null from a theoretical point of view. Practically, the correlation between high- and low-fidelity model improves the estimation through different sampling sets. To explain the idea of different sample sets, we consider a vector Θ_n corresponding to n realisations of the random input vector and Θ_m to a vector of size m. The number of samples m is significantly higher than n, with $m \gg n$. For each sample set, the mean $\hat{\mu}_1$ can be approximated with a MC simulation following Eq. (2.16). Introducing the MC estimators in Eq. (2.20) the control variate

estimator $\hat{\mu}_1^{CV}$ can be formulated as

$$\hat{\mu}_1^{CV} = (\hat{\mu}_1(y,\Theta_n) - \beta\hat{\mu}_1(\tilde{y},\Theta_n)) + \beta\hat{\mu}_1(\tilde{y},\Theta_m). \tag{2.21}$$

Thus, a large number of low-fidelity assessments related to $\beta\hat{\mu}_1(\tilde{y},\Theta_m)$ can significantly improve the estimation of $\hat{\mu}_1(y,\Theta_n)$ with little additional cost. The error introduced by the low-fidelity model is corrected by the term $\hat{\mu}_1(y,\Theta_n) - \beta\hat{\mu}_1(\tilde{y},\Theta_n)$. Its variability is rather low, as the models are highly correlated. In such a way, the mean estimator $\hat{\mu}_1^{CV}$ can be evaluated with a better trade-off between accuracy and expenses. The variance of the estimator, interpreted as an error measure (Peherstorfer et al, 2018), can be calculated by

$$V\left[\hat{\mu}_1^{CV}\right] = A_1 - 2\beta A_2 + \beta^2 (A_3 + A_4), \tag{2.22}$$

where

$$\begin{aligned} &A_1 = V[\hat{\mu}_1(y,\Theta_n)] = \tfrac{\mu_{2,0}}{n}, \quad A_2 = Cov[\hat{\mu}_1(y,\Theta_n), \hat{\mu}_1(\tilde{y},\Theta_n)] = \tfrac{\mu_{1,1}}{n}, \\ &A_3 = V[\hat{\mu}_1(\tilde{y},\Theta_n)] = \tfrac{\mu_{0,2}}{n}, \qquad \text{and } A_4 = V[\hat{\mu}_1(\tilde{y},\Theta_m)] = \tfrac{\mu_{0,2}}{m} \end{aligned} \tag{2.23}$$

with the bivariate central co-moments between y and $\tilde{y}$

$$\mu_{p,q} = E[(y - E[y])^p (\tilde{y} - E[\tilde{y}])^q]. \tag{2.24}$$

The specific co-moments used for Eq. (2.23) can be found in Appendix A. Following Eq. (2.22) one can choose an ideal control parameter by minimising the variance of the estimator, such as

$$\beta^\star = \frac{A_2}{A_3 + A_4}. \tag{2.25}$$

Control variate estimator for variance

The same concept can be applied to the estimation of the variance μ_2 with a control parameter γ

$$\mu_2 = (V[y] - \gamma V[\tilde{y}]) + \gamma V[\tilde{y}]. \tag{2.26}$$

Comparable to the mean estimator of Eq. (2.21), the variance $\hat{\mu}_2^{CV}$ can be approximated by the control variate approach, with

$$\hat{\mu}_2^{CV} = (\hat{\mu}_2(y,\Theta_n) - \gamma\hat{\mu}_2(\tilde{y},\Theta_n)) + \gamma\hat{\mu}_2(\tilde{y},\Theta_m). \tag{2.27}$$

The variance of the estimator of the variance is given by

$$V\left[\hat{\mu}_2^{CV}\right] = B_1 - 2\gamma B_2 + \gamma^2 (B_3 + B_4) \tag{2.28}$$

with the terms B_1 - B_4 analogous to those defined in Eq. (2.23), for example $B_1 = V[\hat{\mu}_2(y, \Theta_n)]$. The detailed equations can be found in Appendix A. The control parameter is formulated accordingly:

$$\gamma^\star = \frac{B_2}{B_3 + B_4}. \tag{2.29}$$

Control parameters

The choice of the control parameter β is closely related to the discussion about unbiased estimators. A simple and practical choice could also be $\beta = 1$, which can result in accurate estimators $\hat{\mu}_1^{CV}$ for highly correlated low-fidelity models as presented in González et al (2019). Another option is to calculate the optimal control parameters β and γ from the sample set itself, as suggested with Eq. (2.25) and Eq. (2.29). To circumvent a biased estimator, a splitting scheme can be introduced (Avramidis and Wilson, 1993). Thus, the sample set is divided into groups from which β and $\hat{\mu}_1$ are calculated. For each group, the control variate estimator $\hat{\mu}_1^{CV}$ is computed combining the control parameters and the mean estimators from different groups. The final $\hat{\mu}_1^{CV}$ is the average of all groups. This concept can be consequently adapted for the variance estimator (Fina et al, 2022). For a detailed explanation, we here refer to Avramidis and Wilson (1993).

2.6. Double-loop robust design optimisation

The second selected double-loop scheme is a robust design optimisation under uncertainties. An optimisation algorithm searches for the minimum of a performance parameter under the variation of design parameters. The term robustness refers to a low variability of the performance quantity around the minima, as illustrated in Fig. 2.3b. In order to assess the variability, the evaluation of second-order statistics is required. This leads to a double-loop optimisation to i) find the minimum and ii) evaluate the variance-based robustness criterion.

2.6.1. Robust optimisation

We are interested in robust design optimisation, which utilises a variance-based robustness metric to find an insensitive optimum. For aleatoric uncertainties, it is either an input variable, also called a noise variable, or a design variable that represents the uncertainty. In the one-dimensional example of Fig. 2.3b the design parameter is modelled as a random variable. Notice that we here follow the naming convention for optimisation and indicate design variables with x, which does not continue the convention for random variables in the previous sections.

A general optimisation problem can be formulated by the objective function $f(\mathbf{x}_d)$ dependent on the vector of design variables $\mathbf{x}_d$:

$$\begin{aligned} \min \quad & f(\mathbf{x}_d) \quad s.t. \quad g(\mathbf{x}_d) \geq 0 \\ & {\mathbf{x}_d}^l \leq \mathbf{x}_d \leq {\mathbf{x}_d}^u. \end{aligned} \tag{2.30}$$

Furthermore, several constraints $g(\mathbf{x}_d)$ are formulated for the design variables x_d, which can be chosen between lower ${\mathbf{x}_d}^l$ and upper limits ${\mathbf{x}_d}^u$. The optimisation algorithm minimises the objective function under the defined constraints. A random design or noise variable W is additionally introduced such that $f(\mathbf{x}_d, W)$ with $w \in S$ for all realisations. Varying metrics can be formulated to describe the sensitivity of the objective function with respect to the uncertain parameter W. The most common technique is to create a two-loop optimisation algorithm. An inner loop computes a robustness metric, which can be considered as an objective or constraint within the standard optimisation procedure (Arsenyev, 2018). Here, we use the 'composite criterion', introducing the variance as a constraint g, which shall be below a threshold value σ^2_{thres}.

$$\min \quad f_r(\mathbf{x}_d) = E[f(\mathbf{x}_d, W)] \quad s.t. \quad V[f(\mathbf{x}_d, W)] \leq \sigma^2_{thres}. \tag{2.31}$$

Another idea is to add the robustness metric to the objective function $f_r(\mathbf{x}_d)$. This would represent an additional objective and lead to multi-objective optimisation. However, the multi-objective problem can be transferred into a single objective function by a weighted sum:

$$\min \quad f_r(\mathbf{x}_d) = E[f(\mathbf{x}_d, W)] + sV[f(\mathbf{x}_d, W)], \tag{2.32}$$

with s indicating the weight. Considering a black-box simulation, the statistical properties can not be calculated directly but must be approximated. Therefore, simulation-based methods are proposed to estimate statistical properties, such as MC analysis. To approximate the standard deviation, points around a candidate are evaluated with Eq. (2.16) and (2.17). This is repeated in every iteration of the optimisation to ensure the convergence to a robust optimum.

2.6.2. Evolutionary algorithms

Lastly, a strategy is needed to solve the optimisation problem, which suits the individual properties of the problem. In general, one can choose between gradient-based methods and gradient-free methods. The former uses gradient information to guide the algorithm towards the minimum. Gradient-based algorithms, such as gradient descent or quasi-Newton methods, are highly efficient in finding local optima for relatively smooth objective functions. The drawbacks of the descent methods are their poor performance for noisy or discontinuous objective functions. Then, gradient-free optimisation algorithms can be employed using population-based techniques, such as Evolutionary Algorithm (EA) or particle swarm optimisation. These global optimisation algorithms follow the principle of the survival of the fittest, whereby only the best candidates of a population are allowed to recreate. In an iterative process, a population of candidates shall evolve through selection, recombination, mutation and creation of offspring to a global minimum (Harzheim, 2014). Popular EA are Genetic Algorithms, Evolutionary Strategies and Differential Evolution (DE), although here we focus on the latter. The following briefly presents the DE algorithm, referring the interested reader to Kochenderfer and Wheeler (2019) for an overview of population-based algorithms.

Differential Evolution

First proposed by (Storn and Price, 1997), Algorithm 1 summarised the main steps of DE, which is also based on the explanations of Feoktistov (2006). For the sake of clarity, the subscript d of the design variable $\mathbf{x}_d$ is omitted in Algorithm 1. The three primary control parameters, the differentiation constant F, the crossover constant C_r, and the population size N_p need to be defined before the DE can be initialised. An initial population Pop^0 is generated employing a Design of Experiments (DOE) method within the bounds of the design variables. The while loop creates a reproductive scheme such that each generation is evaluated and manipulated, leading to a subsequent population. The main steps are recombination, crossover, and selection of the individuals within a population.

Algorithm 1 General DE algorithm (DE/rand/1) based on population size N_p, crossover constant C_r, differentiation constant F, maximum number of generations N_{gen}, objective function $f(x)$

Initialise population with DOE: $Pop \leftarrow \{\boldsymbol{x}_1, ..., \boldsymbol{x}_{N_p}\}$
Evaluate fitness: $f(Pop) \leftarrow \{f(\boldsymbol{x}_1), ..., f(\boldsymbol{x}_{N_p})\}$
while stopping condition not met **do**
  for all $\boldsymbol{x}_i \in Pop$ **do**
    Choose random individuals for differentiation
    $\pi = \{\boldsymbol{\xi}_1, ..., \boldsymbol{\xi}_n\} \subset Pop$ where $\boldsymbol{\xi}_i \neq \boldsymbol{\xi}_j$ for $i \neq j$
    Recombination: create trial vector by recombining the individuals in π
    $\boldsymbol{x}_t \leftarrow Recombination(\pi, F, Strategy)$
    Crossover: random mutation of single genes
    $\boldsymbol{x}_t \leftarrow Crossover(\boldsymbol{x}_t, C_r)$
    Check constraints for violation, if violated return to feasible domain
    Selection:
    if $f(\boldsymbol{x}_t) \leq f(\boldsymbol{x}_i)$ **then**
      $\boldsymbol{x}_i \leftarrow \boldsymbol{x}_t$
    else
      $\boldsymbol{x}_i \leftarrow \boldsymbol{x}_i$
    end if
  end for
  $Pop \leftarrow \{\boldsymbol{x}_1, ..., \boldsymbol{x}_{N_p}\}$
end while
return best individual $\boldsymbol{x}_{best}$

To test the current individual $\boldsymbol{x}_i$, the recombination function in Algorithm 1 creates a trial vector in the differentiation phase. Therefore, the trial vector is constructed by

$$\boldsymbol{x}_t = \boldsymbol{\beta} + F \cdot \boldsymbol{\delta}, \tag{2.33}$$

with a base vector $\boldsymbol{\beta}$, a difference vector $\boldsymbol{\delta}$ and the differentiation constant F. Different strategies to choose the base vectors and the difference vector exist, such as the DE/best/1. This strategy uses the best solution currently available as the base vector $\boldsymbol{\beta} = \boldsymbol{\xi}_1$ and adds the

difference of two random vectors $\boldsymbol{\xi}_2 - \boldsymbol{\xi}_3$ scaled by the differentiation constants F, such that $x_t = \boldsymbol{\xi}_1 + F(\boldsymbol{\xi}_2 - \boldsymbol{\xi}_3)$. A common starting point for the differentiation constant is $F = 0.5$, which may be increased to one in case of premature convergence (Storn and Price, 1997).

Next, the crossover function further manipulates the trial vector $\boldsymbol{x}_t$. Under a certain probability defined by $C_r \in [0,1]$ the new trial inherits parts of the previously constructed vector $\boldsymbol{x}_t$, otherwise the base vector $\boldsymbol{\beta}$ is unchanged. The design parameter setting of the trial vector $\boldsymbol{x}_t$ is applied if a randomly generated number $rand_j$ is smaller or equal C_r:

$$x_{t,j} = \begin{cases} x_{t,j} & \text{if} \quad rand_j \leq C_r, \\ \beta_j & \text{else.} \end{cases} \tag{2.34}$$

As a last step the fitness function is evaluated for the trial vector and compared to the current individual. If the fitness of the trial vector is smaller, it will replace the current candidate and thus be considered in the next generation. The while loop is terminated if a convergence criterion is met or a maximum number of iterations is reached.

Chapter 3

Projection-based model order reduction for structural analysis

In the last chapter, the theoretical background for analysis and optimisation has been introduced. The presented techniques result in highly cost-intensive multi-query analysis. To overcome the restriction associated with the high expenses, this contribution integrates model order reduction techniques into the workflow of robustness analysis and optimisation studies. To understand the proposed method, a second theoretical chapter introduces projection-based model order reduction (MOR) techniques for structural analysis. In recent years, research communities in the field of applied mathematics and computational mechanics have been developing varying projection-based MOR approaches. For the sake of clarity, the chapter merely presents the methods applied here. The theoretical chapter does not aim for a comprehensive literature overview, but is intended to provide a compact summary. Links to other popular research directions in the field of projection-based MOR are provided in the introduction.

3.1. Introduction to model order reduction for structural analysis

To establish reduced order models for structural analysis we start with the underlying concept of FE analysis in the following section.

Finite Element Method for structural analysis

The approaches presented here are based on the Finite Element Method (FEM), the key technology for analysis of structures. The continuous problem is discretised through a finite

number of elements to enable a numerical analysis of arbitrary structures. Attributing from the popularity of the technique, an enormous number of publications are dedicated to FE analysis. For the sake of compactness, a general introduction to FEM is omitted and the reader is referred to one of the extensive books on nonlinear FEM such as Belytschko et al (2014) or Wriggers (2008).

We start our explanations at the point of the semi-discretised equation of motion and emphasise the different nonlinearities typically considered for structural analysis. For dynamic structural problems the partial differential equation takes the following well-known form:

$$\mathbf{M}\ddot{\mathbf{u}} + \mathbf{f}(\mathbf{u}, \dot{\mathbf{u}}) = \mathbf{g}, \tag{3.1}$$

with $\mathbf{M} \in \mathbb{R}^{N \times N}$ being the mass matrix, $\mathbf{u}$, $\dot{\mathbf{u}}$ and $\ddot{\mathbf{u}}$ denoting displacement, velocity, and acceleration, $\mathbf{f}$ and $\mathbf{g}$ representing internal and external forces. The total number of degrees of freedom is N and depends on the resolution of the discretisation.

Equation (3.1) is discretised in space but continuous in the time domain. Therefore, a time integration scheme of implicit or explicit nature is required for dynamic systems. An implicit scheme fulfils Eq. (3.1) for each discrete time step and involves solving the system of equations. With an explicit integration scheme, the unknowns merely depend on the previous step, which, however, results in an integration scheme which is only conditionally stable and that requires the consideration of a critical time step.

If the internal force vector $\mathbf{f}$ of Eq. (3.1) includes a linear relationship between stress and strain and the assumption of small displacements, we speak of a linear problem. If these simplified assumptions are not sufficient to represent the problem at hand, the theory can be extended to nonlinear behaviour. The following nonlinearities are apparent for structural analysis: geometric nonlinearity, material nonlinearity, or nonlinearities due to boundary conditions such as contact. For geometric nonlinearities, the linearised kinematic assumptions are replaced by the consideration of large deformations and rotations. Therefore, a description of not only the initial configuration but also the deformed reference configuration is required. Iterative solvers such as Newton-Raphson schemes are needed to solve the equation of motion. Nonlinear material behaviour is introduced through a nonlinear stress-strain relationship such as hyper-elasticity, plasticity, or damage/fracture models. Another source of highly nonlinear analysis is the consideration of contact between two objects or self-contact (Wu and Gu, 2012). For a detailed discussion of the phenomena, the interested reader is referred to Belytschko et al (2014). In the scope of MOR we recommend the summary of (Rutzmoser, 2018) for a FEM scheme of hyper-elastic materials with large displacements.

The computational costs of FE analysis scale with degrees of freedom N. For industrial applications, detailed simulations require fine meshes with an increasing number of unknowns N.

Moreover, if additional nonlinearities are included, the computational costs will increase further through iterative procedures. Considering the analysis under uncertainties, as introduced in the previous chapter, a single FE analysis is repeated with varying parameter configurations, which greatly increases computational effort. Therefore, reduced order models have been introduced to scale down the cost of classical FE simulations.

Introduction to Model Order Reduction

Within the field of model order reduction, an extensive amount of research contributions can be found. Therefore, we briefly emphasise the selected techniques in comparison to other available approaches. Rather than a comprehensive overview, this shall give a general classification in comparison to other popular approaches. Many of the reduced order methods originate to the field of applied mathematics and are applicable to various system discretisation other than FE approaches. In comparison to well-established linear model order reduction techniques, data-driven and projection-based techniques for nonlinear problems are an active and fast evolving research field. Recent publications on reduced basis approaches for snapshot-based methods (Benner et al, 2021a) or time-dependent problems (Hesthaven et al, 2022) provide an extensive overview on the topics.

With projection-based approaches one assumes that the structure relies on an intrinsically lower dimension, which can represent the behaviour with a lower number of unknowns. The first challenge is to identify these lower dimensions with a new subspace. For the construction of the subspace, we will merely focus on data-driven approaches (Benner et al, 2021a), in contrast to simulation-free approaches (Rutzmoser, 2018).

A common linear projection method, the POD is a highly popular technique to derive the subspace from full-order training data. Hereby we assume that the solution manifold of an intrinsically nonlinear problem can be approximated with a linear projection method. POD is based on SVD, which is applied to a collection of full-order resultants, called snapshots, to construct a projection matrix. Hence, the transformation to the subspace and its corresponding back projection is a simple matrix multiplication. Other linear snapshot-based projection methods are Proper Generalised Decomposition or Dynamic Mode Decomposition.

Moreover, we are interested in parametric MOR techniques to construct efficient models within the scope of uncertainty and optimisation studies. Thus, a parameter space is introduced to the reduced model, which depicts the parameter variation required for multi-query analysis. From a practical point of view, the reduced order model shall represent not only one analysis, but the behaviour dependent on multiple parameter configurations. An extensive overview on MOR for parametric dynamical systems is given by Benner et al (2015) in the scope of linear MOR and its extension to nonlinear problems.

One can divide the MOR approaches into intrusive and non-intrusive techniques, whereby the former transfers the internal system operators. In contrast, the latter, non-intrusive approach regards the FE analysis as a black box and is a purely data-based method. In our case, the intrusive manipulation of the equation of motion is performed with a Galerkin projection. For nonlinear analysis, the projected equation still depends on the full-order dimension. Additionally, a hyper-reduction step is added to further reduce the system and enable an inexpensive online simulation (Ryckelynck, 2009). In this work, the Energy Conserving Sampling and Weighting (ECSW) technique and the closely related Empirical Cubature Method (ECM) (Hernández, 2020; Hernández et al, 2017) technique are presented in detail. However in literature, many different hyper-reduction techniques have been proposed, e.g., summarised in (Farhat et al, 2020).

The mentioned approaches based on POD are an efficient tool if the system behaviour is adequately presentable by the first few basis vectors. A well-known limitation of the linear projection method is its pure behaviour for problems with low Kolmogorov n-width. The Kolmogorov n-width describes the decaying rate of the eigenvalue, which is e.g. critical for transport phenomena in fluid dynamics. Several approaches have been developed to overcome these limitations. The idea of clustering the subspace by creating multiple smaller subspaces with a higher decaying eigenvalue rate has been proposed (e.g. Amsallem et al (2012)). Another line of research has developed adaptive schemes that allow retraining and weakens the separation of the online and offline phases, such as Rocha et al (2020). A more fundamental approach is to exchange the linear with a nonlinear projection method. These techniques are promising research directions, however, not an essential part of the proposed method.

Returning to non-intrusive approaches, data-driven techniques gain in popularity and specific Machine Learning (ML) methods are developed for engineering applications often dealing with sparse data regimes (Montáns et al, 2019). In Hesthaven et al (2022) the approach presented here is called Proper Orthogonal Decomposition with Interpolation, which decisively names the two main ingredients. Thus, the reduced basis vectors, computed by POD, are linearly combined and weighted depending on the parameter configurations. Hereby, the system operators are no longer involved, which creates a purely data-driven meta-model.

Often non-intrusive approaches also exploit nonlinear projection methods instead of linear ones, as the overall workflow is easier to realise. An example is the kernel Principal Component Analysis (PCA), which adds an additional higher-dimensional space, in which the PCA is performed. Another prominent area of non-intrusive MOR is based on artificial neural networks. Most recently, convolutional autoencoders have proven to successfully represent highly nonlinear manifolds (Lee and Carlberg, 2020; Fresca and Manzoni, 2022). Thus, the encoder detects a lower-dimensional representation which can be mapped back with the decoder network.

The approach presented here in detail combines data-based and physical knowledge to project the system of equations into a reduced subspace. During the training phase, the resultants of several full-order models, called snapshots, are exploited to derive the main deformation modes. A global POD is applied to the snapshot matrix, constructing a reduced space through a linear projection. The concept of linear projection through POD and SVD is explained in Section 3.2.1 and 3.2.2. Based on this projection matrix, an intrusive and non-intrusive approach is presented here. The intrusive scheme transfers the governing equation to the subspace to reduce the dimension. In addition to the Galerkin projection, the intrusive MOR scheme includes a hyper-reduction step approximating the nonlinear terms. Section 3.3 explains the approaches in detail. In contrast, the highlighted non-intrusive scheme combines the projection matrix with a regression analysis creating a purely data-driven surrogate model. The non-intrusive approach is outlined in Section 3.4 with the choice of three different regression models.

3.2. Snapshot-based projection via POD

The key idea of projection-based MOR is to find an intrinsically lower dimension that can sufficiently represent the system. The full-order FE analysis solves for a vector of unknowns $\mathbf{u} \in \mathbb{R}^N$ with N entries corresponding to each degree of freedom. To reduce the number of unknowns, $\mathbf{u}$, can be multiplied with a projection matrix $\mathbf{V} \in \mathbb{R}^{N \times k}$ of dimension k, with $k \ll N$

$$\mathbf{u} \approx \mathbf{V}\mathbf{u_r}. \tag{3.2}$$

The projection breaks down to a linear affine transformation with a reduced basis vector. Consequently, the construction of the reduced basis is essential for a successful projection-based scheme.

In a snapshot-based approach the computation of the reduced basis is based on full-order simulations, first proposed by Sirovich (1987). The output resultants, e.g. displacement vectors, of the training simulations, also called snapshots $\mathbf{u_i}$, are collected in a snapshot matrix $\mathbf{A}$. Thus, one searches for a subspace $\mathbf{V}$ of predefined dimension minimising the following problem

$$\min \sum_{i=1}^{n} ||\mathbf{u_i} - \mathbf{V}\mathbf{u_r}||_2. \tag{3.3}$$

with n the number of snapshots. POD solves this problem by applying SVD to the snapshot matrix. Under the terms PCA and KL expansion, similar concepts have been developed in varying research fields. The mathematical distinction between the techniques is analysed by Gerbrands (1981), whereby SVD seems to be the most general label for the underlying concept.

3.2.1. Singular Value Decomposition

Mathematically, the SVD is an orthogonal decomposition or transformation of a matrix. To introduce the technique, we follow the formulation of thin SVD for matrices $\mathbf{A} \in \mathbb{R}^{N \times n}$ with dimensions $N \geq n$ by Golub and Van Loan (2013). Applying SVD on the matrix $\mathbf{A}$ yields the left-singular vectors $\mathbf{U} \in \mathbb{R}^{N \times n}$, the diagonal matrix $\Sigma \in \mathbb{R}^{n \times n}$ containing non-negative singular values σ_i, and the right-singular matrix $\mathbf{Z} \in \mathbb{R}^{n \times n}$.

$$\mathbf{A} = \mathbf{U}\Sigma\mathbf{Z}^T. \tag{3.4}$$

The singular values in Σ_i appear in descending-order. It is assumed that the higher singular values are of greater "importance" and can sufficiently represent the dominant information. Therefore, the lowest singular values are neglected and the matrix is approximated by a truncation. Equation (3.5) shows the decomposed and truncated terms to approximate matrix $\mathbf{A}$ by a reduced matrix of rank k.

$$\begin{gathered} \mathbf{A} \approx \mathbf{U}_k \Sigma_k \mathbf{Z}_k^T = \mathbf{V}\Sigma_k \mathbf{Z}_k^T. \\ \mathbf{V} = \mathbf{U}_{:,:k} \in \mathbb{R}^{N \times k}, \quad \Sigma_k = \text{diag}(\sigma_1, ..., \sigma_k) \in \mathbb{R}^{k \times k}, \quad \mathbf{Z}_k = \mathbf{Z}_{:,:k} \in \mathbb{R}^{N \times k}. \end{gathered} \tag{3.5}$$

Thereby, the projection matrix $\mathbf{V} := \mathbf{U}_k$ can be identified, which resembles the mapping from the full to the reduced subspace.

To further illustrate the procedure, Fig. 3.1 shows the transformation of a three-dimensional sample set. The sample matrix $\mathbf{A} \in \mathbb{R}^{3 \times 34}$ is constructed by $n = 34$ snapshots in the Cartesian coordinate system (grey), which is plotted on the left side of Fig. 3.1. Note that in contrast to this example, in engineering applications, the dimension N is usually much larger than the number of snapshots n. Applying SVD the matrix can be reformulated through three orthogonal column vectors shown in black. On the right of Fig. 3.1 the data set is multiplied with the projection matrix $\mathbf{V}$ of a truncated rank $k = 2$, such that $\mathbf{V}^T\mathbf{A}$. The coordinate system in black is identical to the one on the left, whereby the right figure shows a two-dimensional projection of the data set. Hence, SVD approximates the data in a new 'coordinate' system of lower dimensions, which minimises the variance.

In contrast to the example of Fig. 3.1, it is not trivial to choose an ideal truncation rank k in the scope of projection-based approaches. As a lower bound for k is not known a priori, an optimal value $\tilde{k}$ under the constraint of an approximation error ε is obtained, such as:

$$\text{k} = \min \tilde{k} \quad \text{with} \quad \frac{\|\mathbf{A} - \mathbf{U}_{\tilde{k}} \Sigma_{\tilde{k}} \mathbf{Z}_{\tilde{k}}^T\|_F}{\|\mathbf{A}\|_F} \leq \varepsilon. \tag{3.6}$$

The Eckart-Young-Mirsky theorem (Eckart C, 1936; Mirsky, 1960) ensures optimality of the truncated SVD with respect to the Frobenius and spectral norms. In other words, no other

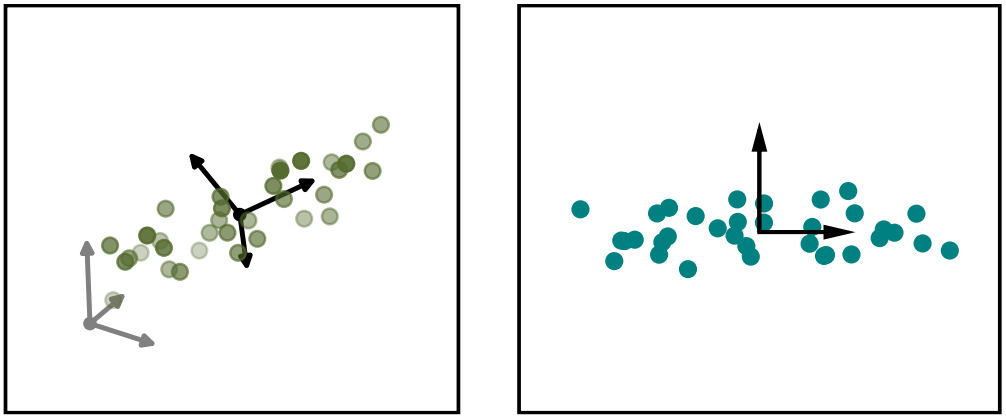

Figure 3.1 Exemplary transformation of a snapshot matrix $\mathbf{A} \in \mathbb{R}^{3\times 34}$ via SVD. On the left, data points are shown in the three-dimensional coordinate system (grey) and its left singular column matrix (black). The projected points are plotted in first two directions of the orthogonal column vectors (black), on the right. As here $n > N$ the decomposed terms have the following dimensions $\mathbf{U} \in \mathbb{R}^{N\times N}$, $\Sigma \in \mathbb{R}^{N\times N}$ and $\mathbf{Z} \in \mathbb{R}^{N\times n}$.

approximation of rank k with a smaller approximation error based on these norms exists. For the choice of an appropriate truncation, the singular values can give an import indication. Equation (3.6) can be reformulated as an energy ratio based on singular values σ, such as

$$\frac{\sum_{i=1}^{\tilde{k}} \sigma_i^2}{\sum_{i=1}^{n} \sigma_i^2} \leq 1 - \varepsilon^2. \tag{3.7}$$

The error measure ε shall ensure a certain level of accuracy with respect to the snapshot matrix approximation. Moreover, the decaying rate of the singular values can give further insight into the complexity of the system. A fast decaying rate indicates that an intrinsic lower dimension can be described by the first few basis vectors, whereas a low decaying rate requires more dimensions for a sufficient representation.

3.2.2. Data-based global POD

For parametric reduced order models the construction of the reduced basis and its underlying snapshot selection can be realised in various ways. Here, we discuss a global POD approach that combines time and parameter variations (Benner et al, 2015). Resultant vectors $\mathbf{u_i}(t,\mu)$ with $t \in T$ as time and $\mu \in P$ with the parameter domain P, are extracted from full-order training simulations. The total number of snapshots n consists of the snapshots at varying time instances $t_1, t_2, ..., t_{n_t} \in T$ and different parameter configurations $\mu_1, \mu_2, ..., \mu_{n_\mu} \in P$, such that $n = n_t n_\mu$. Here, the instance selection is based on a classical sampling strategy, such as Latin hyper-cube sampling or Sobol sampling. The collected snapshot matrix is reformulated through SVD, and the projection matrix can be constructed.

For large-scale matrices, a conventional evaluation of SVD can be highly computationally ex-

pensive or infeasible as its complexity exhibits $O(n^2)$. To address such problems, randomised or incremental SVD techniques (Bach et al, 2019; Oxberry et al, 2017) may be applied. Other developments, such as proposed in Phalippou et al (2020) who introduced an iterative enrichment of the snapshot matrix in combination with an incremental SVD are conceivable.

In general, the choice of snapshots is crucial to the construction of a suitable reduced basis. The classical sampling strategy could also be exchanged for adaptive sampling via greedy search algorithms (Benner et al, 2015). Snapshots are iteratively sampled following the highest approximation error of the reduced model, such as presented by Bui-Thanh et al (2008) using trust region optimisation. Another approach divides the space into multiple local subspaces, also called localised model order reduction. Therefore, different subspaces for parameter clusters are constructed in the offline phase. For each online analysis, the best-fitting cluster is selected, on which the system operators are projected (see Amsallem et al (2012) in combination with ECSW hyper-reduction or (Peherstorfer et al, 2014) with DEIM). For a comprehensive overview on the adaptation of local bases, we refer to (Hesthaven et al, 2022; Benner et al, 2015).

3.3. Intrusive model order reduction

The foundation of the reduced order model has been developed in the previous section by constructing a reduced basis formulation from snapshots. Next, we discuss how intrusive MOR schemes exploit the projection matrix to reduce the dimensions of the system operators. Figure 3.2 gives a schematic overview of intrusive MOR, which is implemented within

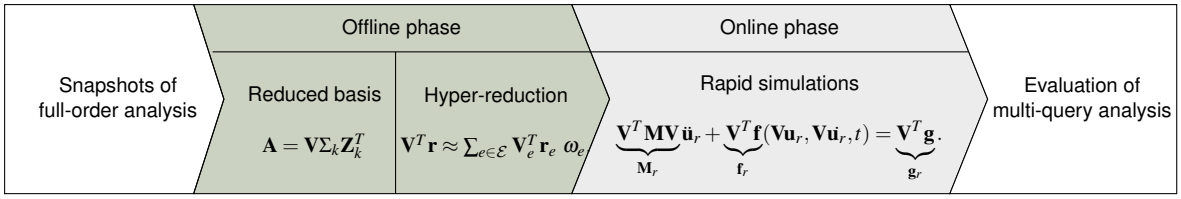

Figure 3.2 The workflow for intrusive MOR divided into online and offline phase.

the FE solver. It is divided into an offline, or preparation phase and an online step. Within the preparation step, a suitable orthogonal projection matrix is constructed, as explained in Section 3.2. This allows a Galerkin or Petrov-Galerkin projection of the equation of motion into a subspace to reduce the number of unknowns. However, for a nonlinear problem the computation of the internal force vector still depends on the full-order analysis. Therefore, an additional hyper-reduction step is introduced, which also requires a precomputation in the offline phase. Consequently, the Galerkin projected system with hyper-reduction can be evaluated in the online phase with lower computational expenses.

In literature, many different hyper-reduction techniques have been proposed. A first approach, called gappy POD has been introduced to computational mechanics by Willcox (2006). Farhat et al (2020) classifies the approach as an approximate-then-project method, whereby other related techniques are Discrete Empirical Interpolation Method (DEIM) (Chaturantabut and Sorensen, 2010), its further development UDEIM by Tiso and Rixen (2013), or Gauss-Newton with Approximated Tensors (GNAT) proposed by Carlberg et al (2013). Another group of hyper-reduction methods follows the idea of project-then-approximate, such as the ECSW technique by Farhat et al (2014, 2015) or ECM published in Hernández et al (2017). For more recent publications, deep neural networks (Cicci et al, 2022), dynamic mode decomposition (Kutz et al, 2016) or operator inference (Peherstorfer and Willcox, 2016) can be named as alternative options for hyper-reduction.

For structural FE analysis, ECSW and its closely connected ECM provide beneficial numerical stability properties and are therefore presented here. Thereby, a subset of elements is selected to approximate the nonlinear internal forces. In the following section, the Galerkin projection is introduced, whereby its differences to the Petrov-Galerkin projection are drawn. Section 3.3.2 introduces ECSW and ECM, as a hyper-reduction technique.

3.3.1. Galerkin projection

To derive the Galerkin projection we repeat the equation of motion of dimensions N with the mass matrix $\mathbf{M} \in \mathbb{R}^{N \times N}$, displacement vector $\mathbf{u}$, external forces $\mathbf{g}$ and the nonlinear internal force vector $\mathbf{f}$:

$$\mathbf{M}\ddot{\mathbf{u}} + \mathbf{f}(\mathbf{u}, \dot{\mathbf{u}}, t) = \mathbf{g}. \tag{3.8}$$

Let us assume that a suitable reduced basis, which represents the system with lower dimensions $k \ll N$, is available. The projection matrix $\mathbf{V}$ can be introduced to Eq. (3.8)

$$\mathbf{M}\mathbf{V}\ddot{\mathbf{u}}_r + \mathbf{f}(\mathbf{V}\mathbf{u}_r, \mathbf{V}\dot{\mathbf{u}}_r, t) = \mathbf{g} + \mathbf{r}. \tag{3.9}$$

Through the approximation implied by the projection, an additional residual $\mathbf{r}$ appears. As for N equations k unknowns are not determined uniquely, the residual is also multiplied by the matrix $\mathbf{V}$, such as

$$\mathbf{V}^T\mathbf{r} = 0. \tag{3.10}$$

If the matrix $\mathbf{V}$ in the above equation is the projection matrix, one speaks of a Galerkin projection. For a Petrov-Galerkin approach, $\mathbf{V}$ would be exchanged by another orthogonal matrix $\mathbf{W}$ to bound the residual. The over-determined system is constrained to be orthogonal to the space spanned by the residual. Thus, we introduce the approximation of Eq. (3.10) to the equation of motion for general nonlinear dynamics:

$$\underbrace{\mathbf{V}^T\mathbf{M}\mathbf{V}}_{\mathbf{M}_r}\ddot{\mathbf{u}}_r + \underbrace{\mathbf{V}^T\mathbf{f}}_{\mathbf{f}_r}(\mathbf{V}\mathbf{u}_r, \mathbf{V}\dot{\mathbf{u}}_r, t) = \underbrace{\mathbf{V}^T\mathbf{g}}_{\mathbf{g}_r}. \tag{3.11}$$

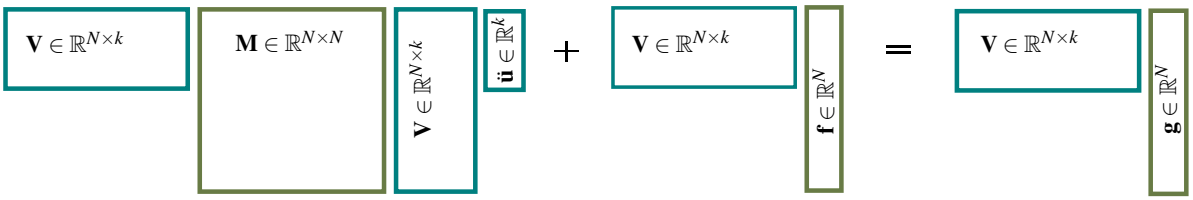

Figure 3.3 The matrix dimensions of projected system of equations following Eq. (3.11) to underline the transformation from dimension k to N with $k \ll N$.

The matrix dimensions of Eq. (3.11) are visualised in Fig. 3.3 to underline the transformation from dimension k to N with $k \ll N$. For dynamic analysis the reduced equation of motion can be solver with an implicit or explicit time integration scheme (Farhat et al, 2014), whereby (Bach et al, 2018) highlights the effects on explicit procedures.

3.3.2. Hyper-reduction

The Galerkin projection reduces the size of equations solved in implicit time integration schemes and therewith the computational costs. For linear problems, this can already result in significant speedups. However, Eq. (3.11) is still coupled to the original system size N when evaluating the internal force vector. It defines the reduced internal force vector with

$$\mathbf{f}_r := \mathbf{V}^T \mathbf{f}(\mathbf{V}\mathbf{u}_r, \mathbf{V}\dot{\mathbf{u}}_r, t). \tag{3.12}$$

As the reduced force vector $\mathbf{f}_r$ is computed by multiplying $\mathbf{V}^T$ by the force vector $\mathbf{f}(\mathbf{V}\mathbf{u}_r, \mathbf{V}\dot{\mathbf{u}}_r, t)$ of dimension N Eq. (3.11) still depends on the physical dimensions. The evaluation of nonlinear forces is performed at every element for every time step in the physical space and requires large computational resources. Reference is made to Farhat et al (2020) for a detailed overview of the computational bottleneck, which distinguishes between linear and nonlinear problems. To avoid the high cost associated with the nonlinear force vector, commonly an additional reduction step called hyper-reduction is introduced (Ryckelynck, 2009). Applying hyper-reduction, the nonlinear terms are only evaluated at selected entries or elements, to circumvent the dependency on the full-order dimension. In the following the ECSW technique and the closely related ECM method are introduced, to circumvent the bottleneck for nonlinear analysis.

Energy Conserving Sampling and Weighting

By applying the ECSW technique (Farhat et al, 2014, 2015) the internal forces are evaluated over a reduced number of elements, while conserving the global energy of the system. Moreover, ECSW yields symmetric system matrices and exhibits superior numerical stability properties compared to other hyper-reduction methods. To identify potential candidates for the hyper-reduction, a non-negative weighting factor is computed for each element to quantify its impact on the solution vector. In general, the global internal force vector $\mathbf{f}$ is assembled

through the connectivity matrix $\mathbf{L}_e$ with the force vectors $\mathbf{f}_e$ for all elements $e \in \Omega$. Through the hyper-reduction the full-order space Ω is approximated by a sub-set $\mathcal{E}$ and a weighting vector ζ^* of weights ζ_e^* for each element:

$$\mathbf{V}^T\mathbf{f} = \mathbf{V}^T \sum_{e\in\Omega} \mathbf{L}_e^T\mathbf{f}_e \approx \mathbf{V}^T \sum_{e\in\mathcal{E}} \zeta_e^*\mathbf{L}_e^T\mathbf{f}_e. \tag{3.13}$$

The product of $\mathbf{V}^T\mathbf{f}$ can be interpreted as the virtual work, which constitutes virtual displacement multiplied by a force vector. Consequently the energy can be conserved by choosing appropriate weighting factors (Farhat et al, 2014). To compute the weights ζ_e^*, the unassembled training forces are collected in the matrix $\mathbf{G} \in \mathbb{R}^{n\times N_e}$

$$\mathbf{G} = \begin{bmatrix} G_{1,1} & \cdots & G_{1,N_e} \\ \vdots & \ddots & \\ G_{n,1} & & G_{n,N_e} \end{bmatrix}, \quad \mathbf{G}_{i,e} = (\mathbf{V}^T)_e\mathbf{f}_e^{(i)} \tag{3.14}$$

with $\mathbf{f}_e^{(i)}$ being defined as the i-th snapshot of the unassembled internal force vector of element e, N_e the number of elements, and n the number of snapshots. Next, the vector $\mathbf{b} \in \mathbb{R}^n$, the sum over all elements $\mathbf{b}_i = \sum_{e\in\Omega} G_{i,e}$ is set up. The linear equations $\mathbf{b} = \mathbf{G}\zeta$ are formulated, whereby all entries of ζ are ones. A minimisation problem is solved with a predetermined tolerance τ, such as:

$$\text{argmin}\,\|\zeta\|_0 \quad \text{s.t.} \quad \|\mathbf{G}\zeta^* - \mathbf{b}\|_2 < \tau\|\mathbf{b}\|_2 \quad \text{and} \quad \zeta^* \geq \mathbf{0}. \tag{3.15}$$

Here, $\|\cdot\|_0$ is the 0-pseudo norm, which counts the number of non-zero entries of its argument. Equation (3.15) is approximated by a sparse non-negative least square method. A solution can be obtained using greedy algorithms, where elements are added until the condition of Eq. (3.15) is satisfied.

Empirical Cubature Method

The Empirical Cubature Method (ECM) algorithm has been introduced by Hernández et al (2017); Hernández (2020), which are the basis for the following explanations. ECM is closely related to ECSW, however, it operates on the integration point level to identify suitable elements. For each selected element, a corresponding non-negative weighting factor is computed to characterise its impact in the assembling process of the reduced system. Instead of considering the unassembled force vector, the residual is used for the computation of the weighting factors. From Eq. (3.8) follows that the residual vector is defined as

$$\mathbf{r}(\mathbf{g},\ddot{\mathbf{u}},\dot{\mathbf{u}},\mathbf{u},t) = \mathbf{g} - \mathbf{M}\ddot{\mathbf{u}} - \mathbf{f}(\mathbf{u},\dot{\mathbf{u}},t). \tag{3.16}$$

Recall that through the Galerkin projection the residual is spanned orthogonal to the projection matrix following Eq. (3.10), such that $\mathbf{V}^T\mathbf{r}(\mathbf{g}, \mathbf{V}\ddot{\mathbf{u}}_r, \mathbf{V}\dot{\mathbf{u}}_r, \mathbf{V}\mathbf{u}_r, t) = \mathbf{0}$.

The assembly of the reduced system is performed element by element. Therefore, the elemental contributions are collected from all elements $e \in \Omega$ as:

$$\mathbf{V}^T\mathbf{r} = \sum_{e\in\Omega} \mathbf{V}_e^T\mathbf{r}_e \approx \sum_{e\in\mathcal{E}} \mathbf{V}_e^T\mathbf{r}_e \; \omega_e. \tag{3.17}$$

Similarly to ECSW, the set of finite elements Ω is reduced to a subset $\mathcal{E}$ and a weighting vector ω, with $\omega_e > 0$, through hyper-reduction. To obtain the subset of elements and corresponding weights, the unassembled projected residuals are gathered in the matrix $\mathbf{S} \in \mathbb{R}^{(kn)\times N_e}$, such that

$$\mathbf{S} = \begin{bmatrix} \mathcal{S}_{1,1} & \cdots & \mathcal{S}_{1,N_e} \\ \vdots & \ddots & \\ \mathcal{S}_{n,1} & & \mathcal{S}_{n,N_e} \end{bmatrix}, \quad \mathcal{S}_{i,e} = \mathbf{V}_e^T\mathbf{r}_e^{(i)}. \tag{3.18}$$

The number of elements and snapshots is denoted by N_e and n and the vector $\mathbf{r}_e^{(i)}$ is defined as the i-th snapshot of the unassembled residual for element e. Moreover, we define the exact assembly, the sum of all elements $\mathbf{b} = \mathbf{S}\zeta$, with $\zeta := \{1\}^{N_e}$. The optimisation problem can be formulated identically to Eq. (3.15) as already explained for ECSW. It is well known that the problem of Eq. (3.15) is NP-hard (Boyd and Vandenberghe, 2004), and therefore it is necessary to resort to convexification or sub-optimal greedy procedures. The ECM applies a greedy procedure to find the required hyper-reduced data. Unlike ECSW, an SVD is performed on the matrix of projected residuals $\mathbf{S} \approx \mathbf{U}_r\sigma_r\mathbf{G}$. It was observed by Hernández et al (2017) that the truncation tolerance for this SVD is closely related to the tolerance τ in the original problem of Eq. (3.15). The required hyper-reduction data are obtained by passing the truncated matrix of the right singular vectors $\mathbf{G}$ to the algorithm: [$\mathcal{E}$,ω] = ECM($\mathbf{G}$).

Therewith, the basics of intrusive model order reduction have been introduced. In summary, the system operators are projection into a subspace via Galerkin projection and an additional hyper-reduction step, which circumvents the bottleneck of computing nonlinear internal forces.

3.4. Non-intrusive model order reduction

The non-intrusive MOR is purely based on data analysis exploiting techniques from the field of machine learning. In contrast to the previously mentioned intrusive scheme, the characteristic equation of the underlying physical phenomena is not invoked. Therefore, non-intrusive MOR belongs to the class of surrogate models. In this context, proper orthogonal decomposition with interpolation (Hesthaven et al, 2022) is introduced, which combines the reduced basis with a

regression model. Examples of successful applications in the scope of nonlinear structural analysis are given by Guo and Hesthaven (2017); Swischuk et al (2019); Yu et al (2019); Kast et al (2020); Kaps et al (2022). In comparison to conventional surrogates, which are commonly used for multi-query analysis, the non-intrusive MOR method operates in the subspace and does not predict the full-order system directly. Moreover, the corresponding model is bounded to physical solutions supplied by the reduced basis.

Non-intrusive schemes do not entail a time integration scheme; therefore, the time parameter must be handled in a different manner. Analogous to the concept of global POD, see Section 3.2.2, the time domain is treated in a similar manner as the parameter domain. Thus, the time instance is an additional input parameter to the regression model. Another possibility is to use a two-level POD (Xiao et al, 2015) to separate spatial and temporal modes. Furthermore, the tensor decomposition of Guo and Hesthaven (2019) provides an advanced way to cope with two classes of parameters of different nature. These approaches show interesting concepts which are, however, not elaborated on further.

In essence, the non-intrusive model approximates the system response as a weighted linear combination of the basis vectors $\mathbf{v}$

$$\mathbf{u} \approx \sum_{i=1}^{k} \mathbf{v_i} \alpha_i(t, \mu). \tag{3.19}$$

Recalling Section 3.2.1, every column $\mathbf{v_i}$ in the projection matrix $\mathbf{V} \in \mathbb{R}^{N \times k}$ represents a reduced basis vector:

$$\mathbf{V} = \begin{bmatrix} \mathbf{v_1} & \mathbf{v_2} & \cdots & \mathbf{v_k} \end{bmatrix}. \tag{3.20}$$

Hereby, the scalar values α_i define the influence of each basis. The weights $\alpha_i(t, \mu)$, depending on the parameter configuration μ and time instance t, are computed with the help of a regressor. One can also interpret the approach as a regression model in the reduced subspace, whereby $\alpha_\mathbf{i} = \mathbf{u}_r$. To gain the full-order resultant vector, a projection back to the physical space $\mathbf{u} = \mathbf{V}\mathbf{u}_r$ is required. Consequently, the evaluation of the governing equation is replaced by a much simpler regression model, however also situated in the reduced space.

Figure 3.4 summarises the overall workflow of the presented non-intrusive MOR approach. Consistent with the intrusive scheme, one distinguishes between an offline (training) and an online phase. First, a snapshot matrix $\mathbf{A} \in \mathbb{R}^{N \times n_t n_\mu}$ is built from the resultants of full-order analysis. To align with the intrusive scheme, we collect displacement data, which could also be replaced by any other quantity of interest. As discussed in Section 3.2.1, POD is performed on the snapshot matrix $\mathbf{A}$ and a truncated set of basis vectors is selected. A list of time $t_i \in T$ and parameter configurations $\mu_i \in P$ corresponding to the snapshots is additionally prepared. Prior to passing $\mathbf{u}$ to the regression model, a multiplication with the transposed matrix $\mathbf{V}$ projects

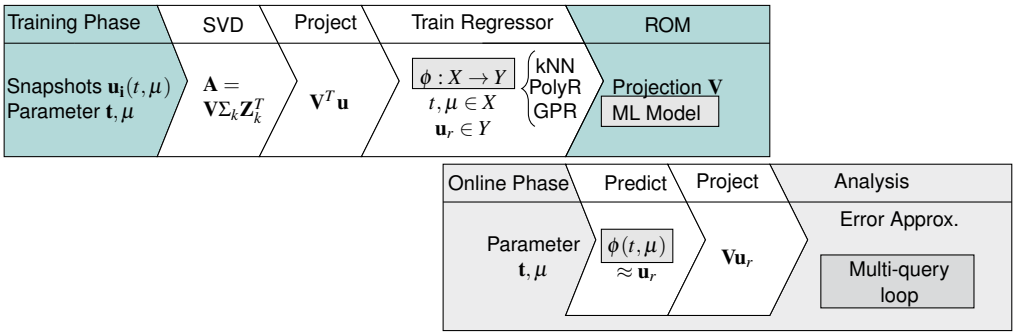

Figure 3.4 The workflow for non-intrusive MOR divided into online and offline phase.

the data into the subspace. Then, a regression model $\phi : X \to Y$ maps the input $t, \mu \in X$ to the outputs $\mathbf{u}_r(t,\mu) \in Y$, whereby $\mathbf{u}_r(t,\mu)$ denotes the vector of unknowns in the reduced space. We focus on k-Nearest Neighbour (kNN), Polynomial Regression (PolyR), Gaussian Process Regression (GPR) as interchangeable regression models. After completing the training phase, Fig. 3.4 depicts the online phase by the lower grey bar. For a specific parameter μ and a time instance t the regression model provides a system answer $u_r(t,\mu)$. To interpret the predicted output, the vector must be projected back into the physical space.

To comprehensively describe the concept of Fig. 3.4, the regression models kNN, PolyR and GPR are presented. Other regressors, such as radial basis functions or artificial neural networks, could also be used in the presented setting. From a machine learning perspective, regression models are supervised learning techniques. To approximate an unknown regression function f we assume that a training set $\mathbf{x}, \mathbf{y} \in D$ is available, where for each pair $x_i, y_i : y_i = f(x_i)$. The available data set is commonly divided into test and training data. The test data contains n observation of data points with $\mathbf{x} = [x_i, ..., x_n]$ and its corresponding outputs $\mathbf{f} = [f(x_i), ..., f(x_n)]$. In general, the regression model is found by minimising a cost function ε that penalises deviations of a prediction $\hat{\boldsymbol{f}}_i$ from its true value $\boldsymbol{f}_i$. Moreover, the model depends on certain model parameters $\boldsymbol{\Theta}$, corresponding to the chosen regression technique. The minimisation problem can be formulated as,

$$\boldsymbol{\Theta}^* = \arg\min_{\boldsymbol{\Theta}} \varepsilon(\mathbf{f}(\mathbf{x}), \hat{\mathbf{f}}(\boldsymbol{\Theta}, \mathbf{x})). \tag{3.21}$$

During machine learning, the model parameters Θ, also called hyperparameters, of the chosen method are optimised. The training set is utilised to build the regression model, which can then be tested with the remaining test data $\mathbf{x}_\star$ and its corresponding $\mathbf{f}_\star$ to assess its accuracy.

3.4.1. K-nearest neighbour regression

The kNN algorithm is commonly applied for classification problems and is less known as a regression model. In a classification problem, kNN divides the set of n observations into multiple clusters. Whenever a new point is classified, the (Euclidean) distance to its k nearest

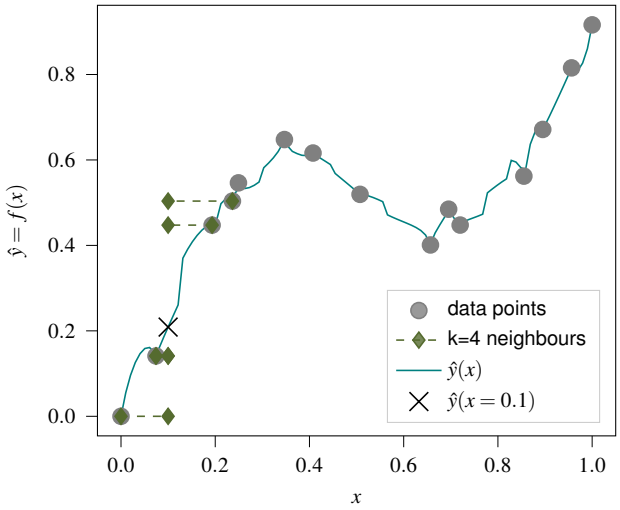

(a) kNN regression with 4 nearest neighbours using the weighted distance to the prediction point $\hat{y} = f(0.1)$.

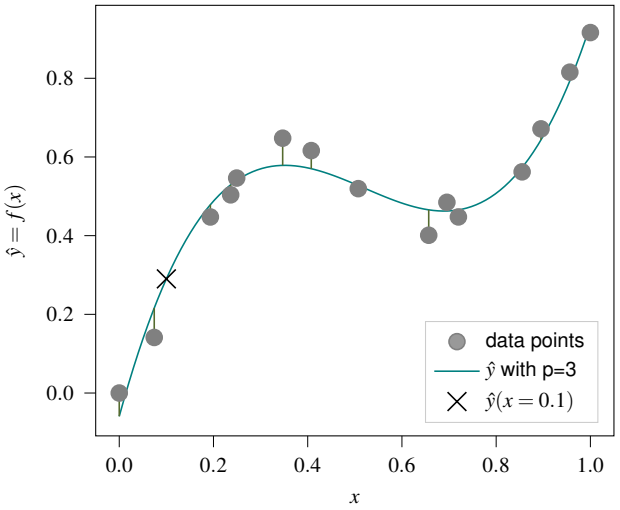

(b) PolyR regression function with $p = 3$ computed by minimising the residuals to the data points.

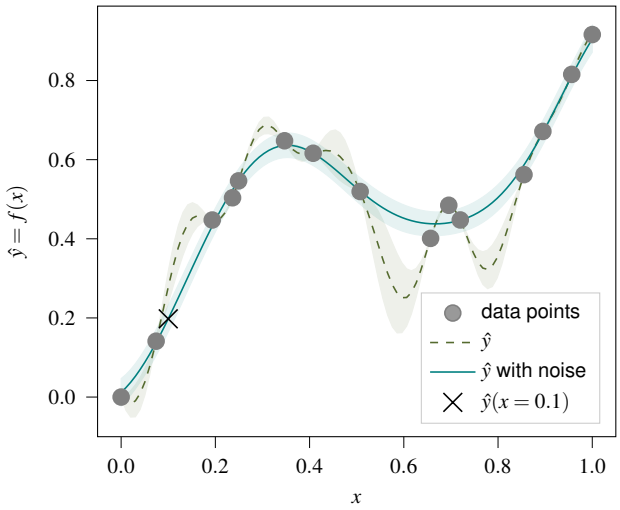

(c) GPR regression with and without considering noisy data and its confidence intervals.

Figure 3.5 Comparison of the regression curve $\hat{y}$ based on kNN, PolyR, GPR for a data set of $n = 15$ observations.

neighbours is computed to select the cluster. Consequently, regression through kNN also involves the closest k neighbours for prediction. The approximation technique averages the value of k neighbours, optionally considering their distances by a weighting factor. The hyper-parameter is, hereby, k, the number of neighbours. The key question is how to efficiently find neighbours within the data set. A naive attempt solves this problem by computing all distances to select the nearest neighbours. The algorithm is characterised by the cost of $O[dn^2]$ with the number of sample points n in dimensions d. To find the closest data points in a more efficient way, tree structures are used, such as the k-d tree by Bentley (1975).

To illustrate the regression algorithms, Fig. 3.5 shows a data set with $n = 15$ observations and dimension $d = 1$. An exemplary test data point $f(x_\star = 0.1)$ is approximated with kNN. Using

$k = 4$ neighbours, its value is calculated by the weighted distance as depicted by the dotted lines in Fig. 3.5a. Moreover, the solid line represents the regressor evaluated at equidistant points along the domain. The prediction is solely based on interpolation, which results in a non-smooth curve. In general, the advantage of kNN is its simplicity and robustness. As shown in the following sections, other techniques can create more sophisticated regression models.

3.4.2. Polynomial regression

In contrast to the local approximation of kNN algorithms, polynomial regression functions belong to global approximation techniques. A polynomial function $\hat{f}(x)$ of degree p shall approximate the unknown function $f(x)$ with a minimal residual error ε, such that

$$f(x) = \hat{f}(x) + \varepsilon. \tag{3.22}$$

An approximation using first-order polynomials is obtained by the first two terms of the following equation:

$$\hat{f}(x) = \beta_0 + \sum_{i=1}^{p} \beta_i x_i + \sum_{i=1}^{p} \sum_{j>i}^{p} \beta_{ij} x_i x_j, \tag{3.23}$$

which is extended to a more general form for higher polynomials with the third term. The approximation includes regression coefficients β_i, which are chosen such that the residual r, the sum of squares between the function $y = f(x)$ and its approximation $\hat{f}(x)$ is minimised:

$$r(\beta) = \sum_{w=1}^{n} (y_w - \beta_0 - \sum_{i=1}^{p} \beta_i x_{iw} - \sum_{i=1}^{p} \sum_{j>i}^{p} \beta_{ij} x_{iw} x_{jw})^2. \tag{3.24}$$

Equation (3.24) can be solved with an ordinary least-squares solver. Although this method includes polynomials of x, it is essentially a linear technique, as the vector β is in linear relation to $\mathbf{y}$. For this reason, the method is often referred to as multiple linear regression or linear polynomial regression. The interested reader is referred to Bishop (2006) for a detailed overview of linear regression models and its developments.

Figure 3.5b shows an exemplary polynomial function $\hat{f}(x)$ with $p = 3$ that approximates the identical data set of the previous example. Here, the distance to the approximation function, the residuals, are drawn in green for each training point. The approximation function $\hat{f}(x)$ is chosen such that the sum of all residuals is minimised. In general, PolyR benefits from a clear function formulation and rapid evaluations, but can suffer from overfitting for high polynomial degrees (Bishop, 2006).

3.4.3. Gaussian process regression

Compared to kNN and PolyR, GPR is a probabilistic regression approach, which is based on Gaussian random processes introduced in Section 2.2.2. In contrast to the previously presented random fields, we are not interested in deriving sample functions from a Gaussian process, but we use its beneficial properties for a predictive model. Thus, training points are treated as random variables with joint Gaussian distributions, and predictions are accompanied by confidence intervals. We focus only on GPR, which is closely related to the popular Kriging approaches that add a trend function to the process. The presented derivations are mainly based on Rasmussen and Williams (2006).

A set of training points $\mathbf{x}$ and its function evaluations $\mathbf{f}$ are assumed as a stationary Gaussian process with a zero mean and a covariance matrix $K(\mathbf{x},\mathbf{x})$. An underlying covariance function, as presented in Section 2.3.2, defines the relation between the data points and is therefore the core of the process. Based on the data set of observed points $\mathbf{f}$ the joint distribution to new test outputs $\mathbf{f}_\star$ can be constructed

$$\begin{bmatrix} \mathbf{f} \\ \mathbf{f}_\star \end{bmatrix} \sim N\left(0, \begin{bmatrix} K(\mathbf{x},\mathbf{x})K(\mathbf{x},\mathbf{x}_\star) \\ K(\mathbf{x}_\star,\mathbf{x})K(\mathbf{x}_\star,\mathbf{x}_\star) \end{bmatrix}\right), \tag{3.25}$$

with the covariance matrix $K \in \mathbb{R}^{n\times n_\star}$ and the number of test points $n_\star$. The joint distribution can be transformed to a conditional distribution, from which the function values $\mathbf{f}_\star$ are sampled. The value of the new prediction response is then the mean $\bar{\mathbf{f}}_\star$

$$\bar{\mathbf{f}}_\star = K(\mathbf{x}_\star,\mathbf{x})K(\mathbf{x},\mathbf{x})^{-1}\mathbf{f}, \tag{3.26}$$

$$\mathrm{Cov}(\mathbf{f}_\star) = K(\mathbf{x}_\star,\mathbf{x}_\star) - K(\mathbf{x}_\star,\mathbf{x})K(\mathbf{x},\mathbf{x})^{-1}K(\mathbf{x},\mathbf{x}_\star). \tag{3.27}$$

For a single test point the covariance $\mathrm{Cov}(\mathbf{f}_\star)$ equals to the variance. If the observations are based on noisy data, the approximation $y = f(x) + \varepsilon$ includes a noise variable ε. The additive noise ε is assumed to be independent and identically normal distributed with variance σ_n. Therefore, the term $K(\mathbf{x},\mathbf{x})$ in Eq. (3.25) is extended by the noise distribution resulting in $K(\mathbf{x},\mathbf{x}) + \sigma_n\mathbf{I}$, with the identity matrix $\mathbf{I}$. The predictions for testing data based on noisy observations are as follows,

$$\bar{\mathbf{f}}_\star = K(\mathbf{x}_\star,\mathbf{x})[K(\mathbf{x},\mathbf{x}) + \sigma_n^2\mathbf{I}]^{-1}\mathbf{f}, \tag{3.28}$$

$$\mathrm{Cov}(\mathbf{f}_\star) = K(\mathbf{x}_\star,\mathbf{x}_\star) - K(\mathbf{x}_\star,\mathbf{x})[K(\mathbf{x},\mathbf{x}) + \sigma_n^2\mathbf{I}]^{-1}K(\mathbf{x},\mathbf{x}_\star). \tag{3.29}$$

The correlation matrices K are calculated based on a predefined correlation function. Hereby,

the correlation lengths are non-physical hyper-parameters. Typically, an optimisation is performed to find an ideal choice for the corresponding data set.

A regression analysis based on GPR for the exemplary data set is plotted in Fig. 3.5c. With a noise-free assumption, GPR interpolates between the training points. The dotted green line represents the mean following Eq. (3.26) and its standard deviation is marked by the shaded area around it. This can be interpreted as the approximation's confidence interval. A GPR with noisy data is used to plot the solid blue line calculated with the assumptions of Eq. (3.28). This approximation does not necessarily conform to the training points. The statistical properties and its flexibility due to the choice of kernel function are beneficial properties of GPR. However, since a matrix inversion of the covariance matrix is computationally very demanding, a large set of data points can be problematic.

Part III

Methods

Chapter 4

Multi-fidelity scheme based on two-level model order reduction

This chapter presents a novel multi-fidelity scheme exploiting reduced order models as the core part of the thesis. It is based on the theoretical framework introduced in the last two chapters. Hereby, the proposed methods intertwine the basic concepts of model order reduction with analysis and optimisation under uncertainties.

For uncertainty quantification or optimisation studies, the iterative nature of the analysis leads to high computational costs. To enable such analyses for highly complex industrial simulations, reduced order models have been developed. The MOR approach introduced here combines classical physics-based FE analysis with data-driven methods to enable cost-effective simulations. In this chapter, the idea is further extended, and a novel multi-fidelity approach is proposed as the main development of this thesis. The intrusive reduced order model, as presented in Section 3.3 is complemented by a non-intrusive model that improves the iterative procedures. To ensure a high correlation between the models, an adaptive update of the non-intrusive model is additionally suggested. The multi-fidelity scheme represents a general applicable technique that specifically focuses on cost-intensive double-loop algorithms. We are particularly interested in robust design and propose a robustness analysis and robust optimisation incorporating the multi-fidelity scheme based on two levels of model order reduction.

The properties of the proposed multi-fidelity scheme are presented, and the options for vari-

ous applications are highlighted in the following paragraph. The workflow is explained in detail, distinguishing between the preparation phase in Section 4.1.1 and the online phase in Section 4.1.2. The subsequent sections focus on the implementation of the multi-fidelity framework for analysis and optimisation under uncertainties. To better understand the workflow, pseudo algorithms explain the application to the double-loop schemes. The chapter is closed with Section 4.4 on the transformation to single-fidelity schemes and related collaborative publications.

4.1. Multi-fidelity scheme for double-loop algorithms

To lower the computational costs, several reduced order models have been developed, which bridge the gap between data-driven surrogates and physical analysis, ideally combining the benefits of both. The proposed multi-fidelity scheme considers intrusive MOR for analysis and optimisation under uncertainty. When creating the intrusive model, the construction of an additional non-intrusive model is a natural extension. Therefore, this non-intrusive meta-model is based on the already available reduced basis. An additional regression model, corresponding to the reduced number of unknowns in the intrusive model, is easy to incorporate and with little additional cost. On the other hand, this correlated low-fidelity model can add useful knowledge in the process of multi-query analysis.

The approach presented here shall be a general scheme for applications of varying iterative analysis. We focus on analysis under uncertainty because these iterative methods are inherently cost-intensive and severely constrained by their computational complexity. For example, in MC analysis, the accuracy of the estimator corresponds directly to the number of system evaluations, and thus to the computational effort. Two costly analysis schemes, a double-loop optimisation and a double-loop MC analysis, are presented to show the variety of use cases. However, the proposed scheme is not limited to these application cases.

The general workflow for the analyses under uncertainties is outlined in Fig. 4.1. To start the analysis, the present uncertainties must be quantified. To describe the aleatoric uncertainties, probabilistic techniques, as introduced in Section 2.2 are employed. We distinguish between single random variables or spatially varying random processes. Uncorrelated random variables could be a material property, e.g., Young's modulus, a geometrical dimension, such as the thickness of a plate (see Chapter 5) or an uncertain loading as introduced in Chapter 7. On the other hand, a random process can describe correlated uncertainty fields in the space or time domain. Examples of spatially correlated uncertainties in structural analysis are inhomogeneous material properties or complex boundary conditions.

If the distribution of the random parameter is already known, one can directly incorporate this expert knowledge into the numerical analysis. As in Chapter 7 or 8 random variables are

defined via normal distributions with certain mean and variance. However, in practical settings, such information is often not available. An example of the quantification of statistical properties is given in Chapter 6. The spatial uncertainties of beech wood are modelled with the theory of random fields. Accessing the theoretical background of Section 2.3 on random fields, a correlation function must be quantified to describe the apparent properties of the correlated field. Based on an experimental data set, an approach is presented to describe the data with a correlation function. With the discretised random field, material properties can be adjusted at the element level, serving as input to the FE analysis. The derived statistical quantities are then used to define the samples in the training phase and are the basis for any type of multi-query analysis.

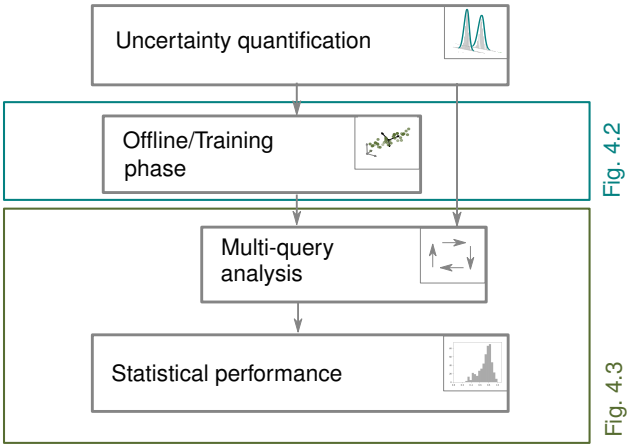

Figure 4.1 Overview of workflow divided in online and offline phase for proposed multi-fidelity scheme

In the offline or training phase, the reduced order model is constructed, explained in further detail in the next section. Iterative analyses are performed in the online phase, described in Section 4.1.2. Detailed explanations of the individual steps are summarised in Fig. 4.2 and Fig. 4.3. As a final stage, results of the multi-query analysis can be evaluated to quantify the statistical performance.

4.1.1. Training phase for parametric problems

Figure 4.2 shows a comprehensive overview of the preparation phase for the multi-fidelity MOR scheme. The grey boxes indicate the considered options between different methods, and the icons give a visual connection to the theoretical background presented in the previous chapters.

After identifying and describing the statistical parameters, the training phase can be initialised. For the set of training simulations, the sampling should correspond to the random variable or field that describes the uncertainty. Moreover, training simulations should cover the possible range of realisations of the random variable or field to define a suitable design space. This can be achieved by applying appropriate sampling procedures, also called design of experiments. A full factorial sampling is suitable for one- or two-dimensional design spaces, whereby it is

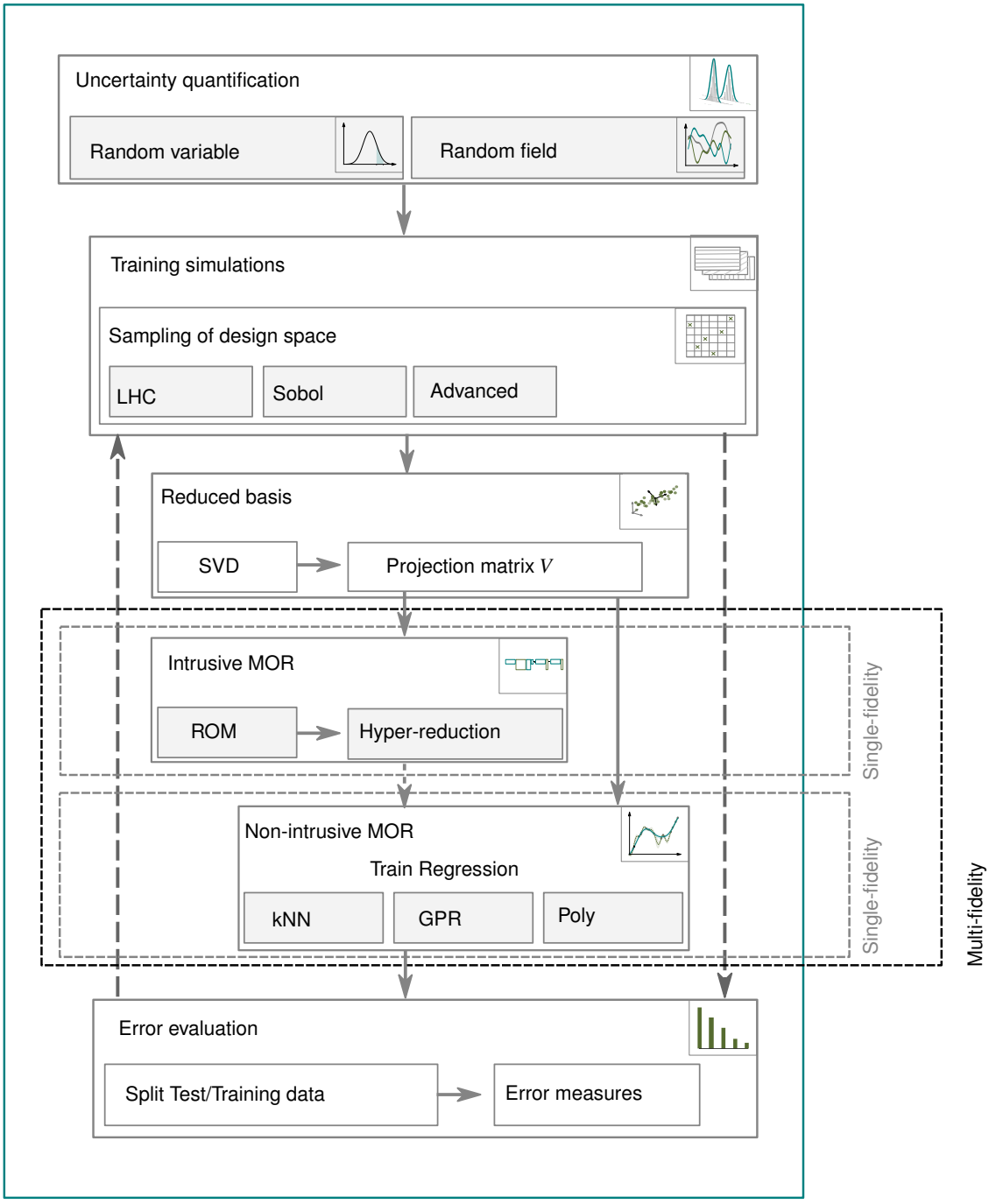

Figure 4.2 Training phase of multi-fidelity scheme constructing an intrusive and a non-intrusive model for uncertainty propagation with varying options highlighted in grey.

beneficial to include the corner points. For such cases, Sobol sampling is a useful sampling strategy, as the training set can be successively enhanced according to the Sobol numbers, as applied in Chapters 5 and 8. Another popular sampling technique is Latin Hypercube Sampling (LHS), which spans a grid of sample points throughout the design domain. Other advanced sampling approaches are especially helpful when dealing with large design spaces or sparse samplings. For example, Kaps et al (2022) apply an adjusted sampling technique for large dimensions (see also Komeilizadeh et al (2023)) to create non-intrusive reduced order models in the scope of multi-fidelity crash optimisations.

With the sampling strategy, full-order analyses are performed, which often presents the main cost of the training stage. Snapshots from all training simulations are collected and a global POD (see Section 3.2) is performed. Therewith, a suitable projection matrix is identified on which intrusive and non-intrusive models are constructed. The intrusive method is based on a Galerkin projection and a hyper-reduction as introduced in Section 3.3. First, a Reduced order model with Galerkin projection (ROM) is established by the Galerkin projection of the system of equations. Based on ROM simulations, the residuals or forces are collected for the computation of the hyper-reduced elements. After performing the ECM or ECSW algorithm, the Hyper-reduced Order Model with Galerkin projection (HROM) is available.

For the multi-fidelity scheme, a second low-fidelity model is added. The non-intrusive model is created on the basis of the projection matrix. Thus, the weighted combination of the reduced basis vectors represents the low-fidelity model. To predict the corresponding weights, a regression model is introduced, using approaches such as kNN, PolyR, or GPR presented in Section 3.4. When employing a single-fidelity scheme, one can choose between an intrusive and a non-intrusive model and neglect the training step corresponding to the other approach.

The error of the reduced order model must be evaluated as a last step. In the ML community, the available data set is commonly divided into test and training samples. The training set is used to create the reduced model, while the test set is applied to evaluate accuracy measures. The quality of the reduced model can be analysed with bisectoral plots or error measures, such as the generalised mean root square error e_{GMRE}. Furthermore, the division of test and training sets is expandable by cross-validation procedures, as discussed in Chapter 8.2. The dotted line indicates that a reconstruction of the reduced order model might be required if accuracy levels are not sufficient. For example, one can increase the number of training simulations or the truncation rank of the projection matrix. At the end of the training phase, an intrusive and a non-intrusive model representing the parametric problem are available.

4.1.2. Online phase for analysis and optimisation under uncertainties

In the previous section, the construction of high- and low-fidelity reduced order models has been explained step by step. With the models in place, we can move to the online phase and efficiently perform multi-query analyses. An overview of the proposed multi-fidelity scheme is

given in Fig. 4.3. The presence of multiple options within the analysis scheme is highlighted with grey boxes. In addition, the steps related to robust optimisations are coloured blue, while robust analysis is highlighted in light green. To illustrate the modularity of the scheme, the grey frames show possible conversions to single-fidelity workflows. The workflow associated with multi-fidelity analysis is framed by the black dotted line in Fig. 4.3.

The top of Fig. 4.3 illustrates the collection of uncertain parameters as a starting point. As mentioned in the previous section, random phenomena can be described by a random variable or, in more complex cases, a spatially distributed random field. On the basis of the uncertain parameter and the desired type of analysis, the iterative procedure is initiated. Both multi-fidelity analyses start an iterative loop, where analyses are repeated with varying parameter configuration. In an outer loop, the high-fidelity is analysed, followed by an optional updating of the low-fidelity model. The idea is that through the additional high-fidelity simulations, new response outputs are available. The training set is enriched with these snapshots, and the regression model can be retrained. Note that the reduced basis is constant through the iterative process, and only the regressor is updated. Next, a second inner loop is executed using the low-fidelity model for analysis.

Figure 4.3 depicts Full-Order Model (FOM) and intrusive ROM, or HROM as possible high-fidelity models to perform the outer loop analysis. For the inner loop, one has here the choice between three different regression models incorporated in the non-intrusive scheme. Furthermore, the approximation accuracy of the non-intrusive model can optionally be improved throughout the retraining step. To gain the highest computational speedup, HROMs should be chosen as the high-fidelity model. For the applications presented here, FOMs are commonly utilised to create a reference solution. However, it is also a reasonable choice in combination with non-intrusive models (Kaps et al, 2022). Another possibility is to omit the hyper-reduction step and directly use ROMs to perform the outer loop, as in the study of Chapter 8.1.

The first option is an optimisation under uncertainties using a variance-based robustness criterion (see Section 2.6), highlighted in blue on the left of Fig. 4.3. The robustness criterion can be considered via the objective function or as a constraint of the optimisation problem. The double-loop algorithm combining two different MOR techniques is employed for optimisation studies with population-based techniques. Evolutionary algorithms introduce a population of sample points which is iteratively adapted such that it converges to a global minimum. For each sample point in every iteration, a structural analysis is required. A second loop evaluates the robustness measure based on the variance. Example studies are introduced in Chapter 8.

The green boxes in Fig. 4.3 indicate the robustness study based on MC analysis and control variate, such as introduced in Section 2.5. In the case of an analysis under uncertainties, a fixed number of samples is analysed during a MC simulation. Similarly, FOM, ROM, or HROM can be applied to realise the MC analysis. When working with control variates, a second

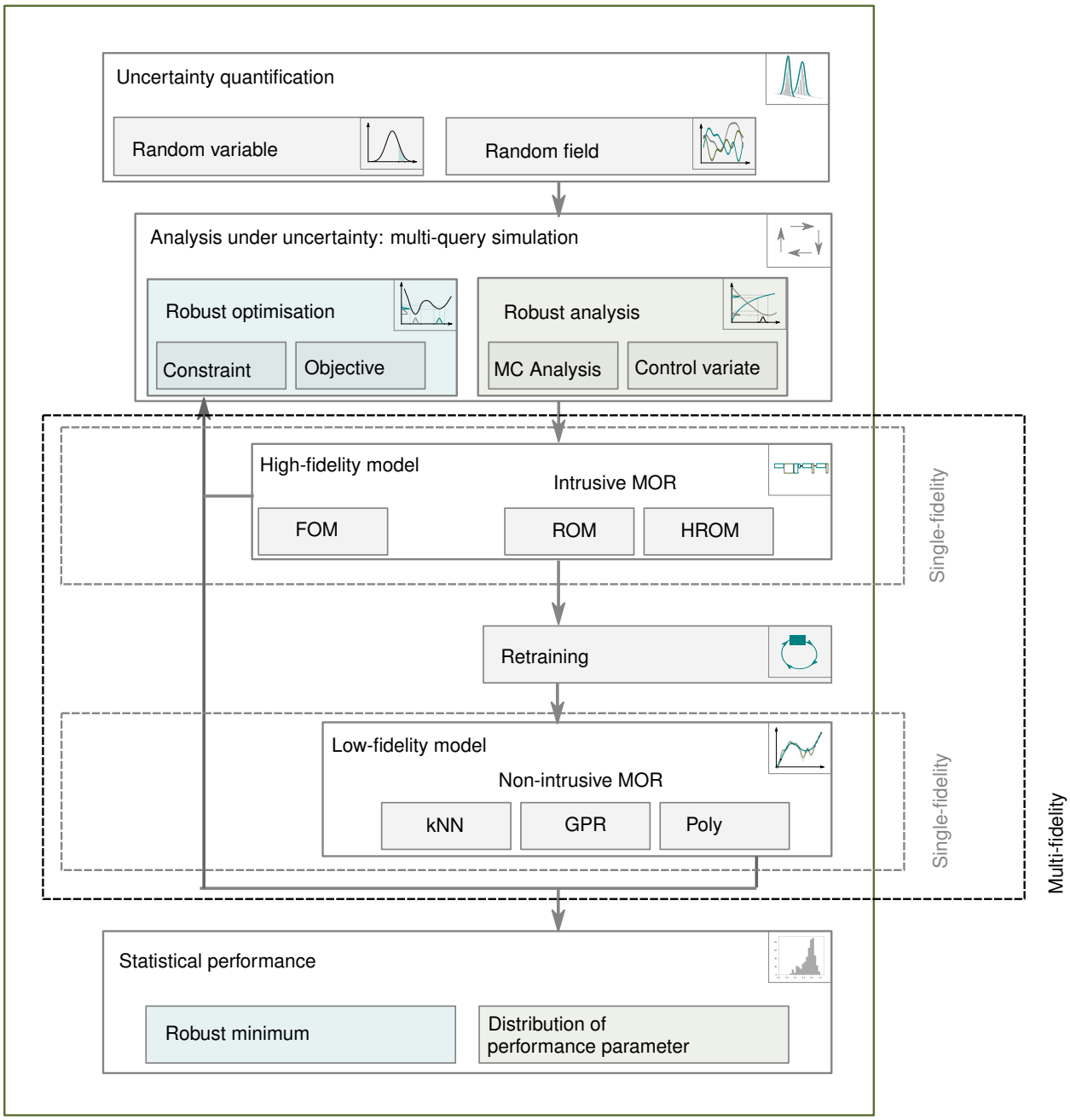

Figure 4.3 Online phase of multi-fidelity scheme employing multiple levels of intrusive and non-intrusive models for robust analysis and optimisation.

inner loop is introduced. Evaluations of the correlated low-fidelity model improve the mean and variance estimators with reduced computational costs. For the construction of the low-fidelity model, additional information from the outer loop can be incorporated. This optional retraining increases the correlation between the high- and low-fidelity models. The multi-fidelity scheme is applied in Chapter 7, where a beam experiencing large displacements through varying loading conditions is analysed.

Figure 4.3 depicts the evaluation of statistical performance as the final stage. For an optimisation study, the robust minima can be visualised along with the convergence of the design variables and objective function. The distribution of the performance parameter is the main outcome of the robustness analysis.

We can summarise that the proposed multi-fidelity scheme exploiting varying levels of MOR is tailored to analysis and optimisation under uncertainties. The construction of the model follows Fig. 4.2, where its theoretical background is presented in Chapter 3. Methods belonging to the field of uncertainty quantification have been introduced in Chapter 2 in a systematic manner. The extension through reduced order models is a major novelty of this work. Figure 4.3 shows a summary of the multi-fidelity approach using different levels of model order reduction. The following two sections provide a detailed implementation of robust optimisation and MC analysis with control variate based on multiple MOR levels. Moreover, its transformation to single-fidelity schemes and related collaborative publications are mentioned in Section 4.4.

4.2. Multi-fidelity robustness analysis via control variate estimators with reduced order models

Figure 4.3 presents robustness analyses that estimate the distribution of a performance parameter as one of the multi-fidelity applications. The theoretical background for statistical analysis through MC simulations and control variate estimators was introduced in Section 2.5. This is the basis for Algorithm 2 that shows the proposed multi-fidelity workflow intertwining the control variate approach with model order reduction techniques.

The definition and initialisation of the random variables is the first step. In particular, two vectors Θ_n and Θ_m of size n and m, with $n \ll m$, are populated by realisations of the random variables. In addition, low- and high-fidelity models g_{LF} and g_{HF} are required to initialise the analysis.

Algorithm 2 further specifies the control variate sampling procedure specific to the multi-level approach. The outer loop represents the analysis with the high-fidelity model g_{HF}. Based on the input vector Θ_n, the performance resultants of n intrusive MOR simulations are collected.

Algorithm 2 Uncertainty propagation of random input parameters with control variate estimator based on low-fidelity model g_{LF} and high-fidelity model g_{HF}

Define random variable;
Initialise Θ_n, Θ_m with n, m samples and $n \ll m$; ▷ realisations of random variable
function CONTROL VARIATE PROCEDURE($\Theta_n, \Theta_m, g_{HF}, g_{LF}$)
  for n sample points Θ_n **do** ▷ **outer loop**
    $y_i = g_{HF}(\theta_i)$ ▷ intrusive MOR
  end for
  Retraining of g_{LF} ▷ update non-intrusive model
  for $(n+m)$ sample points in $(\Theta_n + \Theta_m)$ **do** ▷ **inner loop**
    $\tilde{y}_j = g_{LF}(\theta_j)$ ▷ non-intrusive MOR
  end for
  Compute control parameter β, γ ▷ apply splitting scheme
  Mean estimation $\hat{\mu}_1^{CV}(\mathbf{y}, \tilde{\mathbf{y}}, \beta)$ and $V\left[\hat{\mu}_1^{CV}\right]$
  Variance estimation $\hat{\mu}_2^{CV}(\mathbf{y}, \tilde{\mathbf{y}}, \gamma)$ and $V\left[\hat{\mu}_2^{CV}\right]$
end function

These samples can additionally be utilised to improve the low-fidelity model g_{LF}, by a reconstruction with the supplementary snapshots from the high-fidelity analysis. If the regression model is based on interpolation, e.g. kNN, the updated low-fidelity model gives the identical system answer as the high-fidelity model at the retraining points. To avoid this fact, it is recommended to apply PolyR or GPR with noise as a regression model within the non-intrusive scheme.

In the next step, the inner loop is called evaluating m simulations with $m \gg n$ using the non-intrusive model. Note that the loops are not nested compared to the optimisation algorithm and can also be executed in a parallel manner. Subsequently, the mean and variance estimators are evaluated as in Eq. (2.21) and (2.27), respectively. Moreover, the corresponding estimators and their control parameters β and γ are computed within a splitting scheme. To judge the approximation, the variance of the estimators corresponding to the mean square error can additionally be computed following Eq. (2.22) and (2.28).

The accuracy of the estimators increases proportionally with the number of sample evaluations. Therefore, the cost associated with the corresponding numerical analysis is of great importance. In the proposed scheme, the processing time for numerical analyses is reduced by employing MOR techniques. Assuming a constant budget, the number of samples can be increased through the multi-fidelity technique, which consequently improves the accuracy of the estimators. The double-loop algorithm consists of an outer loop using intrusive methods and an inner loop applying non-intrusive methods. Hence, the correlated models are ideally arranged in a bi-fidelity scheme to enable large efficiency gains.

The method is showcased in Chapter 7 for a structural design problem, a three-dimensional beam-like structure. Thereby, the loading direction is uncertain and is modelled as two un-

correlated normal random variables. With the proposed scheme, we evaluate the distribution of the tip displacement, as the performance quantity. In comparison to simulations with the full-order model, we can show that the proposed scheme significantly reduces computational cost. Moreover, we present the application of the intrusive hyper-reduced order model and the retrained non-intrusive surrogate.

4.3. Multi-fidelity robust optimisation with reduced order models

Building upon the general workflow of MOR based multi-fidelity schemes, the next paragraph concentrates on its specific application to robust optimisations. Therefore, Algorithm 3 explains the multi-fidelity scheme for the double loop algorithm. The analyses through low- and high-fidelity models are indicated by g_{LF} and g_{HF}, whereby the detailed options for high- and low-fidelity models can be found in the overview of Fig. 4.3. Additional comments are added to Algorithm 3 to clarify whether intrusive or non-intrusive techniques are relevant. Algorithm 3 is embedded in an optimisation strategy, here a population-based method, which is not further detailed. Within the optimisation procedure, the sample points of a population are evaluated and recombined through iterations to reach a global optimum. After the initialisation of the optimisation parameters and random variables, the optimisation loop is entered. In this outer loop, the objective function $f(x)$ is repeatedly executed for different design parameters x during the optimisation procedure.

Within the outer loop, a second inner loop is introduced to calculate the robustness metric. We are interested in the variability p_i of the target y_i with respect to the random phenomena. Therefore, sample points x^s are calculated around the current design parameter x_i considering the random variable. With the help of the high-fidelity model g_{HF}, the variance of the performance quantity y_i is computed applying the MC estimator of Eq. (2.17). Through the additional simulations gained by the variance evaluation, the low fidelity g_{LF} can be enriched. In a consecutive step, the performance of the design variable x_i can be analysed with the improved low-fidelity model.

Robust optimisation procedures can consider the robustness criterion within the objective function as Eq. (2.32) or as a constraint following Eq. (2.31). Algorithm 3 incorporates the variance-based criterion into the objective function by $f_i = \tilde{y}_i + s \cdot p_i$ with the weight s. Finally, the fitness f_i of the candidate is returned to the general optimisation procedure. This procedure is applied to all candidates in the population and repeated in each iteration until the convergence criterion of the optimisation study is met.

Caused by the double-loop algorithm, the costs associated to the optimisation algorithm are scaled with the number of evaluations multiplied by the number of samples for the variance

Algorithm 3 Workflow for population based optimisation algorithms exploiting low-fidelity model g_{LF} and high-fidelity model g_{HF}

```
Define random variables
Initialise optimisation
while search for minimum do                                   ▷ outer loop
    function OBJECTIVE FUNCTION(x_i, g_HF, g_LF)
        Define n sample points x^s around x_i                 ▷ based on location and dispersion
        for n sample points x^s do                            ▷ inner loop
            y_j = g_HF(x^s_j)                                 ▷ run intrusive ROM to approx. variance
        end for
        Variance criterion p_i(y)
        Retraining of g_LF                                    ▷ update non-intrusive ROM model
        Evaluate sample point ỹ_i = g_LF(x_i)                 ▷ run non-intrusive ROM
        f_i = ỹ_i + s · p_i                                   ▷ objective + variance criterion
        return f_i
    end function
end while
```

estimation. The intrusive and non-intrusive models help to accelerate the overall workflow and enable such cost-intensive analysis.

Depending on the focus of the study, the application of intrusive and non-intrusive techniques is interchangeable. In Algorithm 3 the high-fidelity model is used to approximate the variance of the design point and the low-fidelity for the design point itself. This could also be exchanged when the computation of the robustness criterion is of less importance. To still realise the retraining of the low-fidelity model, the system answer of the design point x_i must be computed before the variance loop. In fact, this corresponds better to the general idea of outer and inner loops, as presented in Fig. 4.3. In the application chapters, both alternatives are tested. However, since the applications focus on the robustness criterion, Algorithm 3 was defined accordingly.

Chapter 8 presents structural optimisations that employ the two-level MOR approach for robust design. First, the robust position of a hole within a structure experiencing damage is investigated. Hereby, the absolute and robust minima of the objective function are visualised to confirm the effect of the robustness criterion on the optimisation procedure. In a second study, a large-scale industrial optimisation is being carried out: the evaluation of the fibre composite alignment of an aircraft wing. A hyper-reduced model as well as a non-intrusive surrogate are created to find the minimal deformation of the airfoil tip deformation. With the FE model's $200,000$ degrees of freedom, the efficiency gains of the proposed multi-fidelity approach are also exemplified for large-scale analyses.

4.4. Single-fidelity analysis and related work

After elaborating on the multi-fidelity scheme for robust analysis and optimisation, the conversion to single-fidelity and connected multi-fidelity schemes is highlighted. This transformation into a single-fidelity analysis is indicated by the grey dashed boxes in Fig. 4.2 and 4.3. When simplifying the multi-fidelity approach, either the intrusive or the non-intrusive model is applied. The first aim of this thesis is to investigate the overall performance of intrusive MOR in the scope of structural design studies. Therefore, the multi-fidelity scheme is converted to a single-fidelity analysis and the non-intrusive model is neglected or used for comparison. The corresponding Chapters 5 and 6 apply a single-fidelity scheme purely constructing an intrusive reduced order model with global POD and hyper-reduction. The application section starts with an example from the field of crashworthiness in Chapter 5, which also compares the intrusive scheme to the non-intrusive approach to familiarise the reader with both techniques. In the scope of uncertainty propagation, the intrusive approach is showcased in Chapter 6 for natural fibre composites.

For Chapters 5 and 6 the focus lies on intrusive MOR, however, the non-intrusive scheme has also been further investigated by the author in multiple collaborations. In Go et al (2023) a non-intrusive reduced order model successfully represents a human body model in scope of crash analysis. A global POD-based projection is combined with GPR to create a surrogate model for nonlinear transient analyses. Furthermore, the linear projection method is extended with a nonlinear Principal Component Analysis (PCA), the so-called kernel PCA. The surrogate model allowed for a parameter study to prevent injuries caused by the seat belt in crash scenarios. Another collaborative publication is presented in Pretsch et al (2023), in which a non-intrusive model of the pressure field surrounding a compressor blade is used to enable an interdisciplinary design optimisation. For this industrial optimisation problem, a non-intrusive reduced order approach in combination with additional Kriging regression models enables the highly cost-intensive optimisation including structural and fluid analysis.

A multi-fidelity optimisation based on non-intrusive model order reduction has been published in Kaps et al (2022). A hierarchical kriging model introduces a multi-fidelity scheme that adaptively enhances the low-fidelity model within the optimisation study. Within the multi-fidelity scheme, the full-order FE analysis represents the high-fidelity model, and a global POD with kNN-based regression is employed for the low-fidelity model. Applied to automotive crashworthiness problems, a size optimisation for lateral impact, and a shape optimisation for frontal impact is investigated. We could show that the non-intrusive model is well-suited in the scope of hierarchical kriging and accelerates the optimisation algorithm.

Part IV

Applications

Chapter 5

Comparative study of intrusive and non-intrusive model order reduction for crashworthiness

Based on the theoretical background and developed methods, this chapter presents an application of intrusive and non-intrusive MOR for an optimisation study in the field of crashworthiness. It is related to the first class of research questions concerning the benefits and drawbacks of intrusive MOR for parametric nonlinear structural problems. Moreover, the non-intrusive MOR approach is introduced in contrast to the intrusive scheme and complemented by a detailed comparison of offline and online costs for structural optimisation.

The field of crashworthiness requires highly nonlinear analysis and is therefore suitable to test the presented schemes for structural applications. A transient, nonlinear example including contact formulations is conducted to simulate the deformation process of a crash box. First, we introduce the constructed intrusive and non-intrusive models on an exemplary crash box analysis. Hereby, its inter- and extrapolation abilities, and its overall accuracy and speedup are investigated and compared. With an optimisation study, we highlight the benefits and drawbacks of both approaches.

The following chapter is based on the publication Czech et al (2022b), which is partly incorporated or reformulated throughout the text. It is a continuation of the previous Ph. D. thesis of Bach (2020), which was the starting point for this work. For the intrusive MOR scheme, the software LS-Dyna including a special implementation interface, is utilised. The implementation was carried out within a previous work by Bach (2020) and has been extended further to

perform optimisation studies by Mathias Lesjak. The author added the comparative analysis and the design of the optimisation study. A stand-alone Python code holds the algorithm for the non-intrusive scheme, which was developed for this work by the author. Therefore, the Python library Scikit-learn (2022) and SciPy (2022) have been employed for regression and optimisation algorithms.

5.1. Crash box analysis

To assess the two algorithms, a crash box example, similar to the example published by Reid (2000), is introduced. The crash box, as depicted in Fig. 5.9a, is modelled as an elasto-plastic tube with a wall thickness of 2.0 mm and a length of 272.5 mm, whereby imperfections are introduced along the tube to trigger the folding mechanism. A rigid plate with an initial velocity of 40 km/h in the negative z-direction crushes the tube, which is clamped at the bottom.

All deformable parts are discretised with fully integrated Reissner-Mindlin shell elements[1], which have translational and rotational degrees of freedom. In contrast to the element formulation, the remaining contact and material parameters have not changed compared to the template simulation (Reid, 2000). Penalty formulations are applied to model the contact between the plate and the crash box, as well as the self-contact[2]. The material properties for the crash box are as follows: The mass density is $\rho = 7830$ kg/m^3, the Young's modulus is $E = 200$ GPa, the Poisson's ratio is $\nu = 0.30$ and the yield strength is $\sigma_y = 0.366$ GPa with a piece-wise linear plasticity model (see Reid (2000)). The reduced order models are constructed for the tube discretised by 1924 nodes and a termination time of T$= 20$ms is set.

In the following, the intrusive and non-intrusive MOR schemes are applied to the crash box example and their results are compared regarding accuracy and numerical effort. First, we validate the approaches by computing the training accuracy. The measure evaluates the ability to reproduce the training data. However, the main interest lies in the performance on parameters that are not present in the training data presented in Section 5.2.2. Multiple regression models within the non-intrusive scheme are tested. Furthermore, their inter- and extrapolation capabilities are studied, whereby the impacting kinetic energy and the thickness of the crash box are varied. To evaluate their overall computational cost a comparative analysis is presented. In Section 5.3 the reduced models of the crash box are embedded in an optimisation workflow.

[1] LS-Dyna keyword: `ELFORM=16`
[2] LS-Dyna keyword: `CONTACT_AUTOMATIC_SINGLE_SURFACE`

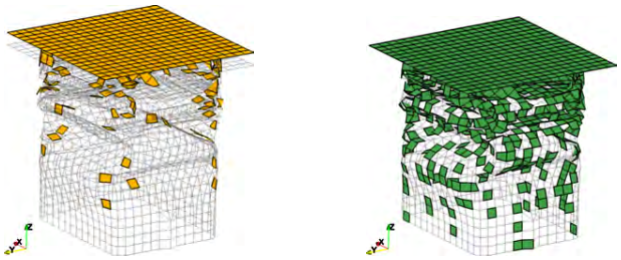

(a) $k = 20,\ \tau = 0.1,$
$\varepsilon_{GMRE} = 8.1\%$

(b) $k = 40,\ \tau = 0.01,$
$\varepsilon_{GMRE} = 0.5\%$

Figure 5.1 The deformed crash box at $t = 20$ ms for two different reduction levels, with the FOM as grey wireframe and the HROM results shown by the coloured elements (Bach, 2020)

5.2. Parameter study for inter- and extrapolation capabilities

5.2.1. Training accuracy

To test the intrusive and non-intrusive scheme for transient analysis, the first study evaluates a model reproducing the training simulation. Therefore, the parameter domain P is neglected and only the time domain T is considered. Uniformly, every $t = 0.01$ ms a snapshot vector of all displacements is allocated to the snapshot matrix.

As the focus is on transient analysis, an error measure considering the full time domain is defined. To evaluate accuracy, the global mean relative error ε_{GMRE} is calculated using full-order displacements $\mathbf{u}$ and reduced order displacements $\mathbf{u_r}$ for the full time domain T as follows:

$$\varepsilon_{GMRE} := \frac{\sqrt{\sum_{t \in T} (\mathbf{u}(t) - \mathbf{V}\mathbf{u_r}(t))^T (\mathbf{u}(t) - \mathbf{V}\mathbf{u_r}(t))}}{\sqrt{\sum_{t \in T} \mathbf{u}^T(t)\mathbf{u}(t)}}. \tag{5.1}$$

For the intrusive scheme, it is referred to Bach (2020) for a detailed description on the implemented MOR employing ECSW (see Section 3.3.2) as hyper-reduction method. Moreover, the projection matrix $\mathbf{V}$ is orthonormalised with respect to the mass matrix and is built for displacement and rotational degrees of freedom separately. The results for the hyper-reduced crash box are summarised in the following. Figure 5.1 shows the results of two crash box simulations computed by the intrusive MOR, whereby the grey wireframe represents the FOM and the orange and green shells indicate the selected hyper-reduction elements for two different reduction levels (Bach, 2020). The parameter k is the number of basis vectors for the ROM, and τ is the tolerance value for the hyper-reduction algorithm in Eq. (3.15). The ROM and the HROM, as depicted in Fig. 5.1, result in computational speedup factors of 4.7 and 7.1, respectively.

To further validate the approach, Fig. 5.2 shows the displacement using intrusive and non-

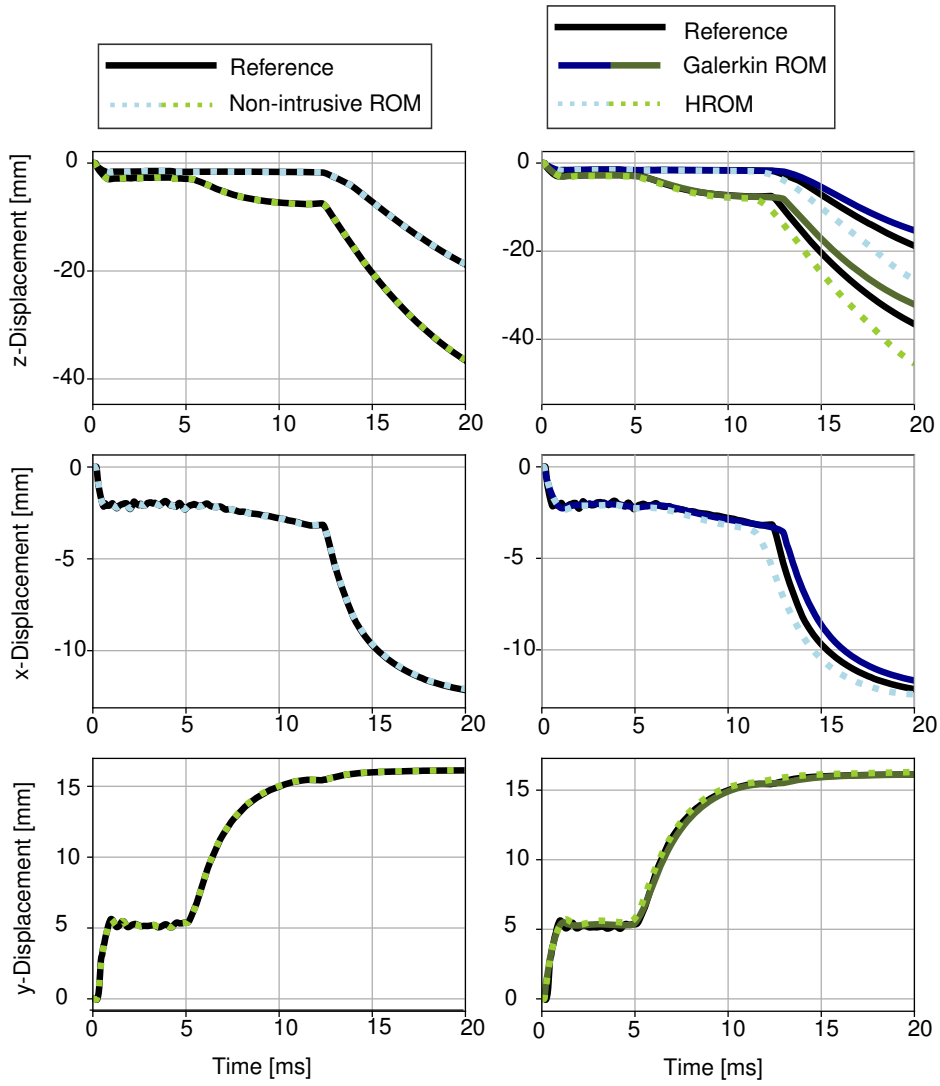

Figure 5.2 Displacement-time curve for two reference nodes (marked in Fig. 5.3 in blue and green correspondingly) using the intrusive ($k = 20, \tau = 0.01$) on the right and non-intrusive ($k = 20$, Matérn kernel) approach on the left.

intrusive MOR of two reference nodes (highlighted in blue and green in Fig. 5.3), which are included in the folding mechanism. The intrusive approach on the right shows the nodal displacement result of the ROM and HROM with larger Δt, as the Galerkin projection leads to a higher critical time step for explicit solvers (Bach et al, 2018).

Next, the Non-intrusive Reduced Order Model (NiROM) model with Gaussian process regression, as introduced in Section 3.4 is constructed. On the left of Fig. 5.2 the results of the reference node are plotted utilising the non-intrusive model with $k = 20$ basis vectors and a GPR with an isotropic Matérn kernel. This example recapitulates the application of the intrusive scheme and illustrates that the non-intrusive regression model can represent the example data. To analyse the quality of non-intrusive models, different regression models are tested with varying input parameter configurations in the next section.

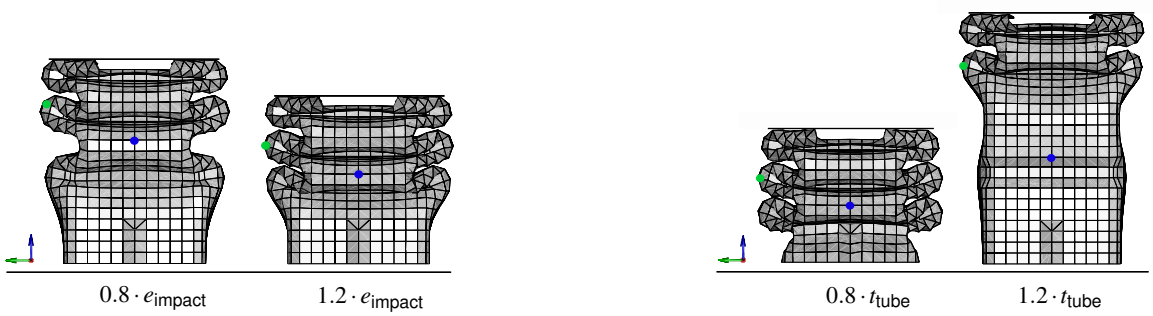

(a) Crash box deformation for a variation of $\pm 20\%$ of the mass of the impacting plate.

(b) Crash box deformation for a variation of $\pm 20\%$ of the tube's thickness.

Figure 5.3 Crash box deformation for a variation of $\pm 20\%$ of the tube's thickness and the impacting kinetic energy realised by a variation of the plate's mass.

5.2.2. Online accuracy

The previous section presented the ability of the MOR schemes to create a simplified model for a nonlinear structural simulation. However, replicating the training simulation is not the intention of the MOR methodology, as no computational efficiency is gained. Considering a multi-query analysis, such as optimisation or probabilistic analysis, the idea is to roughly identify the parameter space and perform a few high-fidelity simulations beforehand. These are utilised for the construction of the reduced model to enable fast online simulations within the multi-query analysis. Therefore, the inter- and extrapolation capabilities within the online phase are the key point for an efficient application. A study investigating two different nonlinear manifolds should illustrate and compare the capabilities of intrusive and non-intrusive models for transient analysis. We first restrict us to a one-dimensional parameter space, whereby a larger design space is evaluated within the optimisation study in the next section.

To illustrate the effect of parameter variations, the kinetic energy of the impacting plate and the thickness of the crash box are identified as suitable variables. For both parameters, individual models are created for a variation of $\pm 20\%$ for all the following studies. To change the kinetic energy applied to the crash box, the mass of the impacting plate is varied by $\pm 20\%$, as it deviates proportionally. The variation in kinetic energy and thickness under constant velocity has a strong impact on the folding mechanism of the crash box depicted in Fig. 5.3. It is also noticeable that the effects of the variation in kinetic energy have a smaller impact on the system than 20% deviation of thickness. By discussing both variables we can investigate the different "levels" of nonlinearity and their effects on the online accuracy.

To analyse the capabilities of reduced order models representing varying manifolds, first a study focusing on the non-intrusive approach is presented. The NiROMs exploiting ML tech-

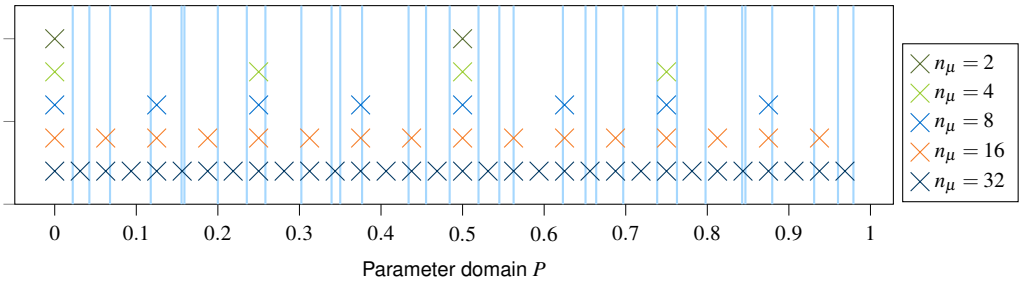

Figure 5.4 Visualisation of training sets $\mu_1, \mu_2, ..., \mu_{n_\mu} \in P$ with varying sample number n_μ for the ROMs $\phi(t, t_{tube})$, $\phi(t, e_{impact})$ corresponding to study of Fig. 5.6 and its 32 test samples, represented by blue lines.

niques PolyR, kNN and GPR are compared individually for the two cases: impacting kinetic energy and thickness of the tube. As the models highly depend on the quality of the training phase, not only the different regression techniques are assessed, but also an increasing number of training simulations.

To judge data-driven meta-models, a prior distinction between training and test data enables the computation of multiple error measures such as the R^2- value or the ε_{GMRE}. A training data set is created by Sobol sampling with an increasing sample set $\mu_1, \mu_2, ..., \mu_{n_\mu} \in P$ with n_μ of 2, 4, 8, 16, and 32. In addition, a testing set of 32 samples is built by a random Sobol sequence, whereby each number is multiplied by a scaled random value. The distribution of the corresponding training and test samples is shown in Fig. 5.4, whereby the test points are highlighted with vertical blue lines.

The training and testing configurations are scaled for the parameter space thickness of the crash box $t_{tube} \in P$ and energy of the impacting plate $e_{impact} \in P$. Full-order analyses are simulated accordingly and snapshots are collected uniformly every 0.1ms. Five NiROMs $\phi(t, t_{tube})$ are individually built for the sets of 2, 4, 8, 16, and 32 training points n_μ, whereby each simulation contributes 200 snapshots $t_1, t_2, .., t_{200} \in T$. To create five NiROMs $\phi(t, e_{impact})$ the procedure is repeated. All models are based on a reduced subspace with $k = 20$ basis vectors.

In Fig. 5.6 the displacement ε_{GMRE} of Eq. (5.1) is plotted, as an error measure for all 32 test samples. The bar is drawn from the smallest to the largest ε_{GMRE} and the mean of all samples is highlighted individually by a marker for kNN, PolyR and GPR. For all models, the accuracy increases with the number of training simulations. One can notice that the PolyR models of order seven, constructed from two training simulations do not provide useful surrogates, possibly due to overfitting. Despite this exception, the regression techniques kNN with five neighbours, PolyR and GPR using an anisotropic Matérn kernel show an ε_{GMRE} in similar ranges.

Table 5.1 compares the ε_{GMRE} and R^2 for the models $\phi_8(t, t_{tube})$ and $\phi_8(t, e_{impact})$ built from 8 training simulations for all three ML techniques. It is noticeable, that the GPR performs

Table 5.1 Comparison of mean error measures R^2 and $GMRE$ for varying NiROMs with a subspace $k = 20$ and PolyR (p = 7), kNN (k = 5), GPR (anisotropic Matérn kernel) for 8 training simulations and 32 test simulations.

	PolyR		kNN		GPR	
	t_{tube}	e_{impact}	t_{tube}	e_{impact}	t_{tube}	e_{impact}
R^2	0.981	0.992	0.900	0.995	0.994	0.999
ε_{GMRE}	1.93	1.20	1.25	0.87	0.36	0.28

best in the framework of non-intrusive MOR with a ε_{GMRE} of 0.28% and $R^2 = 0.999$ for the parameter space e_{impact}. For this example, the models built by kNN have a higher accuracy than those obtained by polynomial regression. As the kNN technique averages a data point with the k-nearest neighbours, its quality to approximate the very first and last time step is reduced. The performance of kNN trained on sparse data, especially in the time domain can drop significantly, as also observed by Kneifl et al (2021). However, kNN is a fast and robust technique and especially for high number of data points a simpler regression model can be beneficial.

Comparing R^2 and ε_{GMRE} for the different parameter domains, all $\phi(t, e_{impact})$ regression models show a higher R^2 than $\phi(t, t_{tube})$. This can also be observed in Fig. 5.6 for models with increasing training sets. On the left, $\phi(t, t_{tube})$ models have continuously higher ε_{GMRE} as $\phi(t, e_{impact})$ surrogates. As a smaller range of displacement patterns (Fig. 5.3) corresponds to the variation of the impacting kinetic energy e_{impact}, this could be expected.

To further understand the particular meta-models, Fig. 5.5 visualises the displacement in x, y, and z-direction of the first test simulation for two folding points (marked in Fig. 5.3). Similar to the Table 5.1, PolyR, kNN, and GPR are based on snapshots from 8 transient training simulations and a subspace of $k = 20$ basis vectors. An artificially smooth function can be observed for the polynomial regression of order seven. Compared to the other techniques, GPR using an anisotropic Matérn kernel has superior accuracy and is able to depict more irregular data points, as also exploited by Guo and Hesthaven (2019).

The next study compares the non-intrusive to the intrusive approach for varying parameter domains. For the intrusive MOR the question rises if the projected system of equation enables an extrapolation of design variables. Therefore, the projection matrix is constructed from a single training simulation and tested in the online phase with extrapolating design variables. The displacement ε_{GMRE} by Eq. (5.1) of the intrusive MOR are plotted on the right of Fig. 5.3a and Fig. 5.3b. The model is trained, collecting snapshots every 0.01ms, using a plate mass of 150 kg and a wall thickness of 2.0 mm. It can be observed, that the error increases with the distance to the training configuration. Also the relative error due to a change in wall thickness is generally higher than the error associated with a change of the plate's mass. This further supports the observation of higher nonlinearities associated with a varying tube thickness.

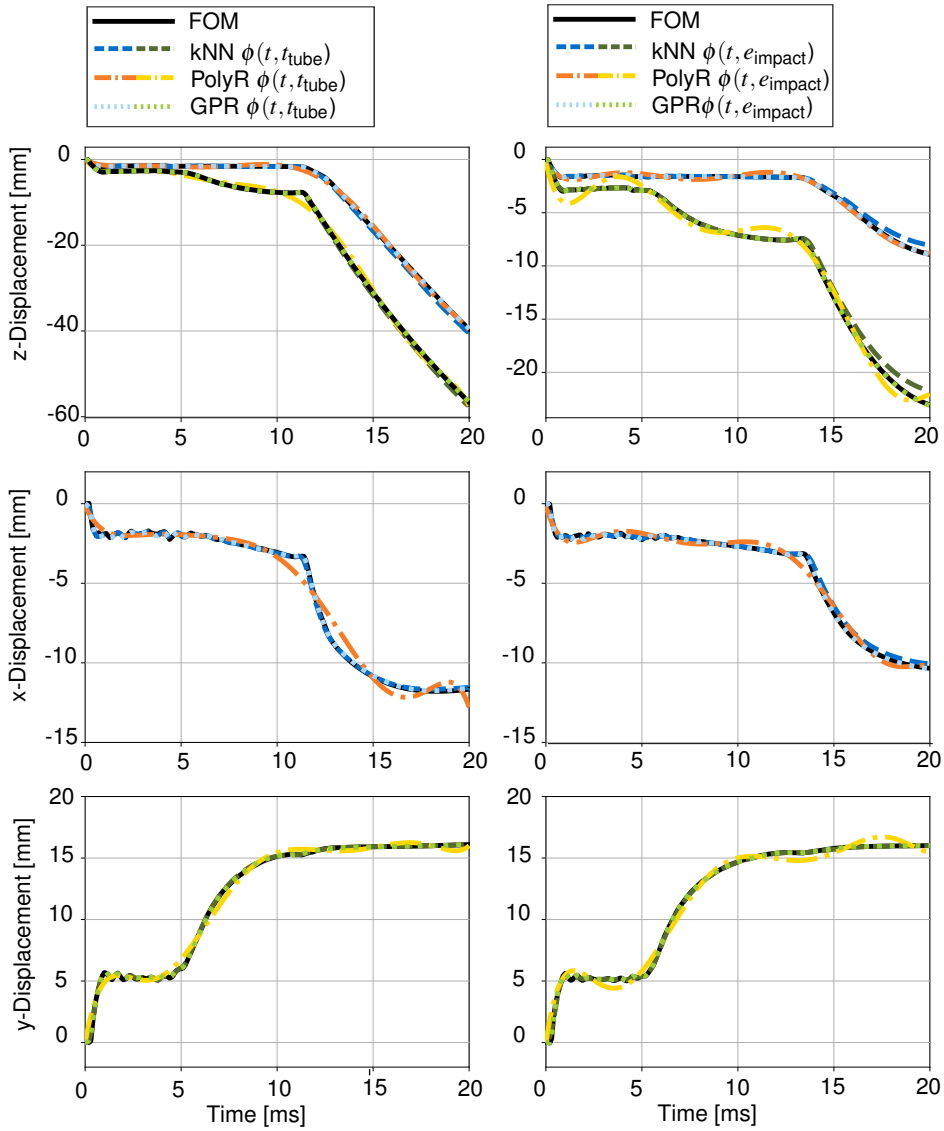

Figure 5.5 Displacement-time curve for two reference nodes (marked in Fig. 5.3 in blue and green correspondingly) for NiROMs with varying regression models PolyR (p = 7), kNN (k = 5), GPR (anisotropic Matérn kernel) and a subspace $k = 20$. The model with varying tube thickness $\phi(t, t_{tube})$ is displayed on the left and the model for different impact energies $\phi(t, e_{impact})$ is shown on the right.

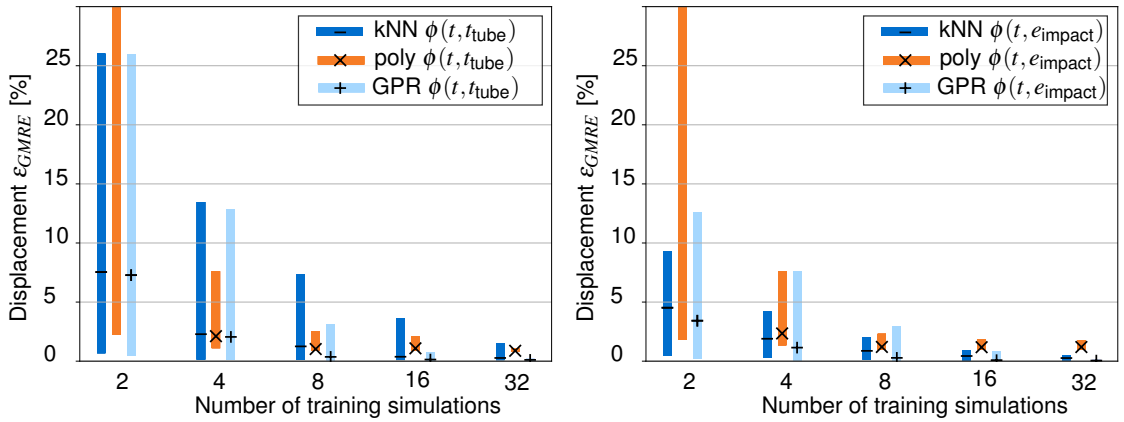

Figure 5.6 Displacement ε_{GMRE} of 32 test simulations and its mean for varying NiROMs with a subspace $k = 20$ and PolyR (p = 7), kNN (k = 5), GPR (anisotropic Matérn kernel) for sets of 2, 4, 8, 16, 32 training simulations. The ε_{GMRE} for models with varying tube thickness $\phi(t, t_{tube})$ are displayed on the left and the models for different impact energies $\phi(t, e_{impact})$ are shown on the right.

In contrast to the small extrapolation capabilities of the intrusive ROMs, the non-intrusive scheme is restricted to interpolation. Training a non-intrusive model with snapshots corresponding to one parameter instance would yield unreasonable results, as the surrogate is essentially a regression model and only enriched by physical phenomena. For a comparison of the techniques, the minimum number of training simulations to reach a similar accuracy level is investigated. The snapshot time increments are enlarged to 1ms, such that a total number of 20 snapshots are collected from each transient analysis. The number of training simulations was successively increased until the non-intrusive ROMs achieved ε_{GMRE} in the same range as the intrusive approach. As for non-intrusive models the computational cost mainly depends on the number of training simulations; this is an important factor to compare the overall efficiency gains.

On the left of Fig. 5.3a and 5.3b the displacement ε_{GMRE} of the non-intrusive MOR results are depicted. The training samples are obtained by Latin hypercube sampling and marked with grey circles in Fig. 5.3a and 5.3b. Hence, three training simulations are needed for varying mass and thirteen for varying thickness, in order to obtain similar error values compared to the intrusive MOR method. As already observed before, the accuracy of the simplified model strongly depends on the nonlinear manifold and the quality of the training phase. Note that for the variation of thickness in Fig. 5.3b the number of training data rises to thirteen, which would be equivalent to an increasing online error while keeping the same number of training simulations.

It could be shown, that non-intrusive ROMs are capable of representing the crash box example, whereby especially kNN and GPR provided reliable regression models. The GPR is the most accurate technique and kNN is favourable in terms of efficiency and robustness. Moreover, the accuracy of ROMs highly relies on the amount of training simulations and snapshot intervals in time and parameter domain. Note that the characteristic change in time and

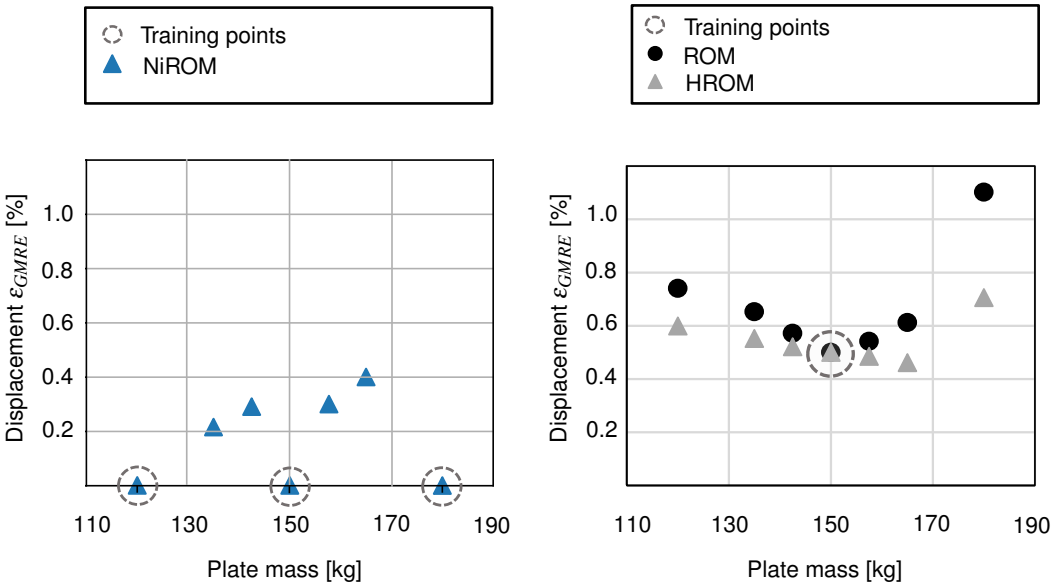

(a) Overall displacement ε_{GMRE} for ROM, HROM and NiROM with varying mass of the impacting plate.

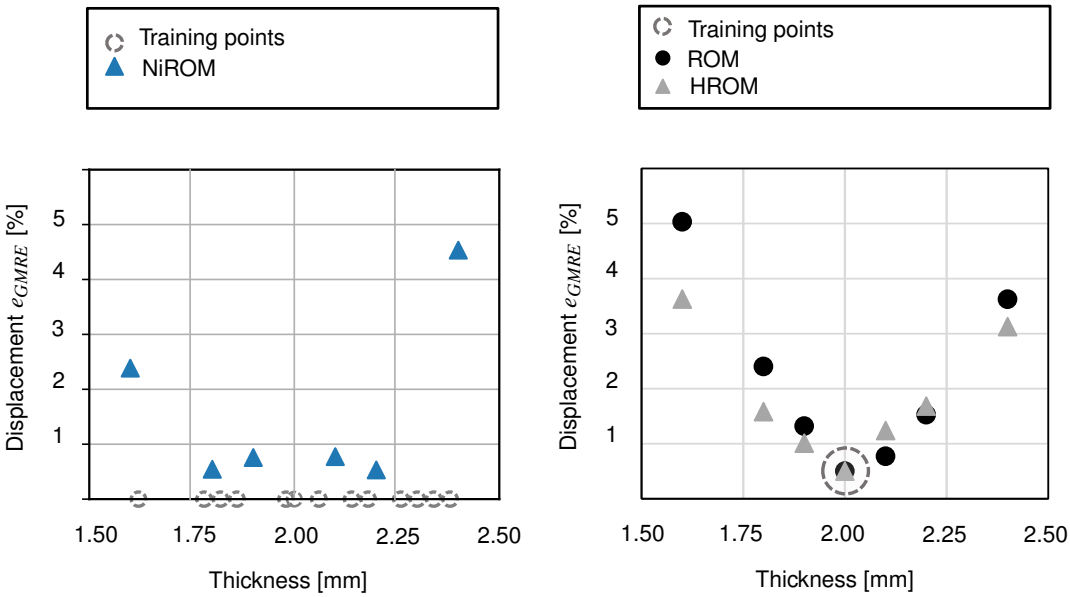

(b) Overall displacement ε_{GMRE} for ROM, HROM and NiROM with varying thickness of the crash box.

Figure 5.7 Comparison of the displacement ε_{GMRE} with parameter variation of intrusive (Bach, 2020) and non-intrusive models (anisotropic Matérn kernel) with a subspace $k = 40$.

Table 5.2 Elapsed time for the crashbox example of Fig. 5.7 comparing FOM, ROM and HROM (Bach, 2020) and NiROM

FOM	ROM	HROM	NiROM
56.55s	20.75s	11.95s	0.01s

parameter space defines the nonlinear manifold and therewith the required training set. A comparison to the intrusive approach illustrates, that similar accuracy can be achieved by non-intrusive ROMs with a higher number of training data. For the intrusive ROMs of the crash box, extrapolation within the parameter domain is possible for a 20% range, however a general conclusion cannot be drawn from this example analysis. Further studies in the field of crashworthiness are required to display a comprehensive picture.

5.2.3. Computational cost

After examining the accuracy of the models, we now focus on the computational speedup of the reduced models. The construction cost of the machine learning model is negligibly small compared to the evaluation of the training simulations for all techniques. One ROM evaluation using kNN or PolyR is 4 orders of magnitude and for GPR 3 orders of magnitude smaller than a full-order analysis. However, for a higher number of DOFs, but especially for a higher number of design parameters and snapshots, the cost of constructing a Gaussian Process can significantly increase. For a detailed comparison of online and offline costs for the different ML techniques in the scope of crashworthiness it is also referred to Kneifl et al (2021).

Here, we focus on the comparison of costs of the intrusive and non-intrusive method. Table 5.2 shows the elapsed time for the crash box example of Fig. 5.7. The single online simulations of the corresponding ROMs are measured on an Intel Xeon 3.5 GHz processor with 4 CPUs. The intrusive scheme has a speedup factor of approximately 4.7 and the non-intrusive scheme with GPR is of 3 magnitudes faster than the FOM. However, including the offline phase into the evaluation of the computational cost the results appear to be different. Figure 5.8 compares the cost function of intrusive and non-intrusive with $\phi(t, e_{impact})$ and $\phi(t, t_{tube})$, in grey, blue, and green respectively. The x-axis shows the number of online evaluations, whereby the start represents the training effort. The values on the y-axis are normalised by the computational cost of one full-order simulation. Thus, the intrusive training cost equals to 1 and the non-intrusive to 3 and 13. With a speedup factor of four and 10^4, the efficiency of the non-intrusive scheme overtakes the performance of the intrusive for 10 and 57 online evaluations of $\phi(t, e_{impact})$ and $\phi(t, t_{tube})$ respectively. Note that the costs of SVD and hyper-reduction are neglected here and the speedups of the intrusive MOR highly depend on the specific implementation (Bach, 2020).

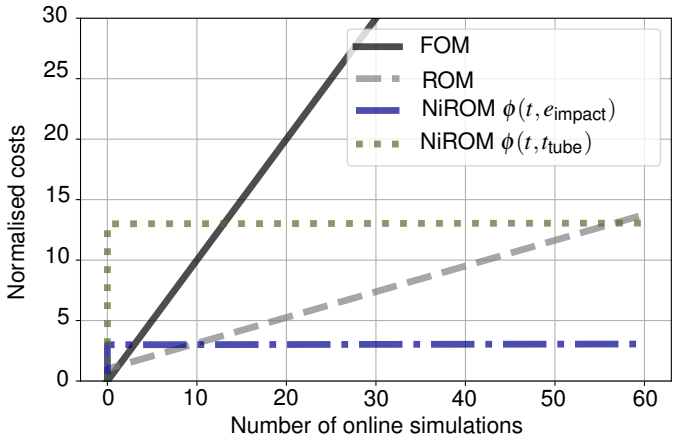

Figure 5.8 Normalised computational cost for the crash box example of Fig. 5.7 comparing full-order simulation (FOM) intrusive (Galerkin ROM and HROM) and non-intrusive ROM for an increasing number of online simulations.

5.3. Optimisation study

The previous section evaluated the effects of training parameters on the online accuracy exemplarily for the crash box example. Next, an optimisation is proposed to further illustrate the capabilities of the presented schemes. Therefore, the crash box is adapted for a dimensional optimisation of tailor welded blanks. The automotive industry discovered that for thin-walled structures tailor welded blanks can be exploited to improve its lightweight and crashworthiness properties simultaneously (Fang et al, 2017). The task is to combine multiple blanks with different thicknesses or material properties to a single structure to enhance its mechanical behaviour. In literature, multiple optimisation studies searching for the best thickness distribution of welded (Chen et al, 2019; Xu et al, 2014) or rolled (Duan et al, 2016; Sun et al, 2017; Klinke and Schumacher, 2018) blanks can be found. All optimisation schemes commonly employ surrogate models such as radial basis functions (Klinke and Schumacher, 2018; Sun et al, 2017) or support vector regression (Duan et al, 2016). Here, the two MOR schemes are used as surrogate models during an optimisation analysis, inspired by (Chen et al, 2019), but utilising a differential evolution algorithm. Notice that we focus on the performance of the surrogate models in a realistic application rather than the finding of new results of the optimisation study itself.

For the optimisation the crash box is divided into three circles representing three blanks, as shown with the colour highlighted parts in Fig. 5.9a. Starting from the top, the thickness of the first ring t_1 and the second ring t_2 are unknown design parameters, whereby t_3 is assumed to be of constant thickness of 2 mm. The blanks are simplified to rings, whereby the transition zones are neglected, such that the design parameters $x = [t_1, t_2]$ are varied in the range from $x^l = 1.0$ to $x^u = 2.0$ mm. In addition, the mass of the impacting plate m_{plate} is set as a design variable with a range of $80 - 170$kg. The termination time is extended to 35ms, such that the tube is completely folded for all possible choices of design variables.

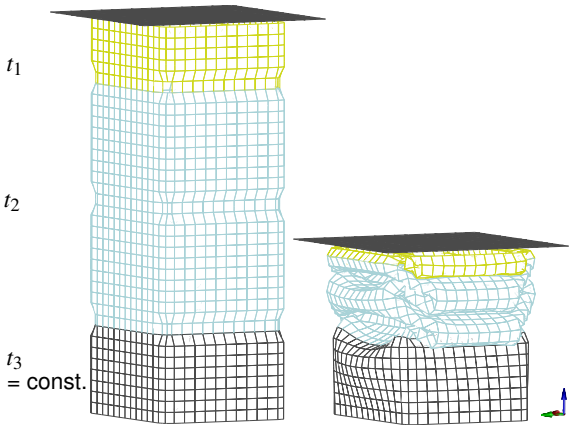

(a) Initial and folded crash box of the optimisation study at $t = 0$ms and $t = 35$ms with optimised design variables $t_1 = 1.08$mm and $t_2 = 1.85$mm.

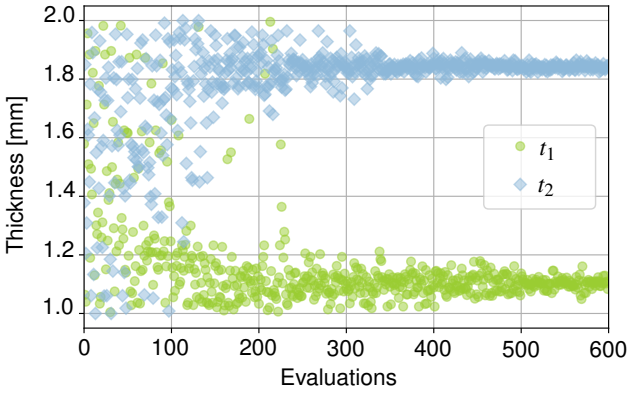

(b) Convergence of the design variables t_1 and t_2 of FOM reference optimisation with a population size of 18 and recombination factor 0.7 terminated after 646 iterations.

Figure 5.9 Optimisation study of a folded crash box minimising $f(x)$ of Tab. 5.3 with design variables t_1 and t_2.

Table 5.3 Combined objective functions with corresponding weights $f(x) = w_1 f_1 + w_2 f_2 + w_3 f_3$ for the optimisation study.

Objective	Function	Weights
↑ Energy	$-f_1(m,v) = \frac{1}{2} m_{plate} v^2$	2
↓ Acceleration	$f_2(u,t) = u(t) - \frac{u_{max}}{T^2}(t-T)^2 - u_{max}$	1
↓ Mass	$f_3(t_1,t_2) = (2t_1 + t_2)\rho$	2

As a first objective the kinetic energy of the impacting plate should be maximised, which is denoted by the objective f_1 in [J]. Secondly, the acceleration $a(t)$ and force $F(t)$ resulting from the impacting plate are expected to be constant for optimal crashworthiness designs. Therefore, the objective function includes a term corresponding to the displacement curve over time $u(t)$ of the impacting plate. Starting from $t = 1ms$, the displacement of the middle node of the impacting plate is observed, whereby the peak forces are neglected here. Transferring the objective to the accelerations $\ddot{u}(t) = a(t)$, the deviation to the ideal quadratic displacement curve (i.e. related to a constant acceleration) is minimised with the second objective function $f_2(u,t)$ in [mm]. A conflicting requirement is a light weight structure, therefore also the mass of the crash box is minimised with $f_3(t_1,t_2)$ in [mm]. Thus, the total objective function $f(x) = w_1 f_1 + w_2 f_2 + w_3 f_3$, with the weights w_i, as shown in Table 5.3, maximises the energy absorption and minimises the acceleration and mass to improve the crash box design. Note that normalised values of $f_1 - f_3$ are combined, to avoid problems due to dissimilar units. The optimisation algorithm terminates if the tolerance $\varepsilon < 0.01$, a population's standard deviation divided by the average of its energy, or a maximum iteration number is reached.

First the study was performed with the FOM and repeated for ten runs with varying population sizes $(12-21)$, recombination factors $(0.7-0.9)$ and max. iteration numbers $(30-50)$ to obtain a reference solution. The resulting thicknesses t_1 and t_2 of all 10 runs are similar, and the mean is listed in Table 5.4. The thickness of the first ring t_1 is at the lower boundary

Table 5.4 Average optimised design variables for the thickness of ring t_1, ring t_2 and the mass of the impacting plate m_{plate} comparing FOM, ROM, and NiROM

Design Variable	t_1	t_2	m_{plate}
Range	1.0 - 2.0 mm	1.0 - 2.0 mm	80 - 170 kg
FOM	1.08 mm	1.85 mm	170 kg
ROM	1.00 mm	1.80 mm	170 kg
NiROM	1.05 mm	1.87 mm	170 kg

of the range and the second ring t_2 at the upper limit, which also relates to the ideas of an optimised crash box by Chen et al (2019). Corresponding to the objective f_1 of maximising the kinetic energy, the mass of the plate m_{plate} has reached the upper range. Exemplarily, the convergence of the design parameter t_1 and t_2 with a population size of 18 is displayed for 600 evaluations in Fig. 5.9b and the corresponding deformed crash box is depicted in Fig. 5.9a. In Fig. 5.10, the objective function is plotted over the full two-dimensional design space t_1 and t_2 and in the vicinity of the optimum. Within the design space, 200 points are analysed by full-order simulation and the minimum is marked. The results of the optimisation algorithm can be confirmed by the clear minimum of the objective function observable in Fig. 5.10.

Next, the optimisation is performed with the intrusive and the non-intrusive MOR scheme. For the non-intrusive scheme 150 training simulations are created with a Latin hyper cube sampling corresponding to the ranges of the three design variables. The subspace is spanned by 50 basis vectors, and a GPR with an anisotropic Matérn kernel is optimised to create the meta-model. The averaged results of the design variables are also listed in Table 5.4. In addition, the optimised values of the intrusive MOR scheme using Galerkin projection are plotted in green. It is built with 30 training simulations and setup by 50 degrees of freedom in the reduced space.
Both approximation methods can replicate the overall minimum and result in similar optimised design variables. The error of the optimised design variable lies in the range of $0.1 - 7.0\%$. However in other regions, especially at the borders of the design space the system answers deviate more from the reference solution. The interested reader is referred to Fig. 5.10, which depicts the objective function over the design space t_1 and t_2 with $m_{plate} =$ 170kg. The approximation by the intrusive scheme has a larger area of low objective values in the vicinity of the minimum and therefore shows less robust optimisation results in comparison to the non-intrusive approximation. This also explains that the intrusive MOR has a higher error than the non-intrusive approach, which is in contrast to the previous studies of Section 5.2.2, e.g. Fig. 5.7.

The former analysis included ROMs for a single parameter, whereas for the optimisation a parameter space of dimension three is spanned. Within the construction of the intrusive ROM it was noticeable, that the enlarged parameter space reduces its accuracy significantly, as

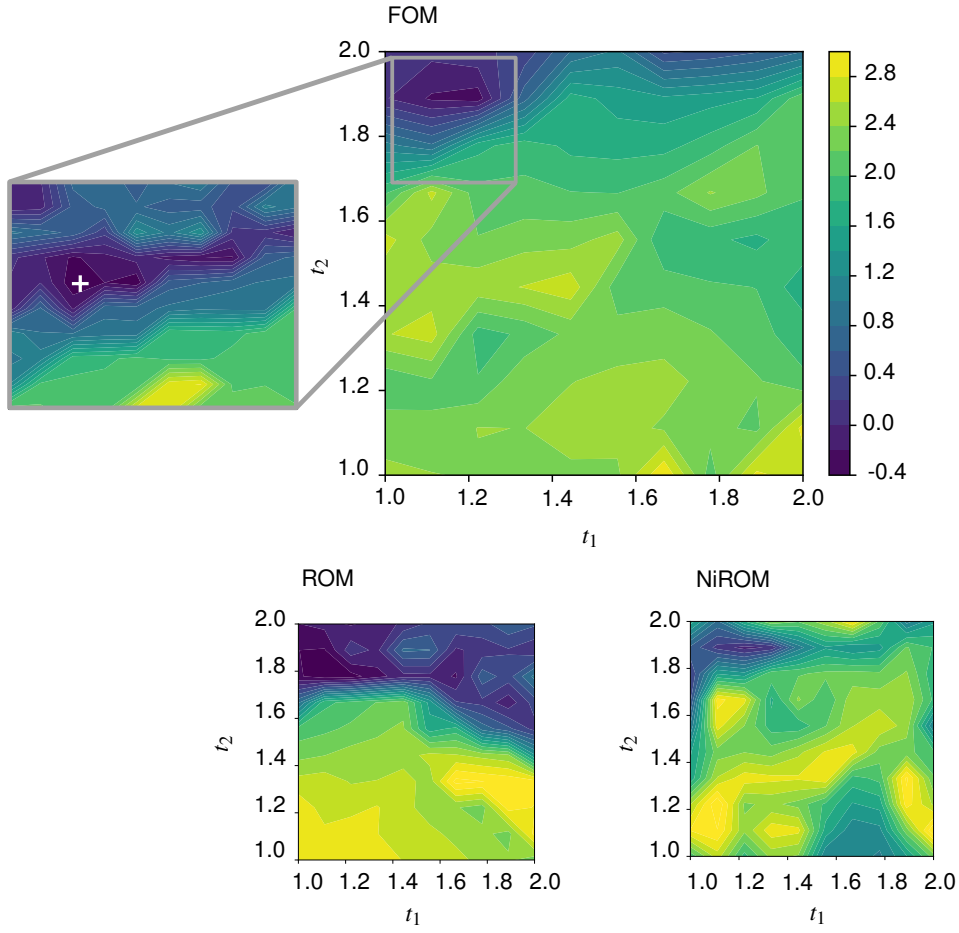

Figure 5.10 Objective function plotted over the design space t_1 and t_2 for $m_{plate} = 170$kg computed by full-order reference simulation, intrusive and non-intrusive model with 100 samples points. The minimum is indicated with a white cross.

more variance is present in the data and therefore more basis vectors in the reduced basis have to be considered. Hereby, the subspace projection restricts the intrusive MOR capturing higher parameter spaces, also observed by Bach (2020). As the projection is the decisive reduction step, only Galerkin ROM is utilised for the optimisation study. Since intrusive and non-intrusive methods differ in speedup by the order of 4 in magnitude, this limitation does not affect the conclusion of this study and the estimate presented in Section 5.2.3 is reasonable.

5.4. Concluding remarks on MOR for crashworthiness analysis

Within this chapter, data-driven MOR techniques for structural transient, multi-query applications were discussed. We focused on intrusive MOR, which projects the system of equations into a reduced subspace in comparison to a non-intrusive approach, a pure data-driven technique. The main interest lies in their applicability and efficiency within optimisation schemes for crashworthiness.

Through a sensitivity study the inter- and extrapolation abilities of intrusive and non-intrusive MOR were compared for a crashworthiness example. In comparison to the non-intrusive MOR methods, intrusive MOR is able to extrapolate input parameters in a small range, and needs fewer training simulations than non-intrusive. Additional modifications to the solver are needed, which increases the complexity of implementation and normally excludes the usage of commercial FEM solvers. In contrast, non-intrusive methods are easier to implement and lead to much faster online evaluations. They need generally more training simulations to achieve acceptable accuracy and are more sensitive to hyperparameter changes.

Moreover, a parameter study illustrated the performance of non-intrusive approaches in relation to its training set, whereby the performance strongly depends on the nonlinearity of the underlying manifold. In general, non-intrusive ROMs require a large amount of training data and its efficiency is only ensured if the number of training simulations does not exceed that of the online evaluations of the multi-query analysis.

With an exemplary optimisation study, we could show that the MOR scheme is able to perform efficient multi-query analyses for structural, highly nonlinear problems. The invested cost of constructing the reduced order models is compensated in the online phase, where the population-based optimisation algorithm evaluates the model in an iterative manner. Considering online and offline expenses, the optimisation via MOR results in significant speedups.

Multiple aspects of intrusive and non-intrusive MOR are still challenging and require further analysis. For non-intrusive MOR, the regression model can suffer from overfitting or sensitive hyperparameters. Moreover, the number of training simulations has a large impact on the quality of the subspace. Both points can lead to an unstable model, which was, however, not observed as a high challenge within this study. An additional hyperparameter study for the non-intrusive regression models can be found in Section 8.2 for a sparse data regime. Following the nature of a data-driven approach, non-intrusive MOR can only be applied for online simulations interpolating between the parameter configuration of the training simulations.

As shown in Section 5.2.2 the intrusive MOR scheme also enables extrapolation as a higher amount of physical knowledge is included in the model. However, one can notice that the optimised design variables deviate from the reference solution by up to 7%, which can be critical for certain applications. Since an optimisation requires large parameter variation, a global POD was used to combine training simulations within the parameter space. During the performed analysis one could observe that the dimension of the subspace must be increased if the design space is enlarged. Thus, the global POD can be critical as it destroys the optimal approximation property of Galerkin projection. A detailed discussion of the Galerkin projection and optimality can be found in Carlberg et al (2017). In addition, if the underlying manifold is nonlinear, it is critical to fit a low-dimensional hyper-plane through the data with a linear method.

The results show that especially the non-intrusive MOR is capable of being used in applications with considerable parameter changes, although extrapolation should be avoided. In contrast, the intrusive ROM shows slight extrapolation and interpolation capabilities (see Section 5.2.2), however, when increasing the number of design parameters especially the presented intrusive scheme reaches its limits. In summary, the application of intrusive and non-intrusive MOR leads to reasonable results for the presented optimisation study, but can be critical for large parameter spaces with underlying highly nonlinear manifolds. In the field of crashworthiness only smaller test cases have been conducted, the application to a full-scale crash simulation is still missing.

Chapter 6

Intrusive model order reduction for spatially varying material properties - application to wooden fibre composites

This chapter applies the reduced order models for structures with spatially varying material properties. It is concerned with the first research aim of investigating intrusive MOR in a single-fidelity analysis scheme. We investigated its general applicability for the nonlinear analysis of structures under damage. Furthermore, the potential of intrusive MOR is explored for the quantification of uncertainties using probabilistic methods.

Therefore, natural fibres, in particular wood, are presented as another challenging application in the field of structural mechanics. On the basis of experimental data, the inhomogeneous material properties are quantified with random fields. In contrast to the other applications, the analysis is complemented by elaborating on the uncertainty field based on an experimental data set. Moreover, the construction of reduced order models for spatially varying material properties is proposed. The parameter space associated with the random process is investigated with varying examples, and its effect on the construction phase is highlighted. The application complexity is increased until a low Kolmogorov n-width is reached, to show the limitations of the classical linear projection. Finally, an MC analysis illustrates the application of intrusive MOR in the scope of uncertainty propagation.

The intrusive MOR approach is realised with *Kratos Multiphysics* an open source FEM algorithm (Mataix Ferrándiz et al, 2020; Dadvand et al, 2013, 2010). We were in close collabora-

tion with the International Centre for Numerical Methods in Engineering (CIMNE) in Barcelona, Spain, in particular Raul Bravo, who developed the core MOR application. Within *Kratos Multiphysics* the ECM is employed as a hyper-reduction technique. For this work, the author extended the MOR implementation for spatially varying material properties. A random field algorithm for geometrical imperfections, see Messmer (2020), was modified to follow the proposed workflow. Furthermore, the uncertainty quantification was implemented in an external Python application to communicate with the FE solver results.

6.1. Reduced order models for spatial uncertainties

The construction of classical surrogates, such as response surface models, is impractical for an analysis with heterogeneous material, as the dimension of inputs depends on the spatial field, a high-dimensional parameter space. To nevertheless enable multi-query analysis, MOR techniques are proposed as simplified models with spatial uncertainties.

Both spatial uncertainties and reduced order models require a preparation step before the actual analysis can be executed. For this reason, Fig. 6.1 shows the complete workflow divided into an offline or training phase and an online phase. For spatial uncertainties, random field properties are extracted from the measurement data, as introduced in Section 6.2. More precisely, the correlation function of Eq. (2.12) is set up and its eigenvalue analysis is performed to discretise the process. The defined random field shall then model the heterogeneous material properties of the structure. A realisation of the random field can be interpreted as an artificially created sample board and is used as an input to the FE analysis of the training simulations. To construct a reduced order model, a snapshot matrix of training simulations is created, and the projection matrix is extracted via SVD using Eq. (3.4). In addition, the elements and weights for the hyper-reduced model are computed with the ECM procedure explained in Section 3.3.2. Random field and hyper-reduced order model (HROM) are the results of the offline phase and will be further utilised in the online phase.

During the MC analysis the reduced order model is evaluated in an iterative loop. Each realisation of the random field will produce a different input for the HROM model, which can be evaluated efficiently. Hereby, the speedup results from the reduced number of unknowns in the projected system and the lower number of elements selected through hyper-reduction. After all MC samples are computed, the statistical properties of a performance quantity are extracted. Thus, with a reasonable amount of simulations, an estimated expected value and a standard deviation of the quantity of interest can be computed. In the following section, the different aspects of the proposed scheme are highlighted by exemplary test studies.

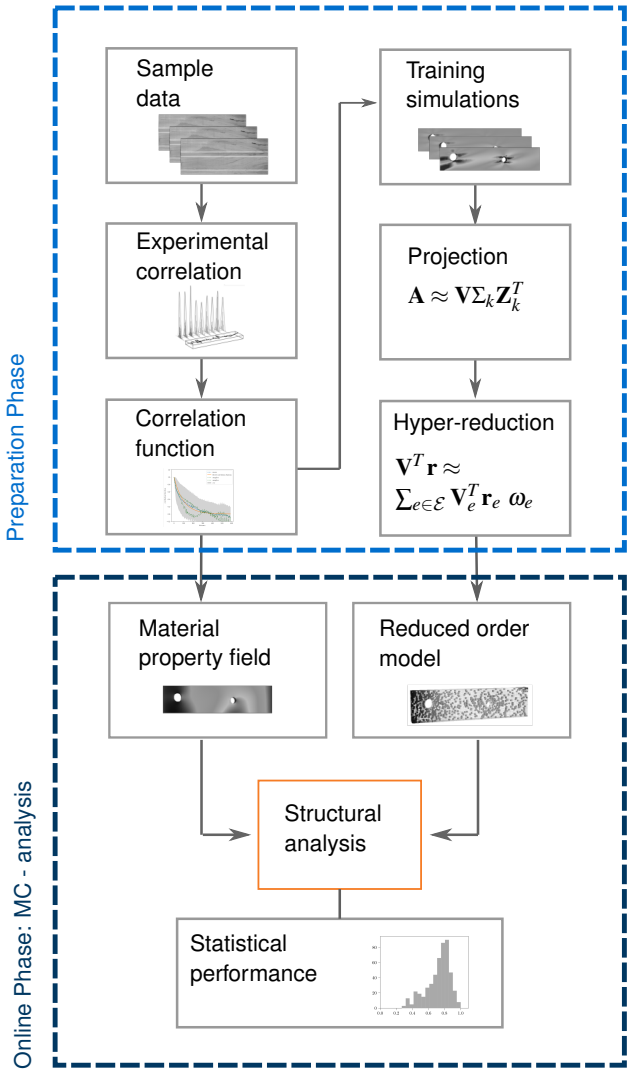

Figure 6.1 Proposed workflow for generating and evaluating spatial uncertainties, divided into a preparation phase (or offline phase) and an online phase in which the MC analysis is performed.

6.2. Random field approximation by experimental data base

After introducing Gaussian processes and its discretisation, the main question remains how to define the correlation function. Within this approach, a measured data set, presented in Section 6.3.1, is utilised to identify a suitable correlation function. Thereby, the correlation function can be extracted from experimental data points, which capture the spatial variations. This technique is commonly used in soil mechanics, e.g. Lloret-Cabot et al (2014); Luo et al (2019); Oguz et al (2019) and originates to Vanmarcke (2010). The data points of each sample are normalised so that mean $\mu = 0$ and standard deviation $\sigma = 1$ are met. Within the data set an equivalent distance Δd is required. For each distance $k\Delta d$ with $k = 1,2,...,n-1$ data points $\hat{x}$, the experimental correlation function can be calculated by

$$\hat{f}_c(k) = \frac{\sum_{j=1}^{n-k}(\hat{x}_j - \mu_j)(\hat{x}_{j+k} - \mu_{j+k})}{\sum_{j=1}^{n-k}(\hat{x}_j - \mu_j)^2}, \tag{6.1}$$

for one sample. Thus, all data points $\hat{x}$ with the same distance k are averaged and compared with the mean of all samples μ. With increasing distance k less data points are available and its interpretability becomes questionable, e.g., for the distance $n-k$ only one data pair is available to verify its correlation. Therefore, large distances are neglected and only distances k divided by a ratio r are used to evaluate the correlation function. To generalise the extracted correlations, we next approximate an analytical function to the data set. To fit an analytical correlation function f_c and the correlation length l_c with an isotropic exponential kernel, Eq. (2.12) can be reformulated depending on the distance d

$$f_c(k_i) = \exp\frac{-k_i\Delta d}{2l_c}. \tag{6.2}$$

In theory, any other kernel function could also be chosen. To fit the analytical function f_c the error e

$$e = \sum_{i=1}^{n-1} f_c(k_i) - \hat{f}_c(k_i), \tag{6.3}$$

with respect to the experimentally computed correlation function $\hat{f}_c$ is minimised. With the extracted correlation length and function, Eq. (2.12) can be defined.

6.3. Wooden structures with spatial uncertainties

This section presents two test cases with properties of non-homogeneous natural fibre-based material to illustrate the proposed scheme. Referring to a realistic example, beech wood is selected as the natural fibre material on which all studies in this chapter are based. According to the workflow of Fig. 6.1, three key areas contribute: the construction of the random field, the reduced order model, and the MC analysis. The structure of the following section follows these three topics.

First, we construct a random field based on a data set of varying fibre angles of beech timber boards. Thus, we restrict ourselves to boards without knots. The assumption of characterising the material properties of beech timber boards as a random field with normal Gaussian distributions is explained in Section 6.3.1. In Section 6.3.2 reduced models for spatially varying material properties are created. With the help of a wooden test case, the accuracy and efficiency of the models are discussed in detail. To investigate the performance of a probabilistic analysis via MOR techniques, a second test case, a beam under bending experiencing damage, is introduced. Benefits and disadvantages are discussed in Section 6.3.3 to evaluate the overall scheme.

6.3.1. Material properties of European beech characterised by fibre angles

Natural fibre-based material shows anisotropic and heterogeneous material properties, which strongly depend on the variation of environmental conditions. Therefore, timber boards are usually modelled with orthotropic material properties following the directions of the fibre, as shown in Lukacevic et al (2019). The number of knots and the resulting fibre deviation in wooden boards strongly influence their mechanical responses. Therefore, a homogeneous material model is not sufficient to realistically model the material behaviour.

In the research area of wood, the spatial correlation of mechanical material properties have been investigated and compared. In the early stage, the strength or stiffness values of neighbouring sections were analysed with physical experiments to compute its correlation (Brandner and Schickhofer, 2014; Bulleit and Chapman, 2004). More recently, continuous parameter space models (Kandler et al, 2015), often quasi-continuous models but with higher resolution as the previous studies have been developed. Hereby, quasi-continuous data of the material properties in two or three dimensions are measured by, e.g. laser scanning devices. By means of virtual strength grading methods, the stiffness properties of individual boards are predicted (Khaloian Sarnaghi and van de Kuilen, 2019; Lukacevic et al, 2019). In addition, spatial correlations have been investigated statistically, however, only for material properties in one dimension, in particular, the modulus of elasticity (García and Rosales, 2017; Kandler and Füssl, 2017). Another line of research defines strong and weak regions, based on discrete

Figure 6.2 Exemplary beech board with varying fibre direction along the board, resulting in inhomogeneous material properties.

knots, and evaluates their statistical variation, e.g. Fink et al (2015); Isaksson (1999), which is not discussed further here.

In addition to the spatial nonhomogeneous nature of wood, the natural scatter of material properties requires statistical theories. An overview of probabilistic analysis of wooden components is given by Kandler et al (2015), whereby random processes have been identified as a possible approach. The authors of Kandler and Füssl (2017) perform a probabilistic study for linear glued laminated timber beams. Hereby, a random field approach describes the one-dimensional Young's modulus as a random variable with spatial correlation.

The proposed approach follows Kandler and Füssl (2017) by analysing a three-dimensional structure with non-homogeneous material properties modelled by a random process. In contrast to the simplification of material properties in one dimension, a three-dimensional representation allows the extension to analysis of more complex geometries and non-linear behaviour. We focus on boards without knots to maintain a general workflow also applicable to other fibre-composites. The variation in stiffness profiles is modelled by the fibre deviation of lamellas obtained from laser scanners as published in Rais et al (2021). The distribution of the fibre deviation is idealised as a stationary Gaussian process. Unlike Kandler and Füssl (2017), we fit an analytical correlation function to the data, instead of directly using the data set to construct the covariance matrix for the random field. This random field approach does not consider fuzzy approaches (Leichsenring et al, 2018; Schietzold et al, 2018, 2019) or non-Gaussian distributions (García and Rosales, 2017). To perform a probabilistic analysis, a common MC scheme similar to Kandler and Füssl (2017) is utilised to approximate the distribution of an output quantity. To enable such a cost-intensive multi-query analysis, we propose to create a data-driven, intrusive reduced-order model.

In the following we concentrate on the natural scatter of material properties of boards with little or no knots. An orthotropic material model dependent on the fibre deviation (Seeber et al, 2023) is assumed and any other influences, such as temperature or moisture, are neglected. As wood is a brittle material under tensile loading, the elastic region is followed by a damage model in many virtual experiments as analysed in Sandhaas and Van De Kuilen (2013).

As an exemplary material, European beech (*Fagus sylvatica*) is chosen for this work, with the authors being able to access an experimental study published by Rais et al (2021). Figure

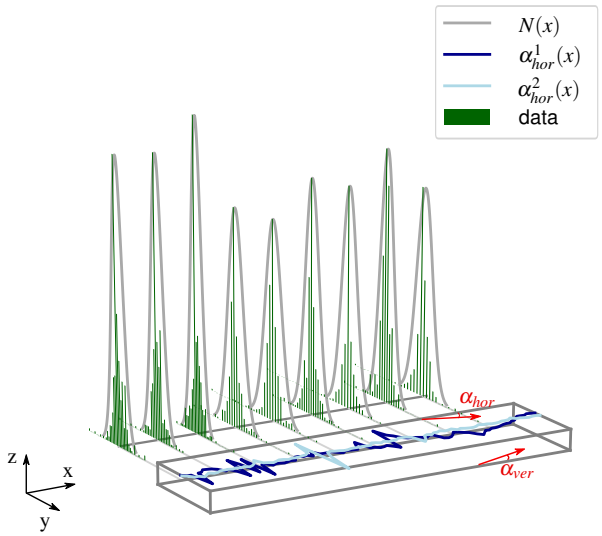

Figure 6.3 Exemplary visualisation of random fields from beech boards Rais et al (2021): the distribution of nine data points in green and its fitted normal distribution $N(x)$ in grey; the one-dimensional functions $\alpha^1_{hor}(x)$ and $\alpha^2_{hor}(x)$ of two boards with $y = z = 0$.

6.2 shows an example of a beech board where the changing fibre direction is visible along four sides of the board. Within the previous work, the surface fibre angles of 407 boards were measured by means of laser sensor scanners (Rais et al, 2021). Thus, a circular laser is projected onto the surface's boards, which deflects to an elliptic shape depending on the fibre direction. The laser evaluates the horizontal fibre angle α_{hor} on the wide surface and the vertical angle α_{ver} on the narrow face, as depicted in Fig. 6.3. A three-dimensional fibre set is interpolated with the surface data as explained in Rais et al (2021) . However, the data points measured by the scanner are not spaced in a regular manner. Therefore, an interpolation function is needed to transfer the data to a regularly sized three-dimensional point cloud. A k-nearest neighbour algorithm (Friedman et al, 1977) with distance measure is implemented to transform the data points into a predefined regular grid.

Figure 6.3 illustrates the nature of the available data set. In blue the horizontal fibre angles α_{hor} of two samples are extracted at the middle ($y = 65$mm) and at the surface ($z = 0$mm) of the board. The connected data points follow the fibre pattern along the horizontal axis.

With the boards of the sample set, a distribution for the fibre angles can be calculated for any discretised point along the board. In Fig. 6.3 nine exemplary points are selected equidistantly along the board and its statistical distribution is evaluated. The sample data for the specific locations are plotted by the green histograms, which show the distribution of 407 boards. The black horizontal line underneath represents an angle of $\alpha_{hor} = 0$. One can notice, that the sample set has a mean value of α_{hor} close to zero and shows a similar distribution to Gaussian normal variables. In grey, the corresponding PDF of a normal distribution evaluated by mean and standard deviation, with

$$N(x) = \frac{1}{\sigma\sqrt{2\pi}} e^{-\frac{1}{2}(\frac{x-\mu}{\sigma})^2}, \tag{6.4}$$

is depicted.

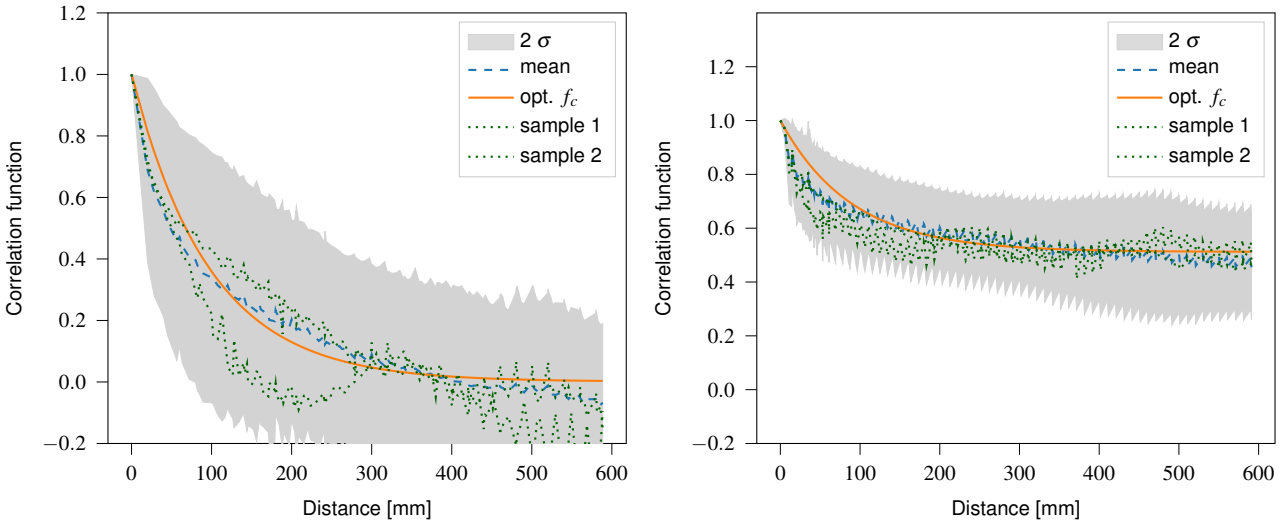

(a) Correlation function ($l_c = 50.4$) for α_{hor}: computed from 30 boards for the horizontal angle in xy-plane.

(b) Correlation function ($l_c = 36.1$) for α_{ver}: computed from 30 boards for the vertical angle in xz-plane.

Figure 6.4 Correlation function fitted to 30 sample data for horizontal α_{hor} and vertical α_{ver} fibre deviation angle in x-y and x-z plane.

In addition to the statistical distribution, the fibre angle field can be characterised by its spatial correlation. The correlation function describes the influence from one point to its neighbours and can be approximated as presented in Section 6.2. To analyse the correlation function, the $x-y$ and $x-z$ surfaces of 30 boards without knots are collected from the data set. The scanned boards are of dimension $2414 \cdot 130 \cdot 38$mm. Figure 6.4 plots the experimental and analytical correlation function following Eq. (6.1) and Eq. (6.2). The y-axis shows the correlation coefficient corresponding to its distance k, on the x-axis. The correlation value starts at one, totally correlated, and decreases with larger relative distances.

The horizontal angles α_{hor} measured on the $x-y$ plane are plotted in Fig. 6.4a. The mean of all samples is depicted in blue, and its 2σ range is plotted in grey to indicate the variation within the sample set. Figure 6.4a also shows two randomly selected samples. To fit the correlation function, Eq. (6.3) is minimised with a BFGS optimiser (Zhu et al, 1997). Therefore, the correlation function is evaluated up to the distance of $k = l/4 = 603$ mm, to ensure interpretability. With the exponential kernel of Eq. (2.12) the optimised correlation length converges to 50.4 for α_{hor}, as plotted in orange. In Figure 6.4b, the vertical angle α_{ver} is evaluated following the same principle. The correlation length of the vertical angle does not converge to zero with increasing distance. In other words, an average angle or bias of $f(k) = 0.14$ can be identified for a board, which is independent of the relative distance. The identified correlation length of 36 in

relation to 130mm board width in vertical direction can be questioned, and thicker specimens are required to confirm this observation.

Considering the presented evaluation of the fibre angle data of beech timber boards the following conclusion can be drawn. The distributions of exemplary sample points visually indicate a normal distribution of the data points. Subsequently, the spatial correlation functions are approximated with an exponential isotropic kernel and are compared graphically. Hereby, one can conclude that the assumptions of a stationary or homogeneous random field with a Gaussian distribution are suitable. This implies that the data follows a normal distribution and its correlation is independent of its absolute coordinates. These are strong assumptions, however, their in-depth discussion is out of the scope of this thesis. It can be added that the approach is extendable to other distributions or non-stationary fields, which are referred to in the outlook.

6.3.2. Reduced order model for tension test

To test the capability of MOR methods to represent analysis with fibre-based inhomogeneous material, a linear elastic transient simulation is first created. A simulation of a beech timber board shall illustrate the application of random fields in the scope of reduced order models.

A board under tension with two holes, as depicted in Fig. 6.6 is clamped on the left side $(x = 0)$. On the right $y-z$ plane the applied surface load increases linearly with time following the function $f(t) = t \cdot 3$ in x-direction and $f(t) = t \cdot 0.003$ in y- and z-direction, until the total time $T = 3s$ is reached. To represent an elastic behaviour, the resulting maximum stress in x-direction of 9MPa is chosen so that 20% of the failure strength is not exceeded. An orthotropic material law is used according to Table 6.1 to represent the wooden elastic material constants (Niemz and Soneregger, 2017) and mass density and strength (Rais et al, 2021). Hereby, the width direction corresponds to the tangential direction and the thickness to the radial direction of a timber board. Shear moduli are further approximated by a combination of E_x, E_y, E_z such as $G_{xy}^{-1} = \frac{1+\nu_{yx}}{E_x} + \frac{1+\nu_{xy}}{E_y}$. The tension test with dimension $590 \cdot 40 \cdot 130$ mm, contains 8170 linear hexahedral elements and $10,593$ nodes. It is important to note that the round holes within the board do not represent knots, as the modelled fibre deviation pattern does not consider any interdependencies between fibre deviation and knots. The random field for the horizontal angle α_{hor}, as fitted in Section 6.3.1 is used to represent the spatial inhomogeneity of the material. In a first setting, the vertical angle is neglected. With the local fibre angles the coordinate system of each element and therewith its material properties are rotated as explained in Seeber et al (2023).

Two varying realisations of the random field for α_{hor} are depicted in Fig. 6.5. For each realisation, the vector $\mathbf{b}$ of Eq. (2.15) yield a different outcome for calculating the fibre field, which serves as input for the structural analysis. Depending on the spatial field of material properties, the resulting stress distribution differs, as shown by the comparison in Fig. 6.5. The fibre

Table 6.1 Material properties for the test cases simulating European beech (Niemz and Soneregger, 2017; Rais et al, 2021), with the following units $E\left[\frac{\mathrm{N}}{\mathrm{mm}^2}\right], f\left[\frac{\mathrm{N}}{\mathrm{mm}^2}\right], \rho\left[\frac{\mathrm{kg}}{\mathrm{m}^3}\right]$.

E_x	E_y	E_z	ν_{xy}	ν_{xz}	ν_{yz}	f	ρ
14000	1160	2280	0.43	0.31	0.49	53	689

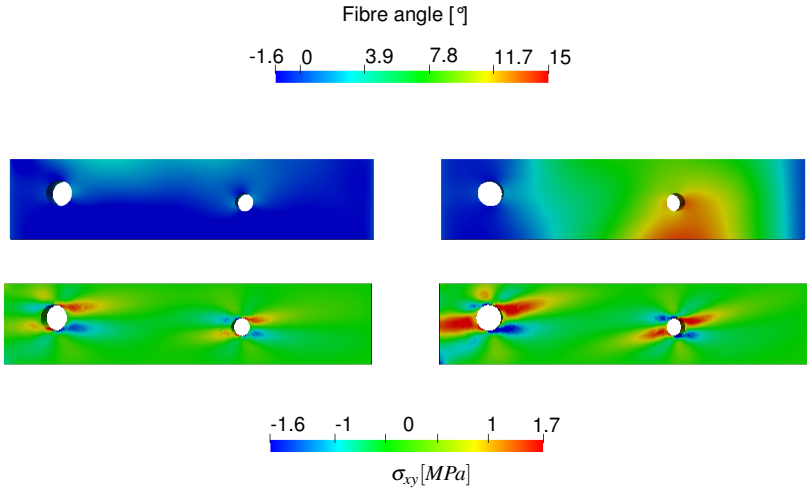

Figure 6.5 Two exemplary fibre deviations modelled by the random field and resulting Cauchy stress σ_{xy} analysed with full-order FE, submitted to a surface force increasing linearly over time up to 9 MPa at $t = 3s$.

angles are indicated based on the colour map on the top and the resulting Cauchy shear stress in the $x-y$ direction σ_{xy} below. The realisation on the left has a large region of the fibre angles close to zero. Consequently, the shear stress zones around the holes are smaller than in the example on the right. The stress distribution in Fig. 6.5 is computed by full order FE models. In Fig. 6.6 the results computed with reduced order models are depicted, corresponding to the left fibre angle field of Fig. 6.5.

The first analysis focus on a linear elastic problem. To create the reduced order model 20 training simulations are conducted and 3 snapshots are collected from each analysis. Notice that for the first training the random field is constructed by an equal weight of all eigenvectors, to ensure that all parts are included in the training simulation. A reduced subspace is constructed with $k = 20$ degrees of freedom. The truncated snapshot by rank 20 has a truncation error following Eq. (3.5) in the range of 10^{-9}. The top of Fig. 6.6 shows the displacement results of the reduced order model with POD based subspace projection (ROM), as explained in Section 3.2.1. The reduced order model with an additional ECM hyper-reduction step (HROM) is depicted above, in addition to the full-order reference solution (wire frame).

Visually, the reduced order models have a very similar deformation pattern. To evaluate the accuracy of the model, Fig. 6.7 shows the error of the HROM model for displacements and Cauchy stresses. Hereby, the relative error for each direction is computed independently, and its magnitude is depicted. The relative error is normalised by the maximum value in each

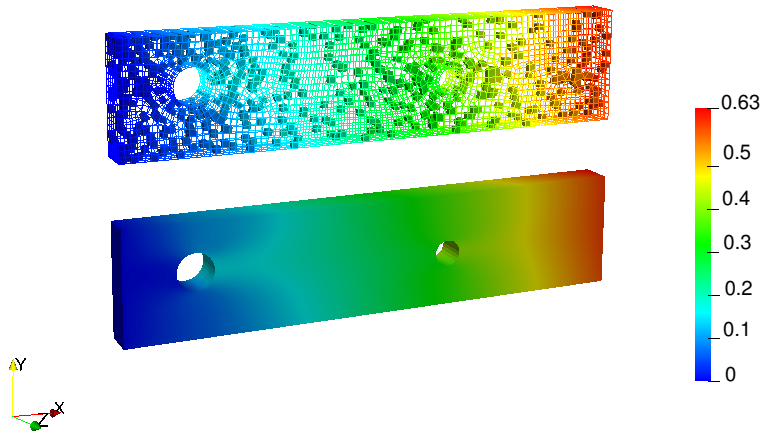

Figure 6.6 Resulting displacements in mm computed by the reduced order model (ROM) on the bottom and hyper-reduced (HROM) model on the top (for a fibre deviation field shown on the left of Fig. 6.5).

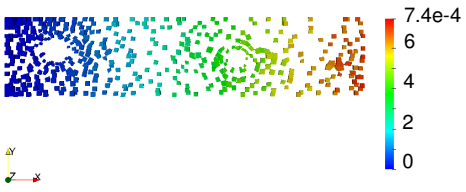

(a) Magnitude of relative displacement error, normalised by the max. displacement for each direction for the example shown in Fig 6.6.

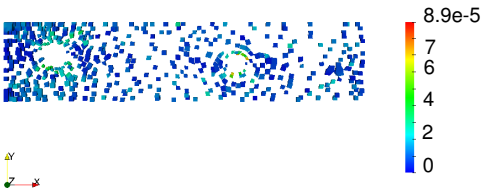

(b) Magnitude of relative stress error for $\sigma_{xx}, \sigma_{xy}, \sigma_{yy}$, normalised by the max. stress for each direction for the example shown in Fig 6.6.

Figure 6.7 Relative displacement and stress error for each element of the HROM shown in Fig 6.6.

direction for better comparison. In displacement, the element with the largest error is also the one with the largest deformation. To ensure that reliable maximum stresses can be evaluated with reduced models, the error of Cauchy stresses is also depicted in Fig. 6.7b. The relative error lies within a low range, and regions with high stresses are also well preserved.

To further evaluate its accuracy, 10 online simulations with varying fibre fields are performed, and a global displacement error e_{GMRE} is computed by

$$e_{GMRE} = \frac{\sqrt{(\mathbf{u} - \mathbf{V}\mathbf{u}_r)^T (\mathbf{u} - \mathbf{V}\mathbf{u}_r)}}{\sqrt{\mathbf{u}^T \mathbf{u}}}, \tag{6.5}$$

with $\mathbf{u}$ and $\mathbf{u}_r$, being the full displacement vector for the last time step $t = T$.

Table 6.2 states the mean displacement error e_{GMRE} for ROM and HROM models as $5.3 \cdot 10^{-7}$ and $2.0 \cdot 10^{-5}$, respectively. With this low error, efficiency can be significantly increased since

Table 6.2 Averaged processing time, speedup and displacement error e_{GMRE} of the constructed reduced models for 10 unseen random field realisations.

	Processing time [s]	Speedup	e_{GMRE}
FOM	13.2		
ROM	0.25	53	$5.3 \cdot 10^{-7}$
HROM	0.03	484	$2.0 \cdot 10^{-5}$

the relative speedups of ROM and HROM are 53 and 484. For completeness, Table 6.2 also compares the mean absolute processing time measured with an Intel processor 'Xeon(R) W-2155 3.30 GHz' containing 10 CPUs. It is important to note that only the construction of the system and the solving step are measured to better compare the analyses.

In Table 6.2 the online costs of the reduced order model are compared to those of a full-order analysis in the online stage. Nevertheless, for a fair evaluation the construction phase of the reduced order model should be considered as well. Computing the SVD, the hyper-reduced elements as well as the random field is insignificant compared to the costs of full-order analysis. Consequently, training simulations, in this case 30 FE analyses, are the decisive factor for the cost of the training phase. The overall efficiency is increased when the multi-query analysis requires more than 33 simulation runs using the HROM model, and it is further improved with a higher number of online analyses.

To increase the complexity and further test the MOR approach the presented test case is extended. A second reduced order model is created with an identical setup, but a second random field for the vertical angle α_{ver} is added. The angle α_{ver} adds a rotation in the $x-z$ plane to the vertical angle α_{hor} in the $y-z$ plan of the system. Similarly to α_{hor}, α_{ver} is represented by an independent random field with an exponential kernel and a fitted correlation length of 36.1. All other parameter settings of the study and the training phase for the reduced models remain unchanged. As before, the displacement error following Eq. (6.5) can be computed to evaluate the accuracy of the model. In the x-direction, ε_{GMRE} is $5.5 \cdot 10^{-3}$ and $5.6 \cdot 10^{-3}$ for ROM and HROM models, respectively. In the y- and z-directions, the error increases to approximately $4.0 \cdot 10^{-2}$ and $5.5 \cdot 10^{-2}$ for both models.

To explain this error discrepancy compared to the previous experiment, Fig. 6.8 compares the singular values of the example studies. The solid line plots the decaying singular vales of the snapshot matrix computed. The reduced subspace of analysis with two random fields has a lower rate of decaying singular values. Once, a truncation of rank 10 and, on the other hand, a truncation of rank 32 represent 99.99 % of the singular values. This results in a larger number of basis vectors to represent the system. However, for a low rate of decaying singular values, the Kolmogorov barrier applies and a linear projection method struggles to find a suitable subspace for the nonlinear manifolds.

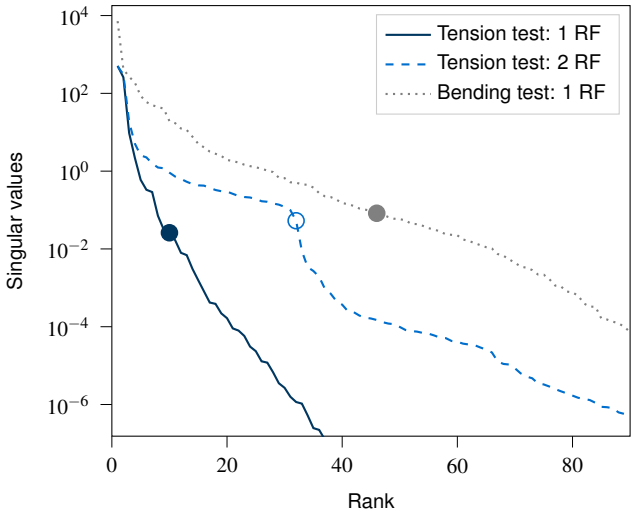

Figure 6.8 Decaying singular values of snapshots matrix and its truncation rank for 99.99% marked with dots for tension test case with one (k=10) or two random fields (k=32) and for the bending test with damage behaviour (k=46).

With the extensive evaluation of the reduced order models for spatial varying material properties we conclude that the simplified models are able to increase efficiency while maintaining a sufficient accuracy. Stresses and displacements can be accurately represented; however, the overall accuracy level also depends on the Kolmogorov n-width, the decaying rate of the singular values. In the next section, we present a second example study and focus on the application of ROMs within the probabilistic workflow.

6.3.3. Probabilistic analysis of bending test with damage

The performance of the reduced order model was evaluated in the last section, whereby its application to the MC analysis is illustrated with the following example. To demonstrate the proposed approach, a wooden board under bending is tested. Figure 6.9 draws the setup of the analysis, which is inspired by the common experimental four-point bending test. To model the forces in y-direction, a surface load is applied. The material properties are identical to those given in Table 6.1, only $\nu_{yz} = 0$ and $\nu_{xz} = 0$ are set to zero, as the behaviour in the vertical direction is decisive for the bending phenomena. To model the heterogeneous material properties, the horizontal angle is described as a random field identical to that presented in the previous sections. In addition, a damage criterion is evaluated based on an equivalent stress function as shown in Oller et al (1996). Thus, stresses are checked against the isotropic strength value of 53 MPa and its stiffness is reduced to account for the damage. The damage law is chosen for simplicity and the reader is referred to Sandhaas and Van De Kuilen (2013) for wood-specific damage criteria.

The dimensions of the board are 2700 mm, 130 mm, 40 mm in x-, y-, z-direction. It is symmetrically set up with a distance between the two supports of 2470mm and between the load application points of 900mm. The beam is meshed with three-dimensional tetrahedrons con-

taining four nodes, considering small displacements. The force increases linearly over time, and the analysis is stopped if an accumulated damage coefficient reaches a certain limit and further evaluations are unreasonable. The simulation is terminated if 90 elements have been damaged or if the time is evaluated to $t = 6s$. In this way, the maximum load capacity of the wooden beam can be investigated. With varying realisations of the random field, the damaged elements often occur in the vicinity of the supports changing from the right to the left one. The damage area of boards without knots is expected to be at the bottom of the board, failing under tension. However, here a simplified damage criterion based on an equivalent stress results in different damage areas, which are further referred to in the outlook.

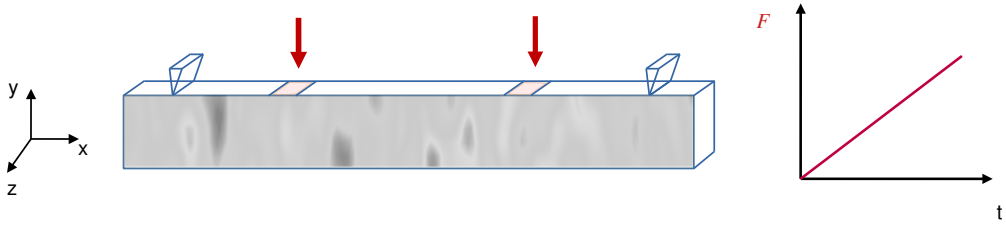

Figure 6.9 Four-point bending test with inhomogeneous material properties and linearly increasing load over time.

Of great importance for the quality of a reduced order model is the training setup. Here, we exploit 50 training simulations to create the reduced subspace. Each training simulation is an analysis with spatially varying fibre angles, a realisation of the constructed random field. Figure 6.10 shows one realisation of the horizontal angle $l_c = 50.1$, as fitted in Fig. 6.4. From each training simulation, 5 equally distanced snapshots are collected during the time interval $T = 6s$, where the incremental time step is 0.01. The load increases linearly following the equation $f(t) = t \cdot 0.35$, so that the final load of 2.1MPa is applied in the last step. After performing a POD, the snapshot matrix is truncated by rank 70. Moreover, a hyper-reduction is performed, resulting in the selection of 3017 out of 11993 elements.

To evaluate the proposed approach, we focus on the probabilistic analysis exploiting the ROM, and HROM model. An identical analysis with the full-order model is performed for comparison. In total, 500 simulations are conducted with varying realisations of the random field. Figure 6.11 depicts the histograms of the study with full-order model, ROM and HROM. In Fig. 6.11 the x-axis represents the maximum load normalised by $p_c = 2.1$ MPa, and the y-axis shows its number of occurrences within the MC analysis. For most of the analysis, the maximum time step $T = 6s$ was reached and those determined by the damage criterion appear to follow the increasing phase of a normal distribution. One can notice that a comparable distribution of the maximum load is observable with the reduced models in comparison to the reference. The mean value of the maximum simulation time of the full-order model is 4.412s, compared to 4.399s for ROM and 4.396s for HROM. Hence, the maximum load can be calculated by $f(t) = t \cdot 0.35$. Through the nonlinear material law the speedups only applying the Galerkin projection are reduced, and the necessity of the additional hyper-reduction step becomes apparent. In

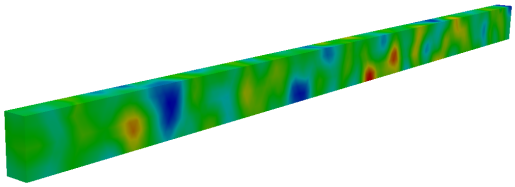

Figure 6.10 Qualitative visualisation of three dimensional realisation of horizontal angle with fitted correlation lengths l_c = 50.4 following Section 6.3.1. Negative angles are displayed in blue, an angle of zero in green and positive angles are marked in red.

contrast to the previous example, the processing times include the overall simulation time with system pre- and post-processing. It is important to note that these evaluations are specific to *Kratos Multiphysics* and also depend on the specific version of the code. To get an overall impression of its practical use, Table 6.3 shows the measured processing times for analysis with the *Kratos* MOR application from March 2020. The cost of a ROM model is reduced by a factor of 1.2, whereby the HROM achieves speedups by a factor of 9, while maintaining a high level of accuracy. Whereby the speedups of the other examples are the specific accelerations due to the projection-based approaches, this shall give an insight to the practical use.

Table 6.3 Online processing time and speedup factors for 500 MC simulations using FOM, ROM, and HROM models.

	Processing [s]	Speedup
FOM	79.4 x 500 = 39700	
ROM	65.4 x 500 = 32700	1.2
HROM	8.8 x 500 = 4400	9

Instead of performing a successive error analysis, we evaluate the mean value of other output quantities of the 500 simulations to quantify the accuracy of ROM and HROM. Hereby, the MC-approximation error is included in addition to the model error, which represents, however, a realistic setting when using the approach. Two example nodes are selected and their average displacement is compared to the full-order model. For the mid-node at the bottom of the board, a mean y-displacement is computed of 11.151mm via full-order model and 11.663mm (ROM) and 11.739mm (HROM) resulting in a relative error of $4.5 \cdot 10^{-2}$ and $5.2 \cdot 10^{-2}$. On the bottom side of the right load application point, the relative displacement error is extracted to $4.0 \cdot 10^{-2}$ and $4.6 \cdot 10^{-2}$ for ROM and HROM, respectively.

Compared to the previous study, the displacement errors are of magnitude 10^2 higher. The

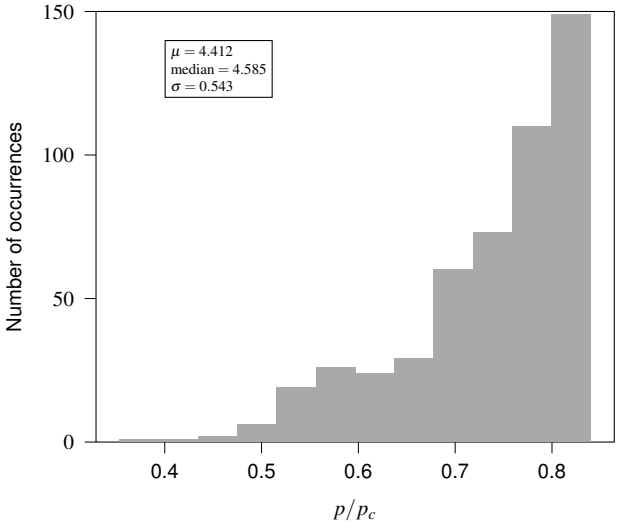

(a) MC analysis: 500 full-order simulations.

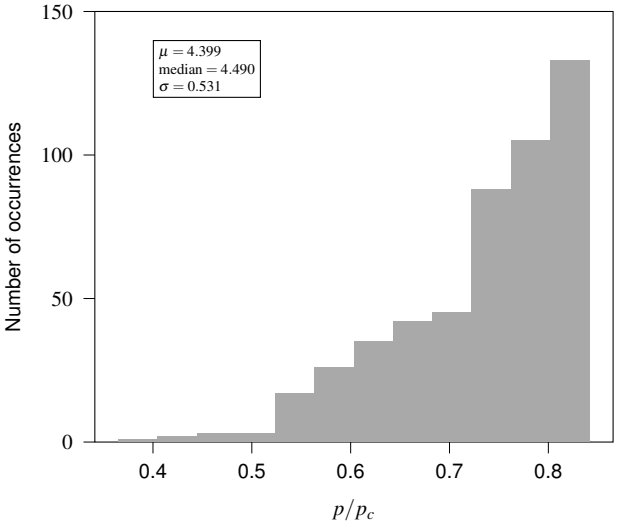

(b) MC analysis: 500 ROMs.

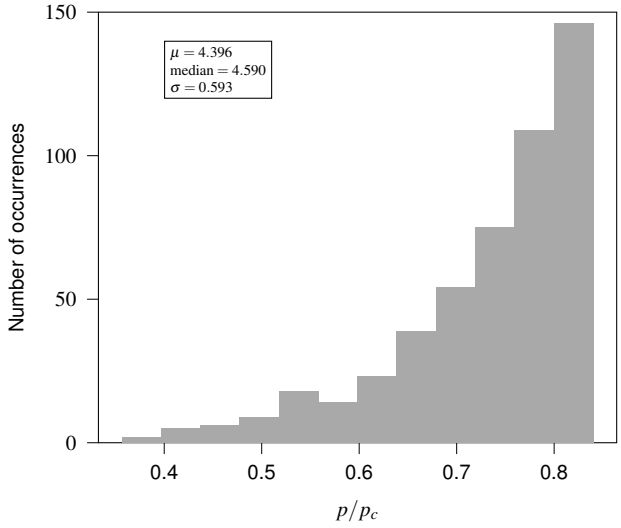

(c) MC analysis: 500 HROMs.

Figure 6.11 Distribution of max. normalised load for 500 transient bending tests, computed by full-order model, ROM and HROM.

displacement error of the study in Section 6.3.2 is in the range of 10^{-4}, whereas in the second example the error reaches $5 \cdot 10^{-2}$. This can also be explained by a lower decay of the singular values as shown in Fig. 6.8, which was already discussed for the tension test case.

6.3.4. Concluding remarks

With this chapter, projection-based reduced order models are applied for uncertain quantification of beech wood as a fibre-composites. The spatial variability of the natural-based material is described by random fields. To analyse these time-consuming models with inhomogeneous material, a reduced model is created. Therefore, we propose to build reduced order models based on training simulations with spatially varying material resulting from realisations of the random field. An experimental data set is exploited for the construction of a material field. With a linear and nonlinear example test case, the efficiency of the surrogate models is evaluated.

We can conclude that, for the linear test case, the reduced model is highly efficient while maintaining accuracy. In comparison, the level of accuracy of the test case with material nonlinearity is reduced. Then, a comparable level of around 5%, similar to what was obtained in the optimisation study in Chapter 5, is achieved.

With the probabilistic analysis, we could show that the proposed workflow enables efficient MC simulations. Compared to classical surrogate models, this technique creates a comprehensive model for varying simulation parameters. The main benefits arise from its general applicability to FE analysis. Therefore, the method is easily extendable to varying nonlinear material laws or geometric nonlinearity.

The quality of the reduced model strongly depends on the representation ability of the constructed subspace. With the random field representation, we could create a reduced order model in a realistic range of the present inhomogeneity for beech wood. Short correlation lengths can result in locally dominated deformation patterns, which are less suitable for the global approach. We conclude that the fibre-induced variation in the longitudinal direction can be represented with the MOR approach. If local phenomena are decisive for the behaviour of the system, the global approach might not be suitable. Then, the MOR approach could be extended by locally defined subspaces.

In the next step, a more realistic wooden structure should be investigated. A complex damage criterion can be applied to realistically assess the behaviour under damage. In addition, the idealisation of the stationary Gaussian field is a preliminary assumption which should be exchanged with an inverse parameter identification. Moreover, environmental influences such as those presented in Yu et al (2022) are an interesting use case for the scheme presented.

Chapter 7

Multi-fidelity robustness analysis via control variate estimators

Through the first two application chapters the reader was familiarised with the intrusive and non-intrusive MOR scheme for varying structural nonlinear multi-query analysis. The following chapter focuses on the proposed multi-fidelity scheme, as the second research aim of this thesis. The approach is based on intrusive and non-intrusive MOR forming a multi-fidelity analysis as introduced in Chapter 4. We focus on uncertainty propagation and efficient robustness analysis of a performance quantity. In the presented test study, this performance parameter is the resultant of a nonlinear FE analysis. The application of the proposed method to the double-loop algorithm exploiting the concept of control variate estimators is illustrated. Moreover, an adaptive construction of the snapshot-based non-intrusive model is tested. Thus, the chapter showcases the proposed multi-fidelity approach for uncertainty propagation.

In the following, the proposed multi-fidelity approach is evaluated for a structural analysis under uncertainty, in particular, for a three-dimensional beam-like structure. For the example study, the loading direction is uncertain and is modelled with independent normal random variables. As a performance quantity, we are interested in the distribution of the tip displacement. The results of the multi-fidelity approach with varying sample numbers and model configuration are explained in detail. We investigate the adaptive construction of the non-intrusive model and the overall impact of the retraining step. Compared to classical MC simulations based on full-order models, we can show that the proposed scheme significantly improves efficiency.

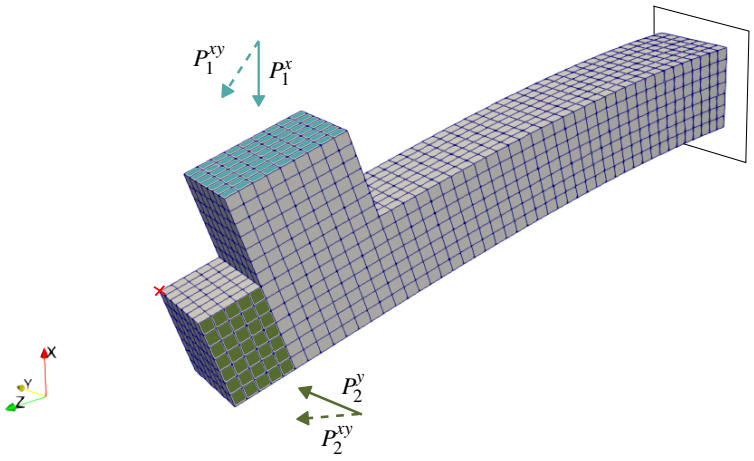

Figure 7.1 Three-dimensional structural design problem with uncertain loading direction of P_1 and P_2 in the $x-y$ plane.

The intrusive MOR model is based on the *Kratos Multiphysics* MOR application (Mataix Ferrándiz et al, 2020; Dadvand et al, 2013, 2010), whereas the non-intrusive model is developed in a stand-alone Python code. We incorporated the FE simulation within an object-orientated Python implementation to the multi-fidelity workflow. Moreover, the control variate was implemented by the author, following the publication of Fina et al (2022); González et al (2019), in consultation with Marcos Valdebenito from the Technical University of Dortmund.

7.1. Beam-like structure with uncertain boundary conditions

To test the multi-fidelity scheme, a three-dimensional structural design problem as depicted in Fig. 7.1 is analysed with a quasi-static FE simulation. The structure is constructed by a clamped beam with a profile of 10 mm $\cdot\, 10$ mm and a length of 70 mm in z-direction. An additional block is added at the top with a distance of $z = 49$ mm from the clamped edge and dimensions 10 mm $\cdot 10$ mm $\cdot 14$ mm. Furthermore, a linear elastic material law with density ρ = 7850 kg/m^3, Young's modulus $E = 206.9$ GPa, and Poisson ratio ν = 0.29 is chosen. The geometry is meshed with 2744 hexahedral elements using a total Lagrangian formulation to enable the computation of large deformations. The meshed geometry leads to $10,905$ degrees of freedom. Two surface loads are applied on the blue and green marked areas with $P_1 = 2 \cdot 10^8 N/m^2$ and $P_2 = 5 \cdot 10^7 N/m^2$, respectively. Moreover, the direction of the surface loads is modelled with a normal random variable with a mean $\mu = 26.5^\circ$ and a variance of $\sigma = 11.3$ in $[^\circ 2]$, so that the load is not only applied in a single direction, but in the $x-y$

plane.

With a MC simulation, the distribution of the tip displacement, as marked in Fig. 7.1, is analysed. Therefore, 1000 reference simulations are conducted and the resulting distribution of the tip displacement in x- and y-direction is depicted in the histograms of Fig. 7.2. With these histograms, the distribution of the performance quantity can be approximated. Due to the different load magnitudes, the variance of the y-displacement distribution with $\sigma = 2.08$ is higher compared to $\sigma = 1.12$ corresponding to the deformation in x-direction.

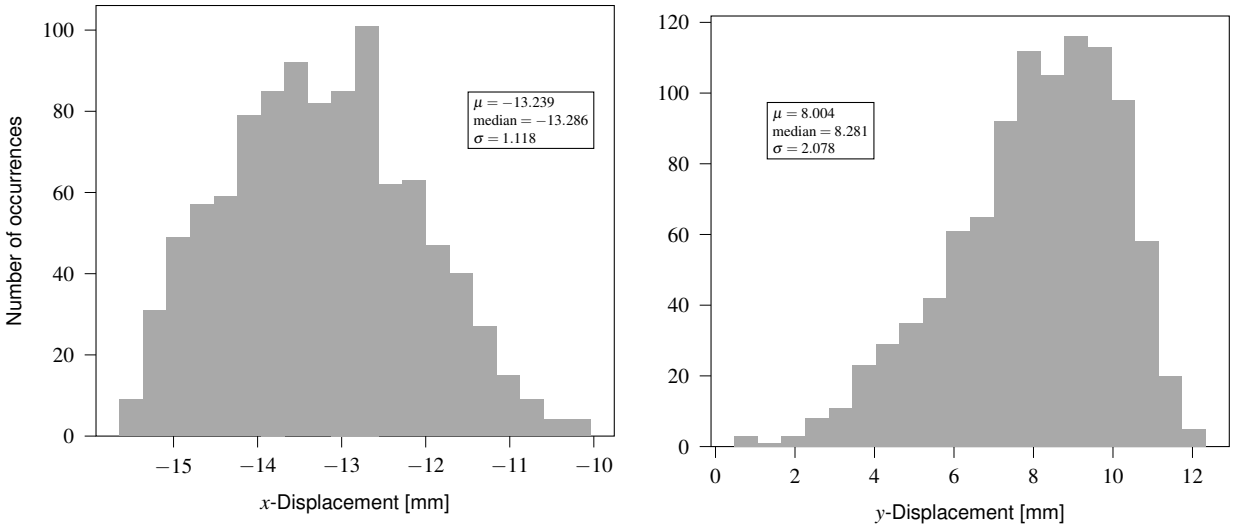

(a) Reference distribution: x-displacement of tip node.

(b) Reference distribution: y-displacement of tip node.

Figure 7.2 MC analysis performed with 1000 full-order simulations evaluated for the tip displacement (see marked node in Fig. 7.1) in x- and y-direction.

7.2. Reduced order models

Next, the reduced order models are constructed to enable the proposed multi-fidelity analysis. In the training phase 25 full-order simulations are evaluated through a full factorial design of experiments with an equidistant grid for load angles between $0°$ and $45°$. Through a global POD of the snapshot matrix, a reduced basis with $k = 16$ vectors is identified for the projection-based approach. The intrusive MOR scheme is further established with ECM as a hyper-reduction method, resulting in 135 hyper-reduced elements (5% of the original element set), such that intrusive ROM and HROM are available. To construct the non-intrusive model, a polynomial regression function of $p = 3$ is chosen.

The quality of the constructed reduced order models is evaluated with Table 7.1 comparing the global e_{GMRE} following Eq. (6.5) and the corresponding processing costs. The processing time merely includes the solving step and neglects the simulation initialisation and post-processing to provide a fair comparison. The average global e_{GMRE} and computing time of ten simulations

are evaluated with realisations of the random variables P_1 and P_2. For comparison, the result of full-order models FOM is displayed in the first column of Table 7.1. The ROM and HROM correspond to the intrusive models with and without hyper-reduction. The properties of the non-intrusive model are displayed in the last column indicated by NiROM. One notices the highly accurate intrusive models, however, with lower computational speedups compared to the non-intrusive approach. A high-fidelity model with high accuracy level and a low-fidelity model with low computational cost are now available for the multi-fidelity scheme.

Table 7.1 Comparison of e_{GMRE} for the varying reduced order models and its corresponding computational cost (system construction and solving).

	FOM	ROM	HROM	NiROM
e_{GMRE} [%]		$5.85 \cdot 10^{-5}$	$2.30 \cdot 10^{-4}$	$5.78 \cdot 10^{-2}$
Processing time [s]	4.33	0.46	0.03	0.0005
Speedup		9.4	144	8660

7.3. Multi-fidelity analysis via control variate estimators

Based on the reduced order models, in the following paragraphs the multi-fidelity approach employing control variate estimators is investigated. With varying models and sample numbers, the properties of the scheme, as proposed with Algorithm 2, are evaluated for the example study. Hence, the section discusses the impact of the additional non-intrusive low-fidelity model on the accuracy, computational cost, and implementation complexity.

To showcase the multi-fidelity algorithm, Tables 7.2 and 7.3 present the results of the applied analysis schemes, in terms of x and y deformation as the desired output quantity. To compare the approach with a reference solution, we state the results obtained with 2000 full-order simulations in the first row. Models referring to MC employ a single-fidelity analysis based solely on MC estimators following Eq. (2.16) and (2.17) to approximate the mean and variance of the output quantity. Furthermore, the variance of the estimators can be approximated with Eq. (2.18) and (2.19) to indicate its precision.

For the control variate estimators, the number of samples from the high-fidelity model n is set to 60, with the number of low-fidelity models given by m. The parameter n_{eq} represents the equivalent full-order simulation cost, to conveniently compare the different analyses. It is calculated by

$$n_{eq} = n_{train} + \frac{n}{s_{HF}} + \frac{n+m}{s_{LF}}, \tag{7.1}$$

additionally considering the number of training simulations n_{train}. The variables s_{HF} and s_{LF} are the speedup factors for the high- and low-fidelity model, which can be acquired from Table 7.1. The estimation of mean and variance based on control variate (CV) approaches are calculated with Eq. (2.21) - (2.29), using varying levels of reduced order models. We first focus on the

result of the proposed algorithm and discuss the different model options 3 - 5, in the following paragraphs to highlight specific attributes of the scheme.

The control variate estimators computed by Algorithm 2 are shown in the second row of Table 7.2, where $n = 60$ and $m = 1200$ samples are employed for high- and low-fidelity analyses loops. For the high-fidelity model, a HROM is utilised, and the adaptively updated NiROM represents the low-fidelity model. The estimation of the first- and second-order statistics, $\hat{\mu}_1$ and $\hat{\mu}_2$ can be successfully approximated, since the approximated mean and variance highly correlate to the reference solution, as stated in Tables 7.2 and 7.3.

Table 7.2 Estimation of second-order statistics for tip displacement in x-direction: comparison of Monte Carlo (MC) and control variate (CV) estimators employing multi-fidelity MOR schemes.

Analysis type	High-fidelity	Low-fidelity	n	m	n_{eq}	$\hat{\mu}_1$ [mm]	$V[\hat{\mu}_1]$ [mm^2]	$\hat{\mu}_2$ [mm^2]	$V[\hat{\mu}_2]$ [mm^4]
Reference									
1. MC	FOM	-	2000	-	2000	-13.1921	0.000634	1.2680	0.001283
Algorithm 2									
2. CV	HROM	NiROM	60	1200	25.56	-13.2006	0.000957	1.2482	0.002596
Other analysis and model configuration: here NiROM without retraining									
3. MC	HROM	-	60	-	25.42	-13.4648	0.018247	1.0947	0.036514
4. CV	HROM	NiROM	60	600	25.49	-13.2247	0.001817	1.1795	0.004306
5. CV	HROM	NiROM	60	1200	25.56	-13.2092	0.001028	1.2919	0.002729

To highlight the influence of the additional low-fidelity model within the control variate estimators, the multi-fidelity analysis is repeated 500 times. For each out of 500 runs, a multi-query analysis with 60 high-fidelity analyses, and additional 1200 low-fidelity analyses are performed, and the resulting mean and variance values are stored. Hence, a histogram of the approximated mean $\hat{\mu}_1$ and variance $\hat{\mu}_2$ is plotted in Fig. 7.3. In comparison, the single-fidelity analysis is displayed, labelled as MC estimator. Therefore, the high-fidelity model based on HROM is evaluated with $n = 60$ samples following the setup of analysis three in Table 7.2. The histograms of Fig. 7.3 visually display the strongly reduced variance of the control variate estimators, compared to the MC estimators. Thus, by adding the low-fidelity model to the estimators, the approximation accuracy can be strongly improved. Figures 7.3a and 7.3b show the tip displacement in the x-direction, while Figs. 7.3c and 7.3d display the estimators for the y-displacement. As expected, second-order estimators show a higher variance of estimators $V[\hat{\mu}_2]$ compared to mean estimators $V[\hat{\mu}_1]$. It is noticeable that the variance $\hat{\mu}_2$ of the y-displacement is, in fact, higher than for the displacement in x-direction. With a larger variance of the output quantity, the approximation is more challenging. This can be observed by the higher variances of the estimators $V[\hat{\mu}_2]$. However, this does not affect the approximation ability of the control variate estimators.

To confirm the variances of the estimators $V[\hat{\mu}]$ in Table 7.2, a comparison with the histograms

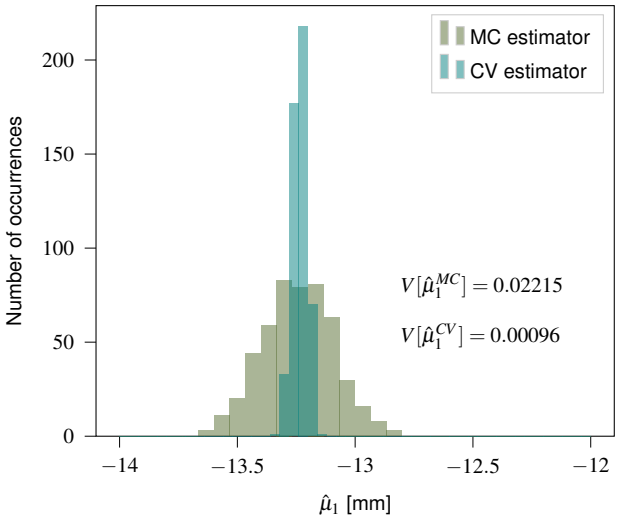

(a) Mean estimator $\hat{\mu}_1$ of tip displacement in x-direction.

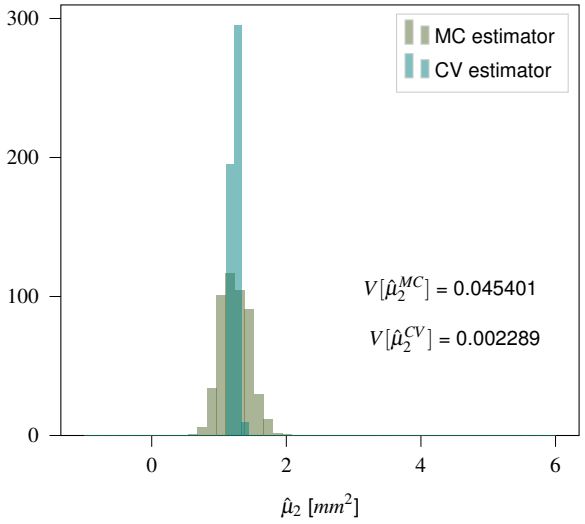

(b) Variance estimator $\hat{\mu}_2$ of tip displacement in x-direction.

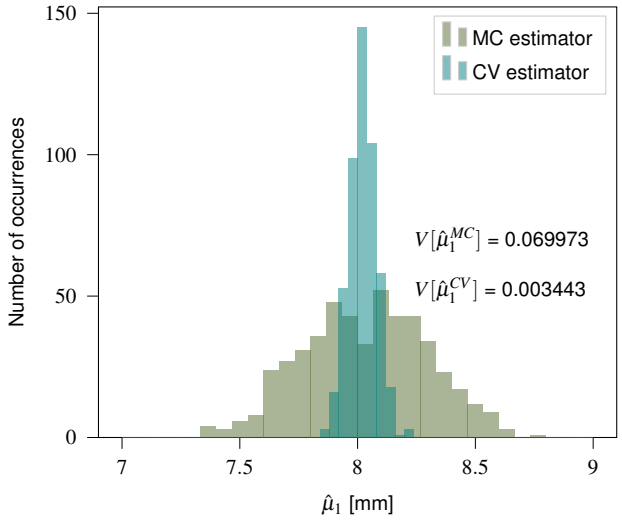

(c) Mean estimator $\hat{\mu}_1$ of tip displacement in y-direction.

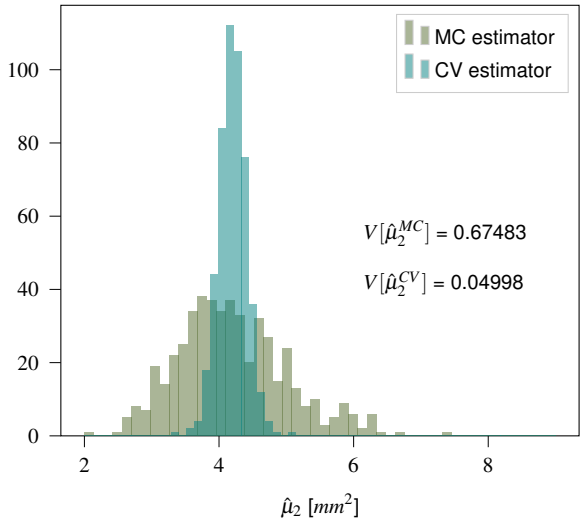

(d) Variance estimator $\hat{\mu}_2$ of tip displacement in y-direction.

Figure 7.3 Histogram of 500 analyses comparing Monte Carlo (MC) and control variate (CV) estimators to estimate the mean $\hat{\mu}_1$ and variance $\hat{\mu}_2$ and its derived variance of estimators V for the tip displacement in the x- and y-direction. The analyses are performed with schemes 3 and 5 of Table 7.2 and Table 7.3, which show the corresponding estimators for a single analysis run.

can be drawn. The variance of estimators, such as Eq. (2.22) is tested against the numerical experiment of 500 individual control variate estimations. When comparing $V[\hat{\mu}_1^{CV}]$ from Table 7.2 with Fig. 7.3a, 0.000957 is confirmed by the value of 0.00096 calculated through the repetitive study.

Returning to Table 7.2, we next analyse the influence of varying numbers of low-fidelity samples within the control variate approach. In Analysis 4, $m = 600$ low-fidelity samples are evaluated, while in Analysis 5, m is set to 1200. It is apparent that the additional computational costs are very small, however, the estimation's accuracy increases. The estimations for $\hat{\mu}_1$ and $\hat{\mu}_2$ are closer to the reference solution for Analysis 5 compared to Analysis 4. Furthermore, the error estimation $V[\hat{\mu}]$ clearly shows the positive effect of higher sample numbers.

After discussing the approximation accuracy of the control variate estimators, the computational costs are evaluated. Since for MC estimators the variance of the mean $V[\mu_1]$ is inversely proportional to the number of samples, one can calculate the number of samples to reach a similar error level as in the multi-fidelity scheme. With the same approximation accuracy, a fair comparison of computational expenses can be made. In fact, a MC simulation with 1325 high-fidelity analyses would be required to reach a level similar to $V[\mu_1] = 0.001$. The multi-fidelity scheme has a resultant n_{eq} of 25.6 to achieve $V[\mu_1] = 0.001$. This results in an overall speedup factor of 51.7. It is important to note that the measured acceleration also includes the construction phase of the reduced order models.

Second, we investigate the effect of the non-intrusive MOR model with a retraining phase, as introduced in Algorithm 2. The NiROM is additionally based on high-fidelity results involved in the control variate estimators and not only the full-order simulations of the training phase. To judge the influence of the retraining step, the multi-fidelity scheme is executed without the adaptive nature of the NiROM. The resulting distribution properties are depicted in Table 7.2 as Analysis 5. Compared to Analysis 2, the estimation of the mean and variance with the adaptive NiROM is slightly closer to the reference solution. A clear improvement in the approximation of $\hat{\mu}_2$ in y-direction with the retraining step is visible in Table 7.3. Here, $V[\hat{\mu}_2]$ can be reduced from 0.0442 to 0.0398 through the enlarged training set of the adaptive NiROM.

Table 7.3 Estimation of second-order statistics for tip displacement in y-direction: comparison of Monte Carlo (MC) and control variate (CV) estimators employing multi-fidelity MOR schemes.

Analysis type	High-fidelity	Low-fidelity	n	m	n_{eq}	μ_1 [mm]	$V[\mu_1]$ [mm^2]	μ_2 [mm^2]	$V[\mu_2]$ [mm^4]
1. MC	FOM	-	2000	-	2000	8.07810	0.002049	4.09844	0.02005
2. CV	HROM	NiROM	60	1200	25.56	8.0579	0.003379	4.1610	0.04423
3. CV	HROM	adaptive NiROM	60	1200	25.56	8.0625	0.003356	4.1046	0.03982

To further investigate the effect of the retraining step, a new set of reduced order models based on 9 training simulations, instead of 25, is created. Figure 7.4 shows the control variate

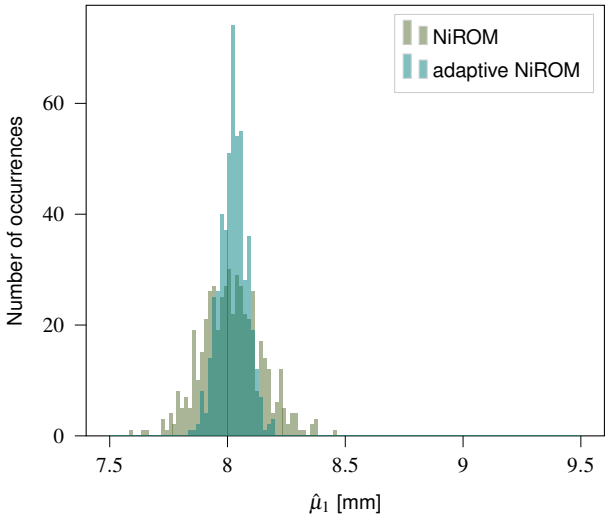

(a) Mean estimator $\hat{\mu}_1$ of tip displacement in y-direction employing NiROM and adaptive NiROM.

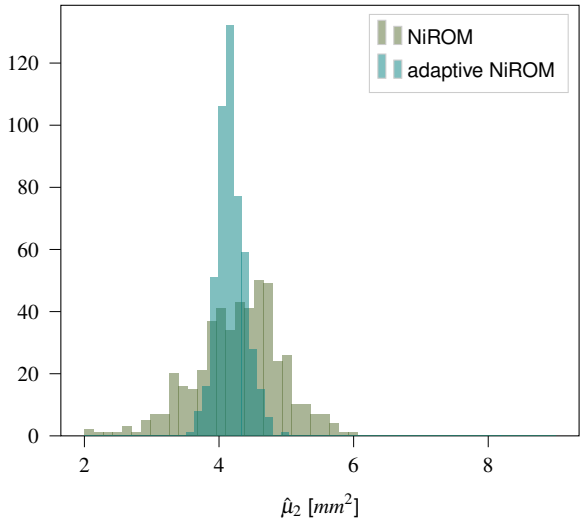

(b) Variance estimator $\hat{\mu}_2$ of tip displacement in y-direction employing NiROM and adaptive NiROM.

Figure 7.4 Histogram of 500 analysis comparing control variate estimators (CV) using a classical NiROM and an adaptive NiROM based on 9 offline training simulations to estimate the mean $\hat{\mu}_1$ and variance $\hat{\mu}_2$ for the tip displacement in y-direction.

estimator without the retraining step in green and with adaptive construction in blue. The histogram clearly visualises that the variance of the estimators is reduced, indicating a lower approximation error. This can be observed for the mean estimator in Fig. 7.4a as well as for the variance estimator in Fig. 7.4b .

The positive impact of the adaptive reconstruction of the non-intrusive model highly depends on its initial quality. If the accuracy of the initial NiROM is relatively high, additional retraining has less impact. Consequently, an adaptive NiROM is especially beneficial for models with a low number of initial training simulations. Moreover, these assumptions are based on the premises that the intrusive models have higher accuracy than the non-intrusive ones.

7.4. Concluding remarks

With the example problem, the multi-fidelity scheme was tested and evaluated in comparison to a reference solution based on full-order simulations. In summary, the test study has shown that the proposed multi-fidelity scheme successfully performs efficient uncertainty propagation. In fact, this analysis shows the most favourable application of the MOR scheme in comparison to other studies presented.

For the robustness analysis, we are interested in the distribution of an output quantity analysed through a FE simulation or, in our case, a reduced order model. Therefore, the parameter space considered for the reduced model is fully exploited for the robustness evaluation. This

is in contrast to the optimisation algorithm, where the main focus lies on the optimum and its direct neighbourhood.

The construction of the intrusive model showed significantly higher speedups compared to the previous chapters. The analysis is based on large deformations, and the variation of the load direction is expected to create a manifold with a lower level of nonlinearity compared to the first two chapters. Therefore, the global POD approach results in ROMs with very low error measures. Here, the hyper-reduction reduces its accuracy level significantly by a factor of 10. The resulting online speedup factor of 144 is also increased by a magnitude compared to the crash example.

However, the speedup comparison to the first chapter on crashworthiness is difficult as varying FE solver have been used. The implementation complexity of large-scale solvers omits a fair comparison. Moreover, the speedup is highly dependent on the exact measured processing times. For example, there is a great disparity in measuring the overall processing time of the simulation, including pre- and post-processing steps or only the solving time of the characteristic equation.

The combination of intrusive and non-intrusive models allows for an approximation of the performance distribution with a speedup of 52 (including offline costs) while maintaining a comparable level of accuracy. Moreover, the beneficial influence of the low-fidelity model has been presented in detail with varying parameter configurations. It could be shown that adding a high number of low-fidelity samples increases the accuracy of the statistical estimators. An additional iterative analysis could confirm the theoretical equations of the control variate estimators and illustrate its variance reduction on the estimators.

To analyse the effect of the retraining stage, the multi-fidelity scheme was evaluated with varying non-intrusive models to highlight its impact. Depending on the initial quality of the non-intrusive model, the impact of the retraining step varies. For models with low approximation abilities due to a limited number of offline training simulations, the adaptive NiROM could significantly improve the overall analysis. If the initial non-intrusive model is already on a high accuracy level, the importance of the retraining step decreases.

Overall, the combination of control variate estimators and multiple levels of reduced-order models seems a promising idea. This is embedded in the research direction of multi-level MC analysis, and further extension with additional fidelity levels could be investigated.

Chapter 8

Multi-fidelity robust design optimisation

In the previous chapter, the multi-fidelity concept was applied to an uncertainty propagation problem. To illustrate its general applicability, this application chapter concentrates on robust optimisation. Therefore, the multi-fidelity approach, as introduced in Section 4, is applied to optimisation problems considering uncertainty. With two structural design problems, the double-loop algorithm using high- and low-fidelity MOR models is demonstrated. Furthermore, we illustrate the efficiency gains resulting from the combination of both models.

The first example seeks the ideal position of a hole for a beam that is experiencing damage. We highlight the differences between absolute and robust minima on the basis of objective function evaluations in the full design space. The result evaluation focuses on the robustness criterion and on the adaptive non-intrusive model. It is shown that the proposed multi-fidelity workflow converges to the robust minimum with reduced computational effort. The second example is a large-scale airfoil wing constructed with fibre composites, in which the fibre orientation is optimised. Here, we illustrate that the proposed approach is also applicable to industrial-scale problems.

As in the previous chapter, the multi-fidelity MOR implementation incorporates the intrusive MOR from *Kratos Multiphysics* with the non-intrusive algorithm. This is combined with the optimisation algorithm that is realised with the help of the Python library SciPy (2022). The first example was published in a conference proceeding by the author (Czech et al, 2022a), which is the basis for the following paragraphs. The second example was developed during a Master's thesis of Weißinger (2023) supervised by the author.

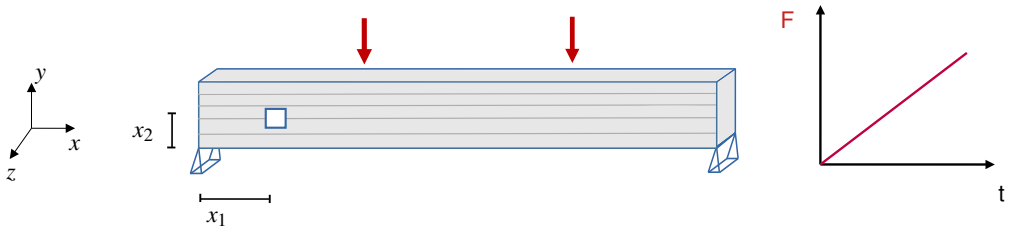

Figure 8.1 Three-dimensional test case: dynamic four-point bending test with hole.

8.1. Positioning of a hole within a bending beam

With this example the multi-fidelity scheme, presented in Algorithm 3 of Chapter 4 is assessed. Hereby, we focus on the evaluation of the robustness criterion and the retraining step of the non-intrusive scheme and leave the efficiency evaluation to the second example case.

8.1.1. Four-point bending test with damage

As depicted in Fig. 8.1, a four-point bending test inspired by a wooden board experiment (Kandler et al, 2018) is analysed to illustrate the proposed algorithm. The three-dimensional beam has a length of 2700mm and a rectangular cross-section of 150mm$\cdot 70$mm. It is meshed with quadratic elements of length 25mm in all directions, resulting in 9156 degrees of freedom. Subjected by a linearly increasing load over time, $F_y = 0.3t$ N/s, which is distributed as a surface load, the beam bends in negative y-direction until 10s are reached. The surface loads are applied at a distance of 800mm to 850mm, measured from the edges of the board. An orthotropic material description with a Tsai-Wu damage criterion (Knight, 2006) characterises the material behaviour. The damage criterion is evaluated at each time step, and, if stresses exceed the strength value, the stiffness of the element is reduced by multiplying with the reduction factor β. Table 8.1 states Young's modulus E, Poisson's ratio ν, strength value f, reduction factors β, and mass density ρ corresponding to the coordinate system shown in Fig. 8.1. If no specific direction is stated, the parameters in Table 8.1 are assumed to be isotropic. Moreover, the shear moduli are calculated by a combination of E_x, E_y, E_z such as $G_{xy}^{-1} = \frac{1+\nu_{yx}}{E_x} + \frac{1+\nu_{xy}}{E_y}$.

Table 8.1 Material parameter of test cases: Young modulus E $\left[\frac{\text{N}}{\text{mm}^2}\right]$, Poisson's ratio ν, strength f $\left[\frac{\text{N}}{\text{mm}^2}\right]$, reduction factors β, mass density ρ $\left[\frac{\text{kg}}{\text{m}^3}\right]$. The indices $1,2,3$ correspond to x, y, z direction, respectively.

E_1	E_2	E_3	ν	f	β	ρ
12500	500	500	0.0	80	0.01	1000

Figure 8.1 depicts a quadratic hole in the board of size $25 \cdot 25\text{mm}^2$, characterised by the coordinates x_1 and x_2 of its centre, which will be optimised. In this exemplary study, the mid-node displacement of the beam is minimised with respect to the position of the hole. Here, the design variables are treated as continuous variables and the displacement in y-direction at

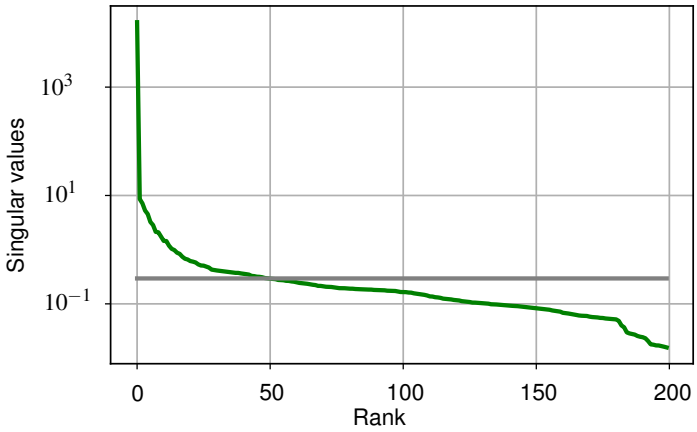

Figure 8.2 Decaying singular values of the snapshot matrix with logarithmic scale, truncated at rank 50 for the reduced order models.

the symmetry plane is considered as the objective function. To better understand and illustrate robust optimisation, a two-dimensional design space is chosen. The complexity is further reduced, as only one half of the symmetric problem is investigated.

8.1.2. Reduced order models

To test the proposed surrogates, full-order training simulations are analysed for the construction of intrusive and non-intrusive reduced order models. In the design space, a full factorial sampling is spanned with 50 points in x- and 4 points in y-direction. At each grid point, a training simulation is conducted, and snapshots are collected from the last time step. These 200 snapshots are combined and reduced to a 50-dimensional subspace via SVD approximation by a truncation error of $2 \cdot 10^{-5}$. The decaying singular values are depicted in Fig. 8.2 on logarithmic scale with a truncation at rank 50. Based on the reduced basis vectors, a regression model is trained for the non-intrusive model. To compute the weights, for the linearly combined bases vectors of Eq. (3.19), a polynomial regression model is introduced with $p = 5$ and trained with 200 snapshot results. As the hyper-reduction step is neglected for this first example, the training phase is completed, and intrusive and non-intrusive reduced order models are available for the desired multi-query analysis.

8.1.3. Robust optimisation of the holes' coordinates

The optimisation study includes two design variables, which describe the coordinates of the hole. All elements in the z-direction with identical x and y coordinates are deleted such that a hole is created. Elements at the boundary and those affected by the support are excluded so that the first design variable, the x-coordinates are chosen between $112.5 \leq x_1 \leq 1612.5$mm and the y-coordinate is bounded with $37.5 \leq x_2 \leq 112.5$mm. The objective is defined as the displacement of the mid-node in y-direction. Moreover, the design variables are defined as the uncertain variables and its impact on the objective function is to be investigated. To consider the robustness criterion, the variance of the objective function is included as a constraint, with $\sigma_{crit} \leq 0.001[\text{mm}^2]$.

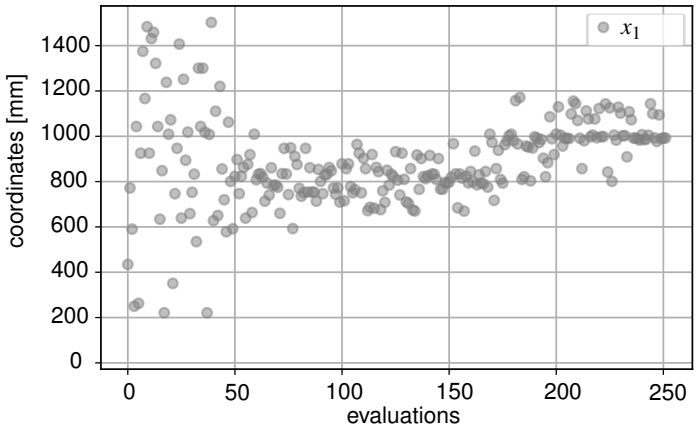

Figure 8.3 Convergence of design variables x_1 to robust minimum x_r computed by FOM analyses with robust design optimisation.

For a reference solution, the optimisation scheme based on full-order analyses is conducted. To perform the optimisation, a differential evolution algorithm is employed with a population of 5 and a recombination factor of 0.7. The algorithm stopped after 14 iterations and 253 evaluations, whereby an absolute convergence tolerance of 0.001 is reached. The global minimum $\mathbf{x_0}$ is found at the coordinates $x_1 = 193.4$mm and $x_2 = 103.4$mm, which correspond to a hole with the central coordinates $x = 187.5$mm and $y = 112.5$mm.

To better judge the results and effectiveness of the variability measurement, the design space is scanned by FOM simulations. In Fig. 8.4a, the x- and y-axes represent the x- and y-coordinates of the hole, and the normalised objective function is displayed according to the colour bar. The global minimum x_0 is located in the upper left part of the design space, coloured dark blue. Another optimisation, including the robustness criterion, is started with the same optimisation parameters. Figure 8.3 depicts the convergence of the design variables x_1. When adding the robustness criterion by the standard deviation approximated by four points, another minimum x_r, is found. The absolute value of the objective function is higher, but the larger distance between iso-lines visualises a reduced variability compared to the global optimum x_0.

For the global minimum, the position of the hole is close to the corner of the board, above the support. Here, the hole weakens the board only minimally, but its variability in bending is relatively high. When the hole is moved closer to the support, the force flow is disturbed and deformation increases. A hole placement with lower variability of the objective function can be found in the middle (shown as x_r in Fig. 8.4), approximately one third of the board length, with a greater distance from the support.

The result of the robust optimisation via MOR models, as proposed in Algorithm 3 is depicted in Fig. 8.4b. Therefore, the variance is estimated with the high-fidelity model and displacement is based on the low-fidelity evaluations. The background shows the design space scanned by

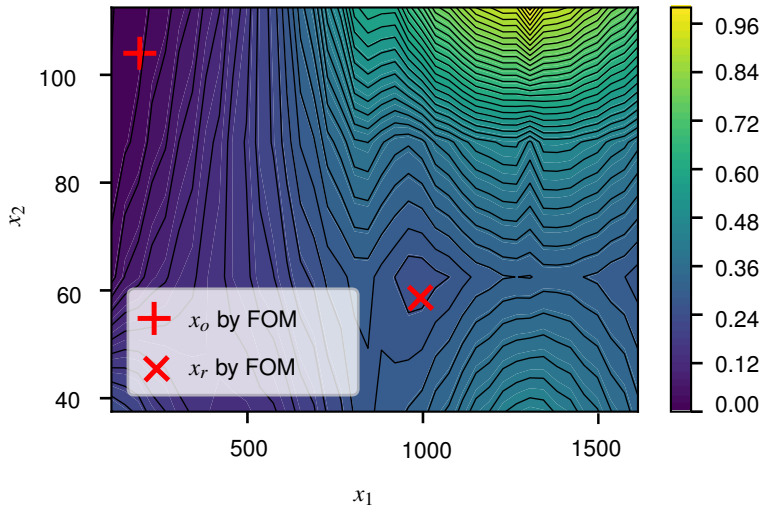

(a) Two-dimensional design space showing global x_0 and robust minimum x_r evaluated with a differential evolution strategy using FOM analyses.

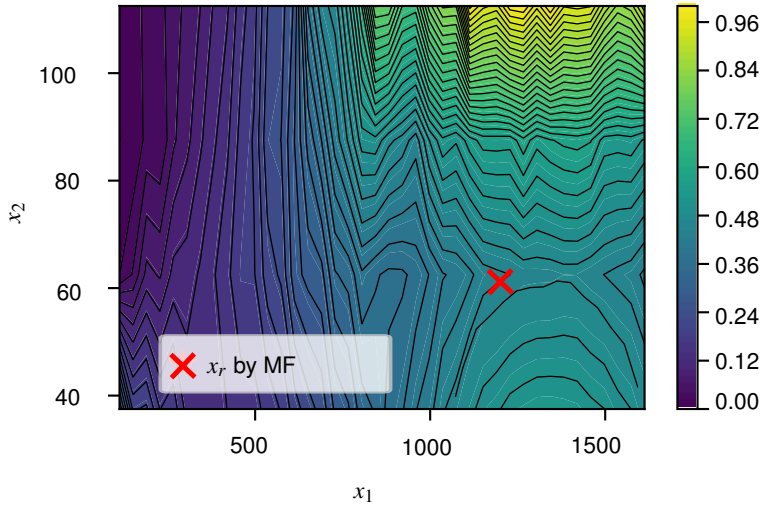

(b) Two-dimensional design space evaluated by ROM analyses and robust minimum found with multi-fidelity (MF) approach.

Figure 8.4 Two-dimensional design space showing the global x_0 and robust x_r minimum of the objective function evaluated with the full-order model (FOM) and the intrusive reduced order model (ROM).

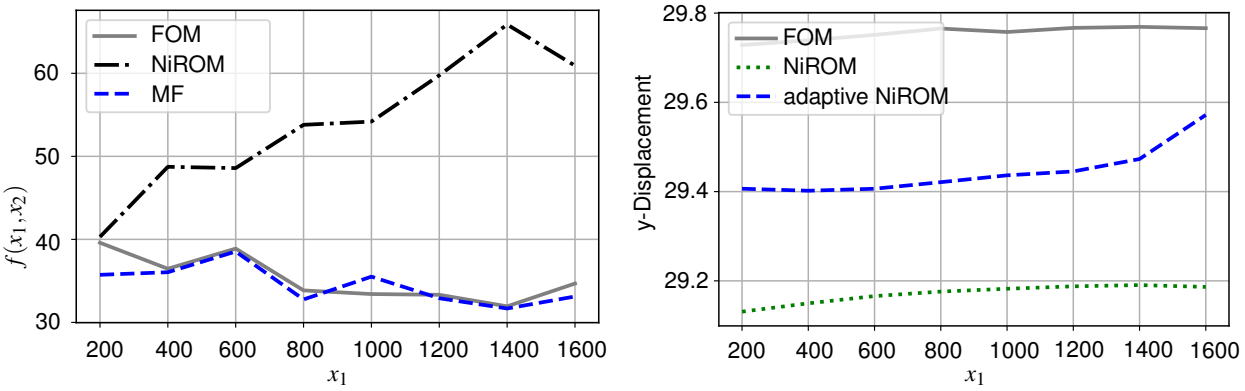

(a) Objective function $f(x_1,x_2)$ computed by low-fidelity (NiROM) and multi-fidelity (Adaptive NiROM + ROM) in comparison to FOM reference solution for varying x_1.

(b) Mid-node displacement in y-direction computed by NiROM with and without adaptive training in comparison to FOM reference solution for varying x_1.

Figure 8.5 Evaluation of the multi-fidelity (MF) optimisation scheme compared to full-order analysis (FOM) and analysis based non-intrusive models (NiROM) distinguishing between NiROM and adaptive NiROMs.

intrusive reduced order analyses. When comparing the design space analysed by the intrusive model in Fig. 8.4b with the reference in Fig. 8.4a, the overall landscape is well approximated. It is noticeable that the resulting design variable x_1 computed by the proposed algorithm slightly deviates from the reference solution due to the approximation error of the ROM. To further analyse this discrepancy, the accuracy of the surrogate models is evaluated with the normalised mean squared error:

$$\varepsilon_{NMSE} = \sqrt{\frac{(u_{FOM} - u)^2}{u_{FOM}^2}}. \tag{8.1}$$

The mid-node y-displacement of the robust optima, as the decisive quantity for the optimisation problem, is compared to the reference solution. The high-fidelity ROM has a normalised mean squared error of $\varepsilon_{NMSE} = 0.009$. In addition, the low-fidelity NiROM is evaluated, resulting in a ε_{NMSE} of 0.02.

To further illustrate the combined models, Fig. 8.5a depicts the objective function $f(x_1,x_2)$ computed by low-fidelity (NiROM) and multi-fidelity (adaptive NiROM + ROM) compared to FOM reference solution for varying x_1. One can clearly notice that the system answer between the NiROM and FOM reference solution diverges, indicating that an optimisation based solely on the low-fidelity model is not sufficient. On the other hand, the multi-fidelity model closely follows the reference solution.

In a next analysis step, we evaluate the retraining step of the NiROM in Fig. 8.5b. To highlight the importance of the retraining step, an optimisation run with (adaptive NiROM) and without update (NiROM) is compared to the reference solution. The adaptive NiROM improves its accuracy and also the ε_{NMSE} of Eq. (8.1) is reduced from 0.02 to 0.01. Without the adaptive nature, the information gained by the high-fidelity model is not used further, and the accuracy of the approximation is reduced.

Table 8.2 Geometric parameters of the Common Research Model (CRM) of NASA (2022) for the utilised airfoil model of a transsonic transport aircraft.

Wing span	Aspect ratio	Root chord	Tip chord
58.76m	9	13.56m	2.73m

The proposed algorithm was successfully tested on a small structural design problem with material nonlinearity. It could be shown that the robustness criterion can approximate the variability of the objective function and lead to a robust optimum instead of the global minimum. Confirming the results of the last chapter on uncertainty propagation, the adaptive NiROM can improve the overall accuracy of the proposed workflow. To create an efficient scheme for higher nonlinear problems, a hyper-reduction step must be added to the workflow. An application to a large-scale industrial example that includes all the available reduction steps is presented in the next section.

8.2. Robust optimisation of an airfoil wing structure

For the second example study, the fibre direction of a semi-span airfoil wing is optimised applying the multi-fidelity scheme. The focus lies on a large-scale optimisation study in which a simplified airfoil model for a transsonic transport aircraft is analysed. Therefore, we use the Common Research Model (CRM) of NASA (2022), which has been employed for numerous analysis, such as the structural optimisation in Dababneh et al (2018); Kilimtzidis et al (2023). The design of an airfoil wing is a complex task that includes computational fluid dynamics and structural analysis (Bak et al, 2014). Here, we merely focus on the structural design of airfoils, which is commonly optimised for the overall weight, the stiffness and strength, or aeroelastic stability, such as flutter. It is important to note that we do not show a realistic design optimisation of an airfoil wing, but a simplified version to illustrate the applicability of the multi-fidelity scheme to related problems. Therefore, we perform an optimisation that minimises the twisting angle under the variation of two material constants characterising the orientation of the fibre composite material.

8.2.1. Wing structure analysis

The original aircraft model by NASA (2022) is simplified to its wing, neglecting the body, pylon, and nacelle. Moreover, the wing is modelled as a hollow structure, while the reinforcement in the interior are not represented. The upper and lower surfaces of the airfoil wing are shown in Fig. 8.6, with the geometric variable summarised in Table 8.2. The upper and lower structure is modelled with a thickness of 100mm. For detailed explanations of the airfoil model, the reader is referred to Vassberg et al (2008).

The wing is clamped on the left side and static loading conditions are assumed. To model

Table 8.3 Orthotropic material assigned to the wing surfaces for a T300/7901 UD layer, (Hu et al, 2021): Young's modulus E $\left[\frac{\text{N}}{\text{mm}^2}\right]$, shear modulus G $\left[\frac{\text{N}}{\text{mm}^2}\right]$, Poisson's ratio ν. The indices $1,2,3$ correspond to x,y,z direction, respectively.

E_1	E_2,E_3	G_{12}, G_{13}	G_{23}	ν_{12}, ν_{13}	ν_{23}
125000	11300	5430	3980	0.3	0.42

the complex aerodynamic loading, pressure measurements are taken from wind tunnel experiments TNA ESWIRP ETW (2014). The pressure distributions correspond to a wind tunnel experiment that mimics a standard transsonic flight operation with a cruise altitude of 10688m, a Mach number of 0.85, and a nominal lift condition of 0.5. The pressure is measured by 227 pressure ports during the experiment. Within the FE model, we averaged the pressure results to 16 different surface loads. In Fig. 8.6 the corresponding surfaces are depicted, whereby the dotted lines show the location of the experimentally obtained pressure data. The orange surface is highlighted as an example, for which the pressure is averaged to 53 kPa considering the corresponding pressure ports of the first three rows.

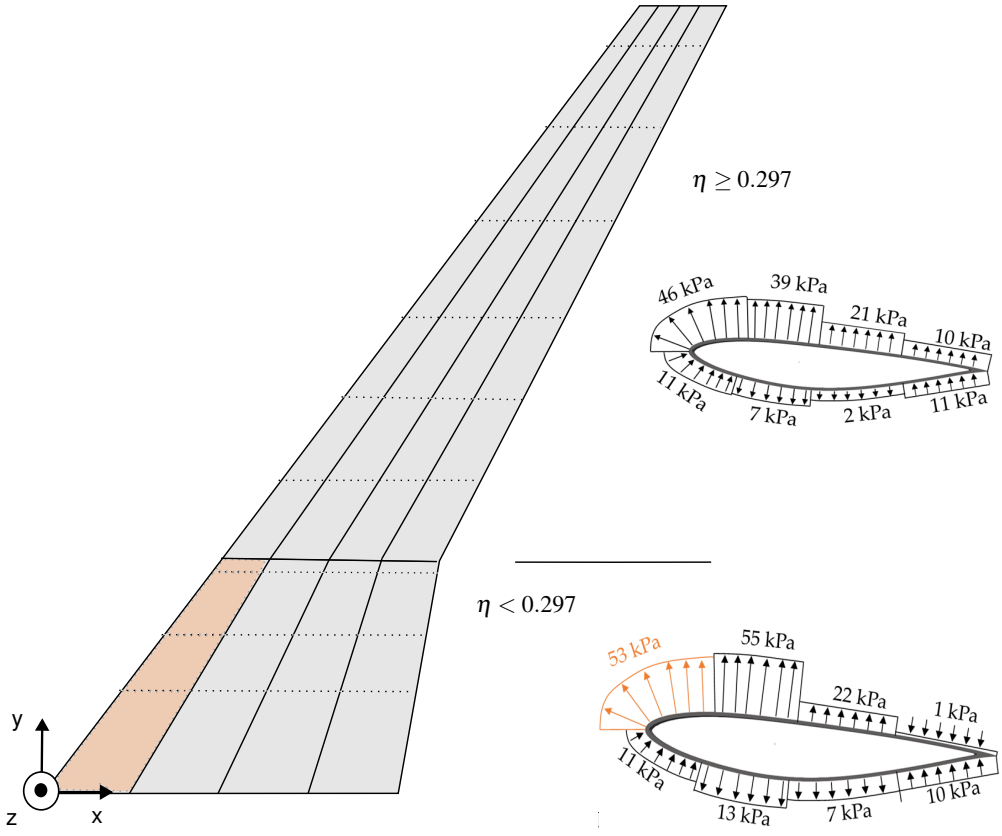

Figure 8.6 Airfoil wing structure (NASA, 2022) and corresponding averaged pressure results experimentally gained by TNA ESWIRP ETW (2014). The variable η describes the relative position in spanwise direction.

Aircraft wings are commonly constructed with fibre-reinforced materials, often consisting of multiple layers of varying fibre orientations. For this analysis, one uni-directional carbon fibre reinforced epoxy layer is assumed, with the material parameters given in Table 8.3. An orthotropic material model represents the varying material properties of fibre and matrix with

the first direction corresponding to the x-axis, and the second direction corresponding to the y-axis, as shown in Fig. 8.6. The fibre direction is defined as the positive rotation around the z-axis, starting with zero degree aligned with the x-axis. The upper and lower part of the wing are represented with individual fibre orientations θ_1 and θ_2. As a hyper-elastic material model is appropriate (Lüders, 2020), a Neo-Hookean material represents the linear elastic regime (Belytschko et al, 2014). To discretise the wing, it is meshed with $242,362$ linear tetrahedral elements with element lengths between 25 and 120mm, resulting in $79,737$ nodes and $239,211$ degrees of freedom.

A common constraint to ensure static stability is to limit the displacement and twist angle at the tip of the wing (Dababneh et al, 2018; Kilimtzidis et al, 2023). Therefore, the tip displacement is restricted to $u_{tip} < 15\% \cdot s = 4.41$, with the semi-span s. To keep the twist angle in a realistic range, we check for $\alpha_{tip} < 6^\circ$. These constraints are met with fibre angles ranging between 40° and 60° degrees. The range also aligns with fibre directions approximately following the wing span.

8.2.2. Hyper-reduced airfoil wing model

To construct suitable reduced order models, training simulations are run with varying design variables θ_1 and θ_2 in a range of $[40^\circ, 60^\circ]$. In total 49 training simulations are sampled based on a full factorial design with an equidistant grid for θ_1 and θ_2. We collect the resulting displacement vectors in the snapshot matrix, which is reformulated via SVD. With a truncation tolerance of $1 \cdot 10^{-6}$ a subspace with $k = 39$ reduced basis is created. For the hyper-reduction, only 12 training simulations are utilised to select the reduced set of elements, due to memory limitations resulting from the large matrix sizes. The 284 hyper-reduced elements, selected through the ECM algorithm are depicted in Fig. 8.7.

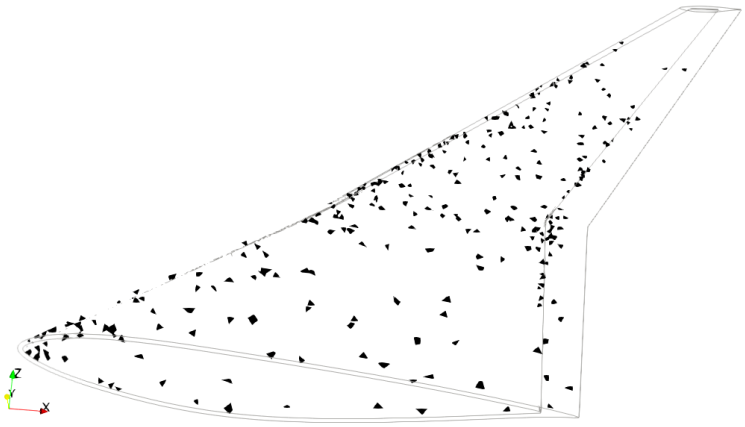

Figure 8.7 Hyper-reduced airfoil wing structure based on 39 reduced basis resulting in 284 selected elements via ECM.

To test the reduced order models, 10 random samples within the design space are computed and compared with the reference solution. Therefore, displacement e_{GMRE} and speedups are depicted in Table 8.4. The e_{GMRE} of the ROM with 2.84×10^{-6} in the decisive y-direction

shows that the global POD approach can sufficiently approximate the current design space. The HROM has a reduced but acceptable mean e_{GMRE} of 3.77×10^{-3} for the same quantity. The measured processing time only contains the projection and solving step and neglects the initial setup and post-processing for a fair comparison. Since in this example only 0.001% percent of the element are included in the hyper-reduced mesh, the remarkable speedup factor of 2000 is achieved.

Table 8.4 Evaluation of the displacement e_{GMRE} for all three dimensions and the computational speedup of the ROM, HROM, and NiROM with varying regression models.

model	e_{GMRE}			speedup
	x	y	z	
ROM	1.23×10^{-5}	2.84×10^{-6}	2.25×10^{-6}	12.51
HROM	2.97×10^{-3}	3.77×10^{-3}	4.02×10^{-3}	2452.10
NiROM - PolyR	2.21×10^{-1}	2.95×10^{-2}	2.30×10^{-2}	61884.06
NiROM - kNN	1.48×10^{-1}	5.00×10^{-2}	4.84×10^{-2}	48542.87
NiROM - GPR	1.50×10^{-2}	1.28×10^{-3}	6.69×10^{-4}	56113.65

For the non-intrusive approach, all three regression models are tested. Therefore, only 12 training simulations are used within the training space to create a fair comparison between intrusive and non-intrusive MOR.

For PolyR and kNN a hyper-parameter study with 5-fold cross-validation is conducted to find the optimal polynomial degree and number of neighbours, respectively. Therefore, the displacement e_{GMRE} corresponding to the test and training data is computed to judge the constructed models. On the left of Fig. 8.8 the testing error is plotted in grey, and the training error is visualised in blue for increasing polynomial degrees. It is visible that the lowest testing error can be found with a polynomial degree of $p = 5$. With polynomials $p < 5$, the training and testing errors are simultaneously decreasing, while a divergent trend for $p > 5$ indicates the start of overfitting. For the kNN regression model, we observe the lowest testing error with $k = 2$ neighbours in Fig. 8.8, on the right. The sparse training data explains the low number of neighbours and the relatively poor performance. The GPR is constructed with an RBF kernel with an isotropic correlation length of 50. Here, the hyper-parameter is found through a gradient-based optimisation study. The corresponding speedups for the non-intrusive models are in a comparable range of 10^4, summarised in Table 8.4.

8.2.3. Optimisation study to minimise the twist angle

An optimisation study of the presented airfoil wing is conducted with the multi-fidelity MOR approach. Minimising the twist angle at the tip of the wing is chosen as an objective to illustrate the capabilities of the robust optimisation approach. The design variables are θ_1 and θ_2, the fibre orientations for the upper and lower skin. Consequently, the optimisation problem can be

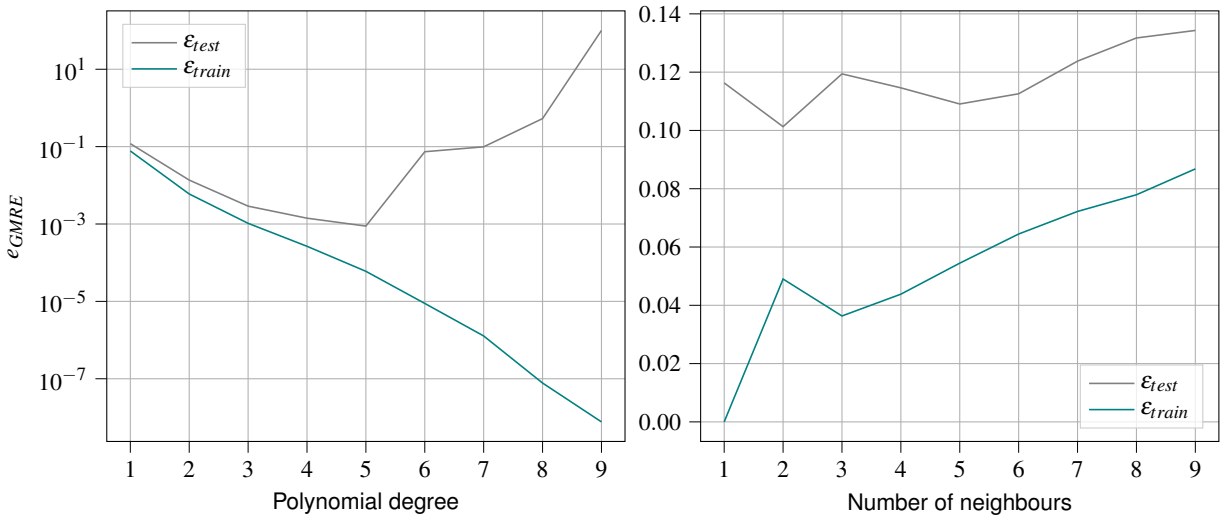

Figure 8.8 Hyper-parameter study with 5-fold cross-validation for PolyR and kNN to find the optimal polynomial degree and number of neighbours for NiROMs.

defined with the following objective function:

$$\begin{aligned} &\text{minimise} \qquad f(\theta_i) = \frac{\alpha_{tip}(\theta_i)}{\alpha_0} + \frac{\sigma^2(\theta_i)}{\sigma_0^2}, \\ &\text{such that} \qquad 40^\circ \leq \theta_i \leq 60^\circ; \qquad\qquad \theta_i \in \mathbb{R}, i = 1,2. \end{aligned} \tag{8.2}$$

Equation (8.2) combines the twist angle at the tip α_{tip} and the robustness criterion σ^2 in the objective function. This contrasts to the previous example in Section 8.1.3, where the robustness criterion is considered as a constraint. Here, the multi-objective problem is combined to a single-objective function with a weighted sum. As the weights are set to one, they are neglected in the above equation. To compute the twist angle, we evaluate

$$\alpha_{tip} = \arctan\left(\frac{\delta_{max} - \delta_{min}}{c_{tip}}\right), \tag{8.3}$$

with δ_{max} the maximum displacement and δ_{min} the minimal displacement of the tip in the vertical direction, and c_{tip} the chord length at the tip (Dababneh et al, 2018; Kilimtzidis et al, 2023). The simulation to evaluate the twist angle represents the outer optimisation loop and is executed with the intrusive model.

The robustness measure is represented by the variance σ^2 in Eq. (8.3). The evaluation of the variance-based criterion is approximated by Latin hypercube sampling in the vicinity of the corresponding candidates $\boldsymbol{x} = (\theta_1, \theta_2)^T$. The sensitivity of the objective function to random deviations in the design variables is set to $\pm 0.5^\circ$. Thus, candidates $\boldsymbol{x}_j$ are sampled within the neighbourhood defined by

$$\boldsymbol{x_j} = \left(\theta_1^j, \theta_2^j\right), \quad \text{with } \theta_i^j \in [\theta_i - 0.5^\circ, \theta_i + 0.5^\circ], \tag{8.4}$$

for robustness evaluation. If the current sample x is close to the limits of the design variables, the neighbourhood is adjusted so that the samples remain within the design space. Normalisation coefficients α_0 and σ_0^2 are introduced to combine the two objectives in an equal manner. They are obtained by a standard optimisation that neglects the robustness criterion. Consequently, the robust optimum is expected to have an objective function value $f_i/f_0 > 1$ and a normalised variance $\sigma_i^2/\sigma_0^2 < 1$. The overall fitness is then a sum of the normalised twist angle and its normalised variance.

The optimisation algorithm is based on a differential evolution strategy and is executed with an initial population of 10, a differentiation constant $F = [0.5, 1]$, a crossover constant of $C_r = 0.5$, and a *rand/1/bin* strategy to avoid convergence to local minima. Furthermore, the optimisation algorithm is terminated if a tolerance of $1 \cdot 10^{-8}$ is reached or after 10 generations.

The results of the multi-fidelity optimisation study are shown in Fig. 8.9 that highlight the global optimum x_0 and the robust optimum x_r. Evaluated by HROM analyses, the objective function is plotted in the background. A minimum determined by the non-robust optimisation is found with the fibre angles $\theta_1 = 48.07°$ and $\theta_2 = 52.54°$. Moreover, the corresponding objective function and variance values are stated in Table 8.5 in the first row.

Table 8.5 Global and robust minimum found by the optimisation algorithm exploiting the multi-fidelity MOR scheme and the corresponding reference FOM analysis.

Optimum	θ_1 [°]	θ_2 [°]	model	α_{tip} [°]	σ^2 [(°)^2]
global x_0	48.07	52.54	HROM/GPR	6.141×10^{-2}	5.862×10^{-4}
			FOM	6.575×10^{-2}	5.155×10^{-4}
robust x_r	41.77	55.07	HROM/GPR	7.391×10^{-2}	1.740×10^{-4}
			FOM	7.317×10^{-2}	1.348×10^{-4}

To evaluate a robust minimum, the presented multi-fidelity (MF) approach applies the HROM and non-intrusive model with GPR. Therefore, 100 evaluations of the low-fidelity model are used to approximate the variance for the robustness criterion. The optimal design is found with the design variables $\theta_1 = 41.77°$ and $\theta_2 = 55.07°$, with a slightly higher twist angle and a reduced variance from $5.9 \cdot 10^{-4}$ to $1.7 \cdot 10^{-4}$. Here, the optimisation algorithm is terminated when the maximum number of iterations is reached. With the contour plot, the convergence of the robust optimum can be visually confirmed. Therefore, no further optimisation study, with e.g. different initial parameter settings, is performed to improve the convergence behaviour.

As a robust optimisation based on FOMs would have infeasible costs, only simulations with the optimal design variables are carried out. In Table 8.5 reference solutions for the twist angles and its variances are stated for the absolute and robust minimum. For the FOM analysis, the variance is approximated with only 10 sample points. The reader can observe that the results of the twist angle and its variance slightly vary between HROM and FOM, due to its approximation error. However, the comparison between global and robust optimum shows a

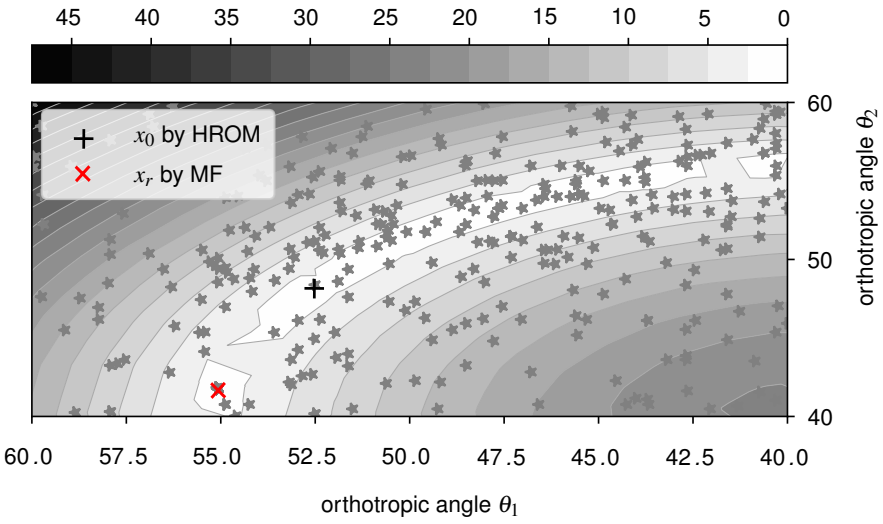

Figure 8.9 Performed multi-fidelity optimisation study based on HROM and NiROM resulting in a global optimum x_0 and the robust optimum x_r.

correct identification. Consequently, we can confirm that the proposed optimisation scheme is capable of finding a robust optimum.

As a last step, the cost associated with the optimisation study is evaluated. Approximately 420 designs are analysed by the HROM during the robust optimisation procedure. Furthermore, the neighbourhood is explored with 100 low-fidelity samples for each design, resulting in a total of $42,000$ model evaluations. Combining the offline and online costs of the robust optimisation results in a total processing time of $16,686$ s. A robust optimisation based solely on FOM would have incurred a cost of 7×10^6 s. Thus, the presented scheme offers a speedup of 466 and compensates for the expenses of the training phase. Even in comparison to a FOM-based analysis utilising only 10 individuals to approximate the variance, the presented scheme would still provide a speedup of 51.

8.3. Concluding remarks on multi-fidelity scheme

Within this chapter, the multi-fidelity scheme has been successfully applied to robust optimisation studies. A robust position of a hole within a beam under damage represented the first application case. Through a fibre optimisation of an airfoil wing, the efficiency of the proposed multi-fidelity scheme could be confirmed.

The first example focused on the variance-based robustness criterion and the adaptively updated non-intrusive model. Similarly, to Chapter 7 the update can improve the accuracy of the NiROM. The enhancement depends on the initial quality of the non-intrusive scheme and its

effect is reduced if the initial approximation quality is relatively high. However, only previously available data are used and a limited additional effort is needed for the retraining step.

Secondly, we showed that the robustness criterion has a measurable effect on the optimisation study, and robust optima that are insensitive to small variations in the design variables can be found. To consider the robustness criterion, it can be incorporated as a constraint, as in Section 8.1 and within the objective function shown in Section 8.2. For variance evaluation, the application of high- and low-fidelity models is interchangeable and can be defined according to its importance within the optimisation study. The first example approximates the variance with the high-fidelity model. With the second optimisation of an airfoil wing, this was exchanged. Here, the twist angle is evaluated with the high-fidelity model, and the variance is evaluated with the low-fidelity model.

The second example is closer to an industrial application case with approximately $240,000$ elements. It is observable that the proposed multi-fidelity approach is well applicable to large-scale problems. In addition, the achievable speedups are highest in this example compared to the others.

With the second example, a previously occurred limitation becomes apparent. In general, we have assumed that the intrusive MOR approach has a higher accuracy level than the non-intrusive scheme. However, for the airfoil wing optimisation, the regression model based on GPR has a similar precision. This has also been observed in Chapter 5 for the enlarged parameters space of the crash box optimisation. The question can be raised whether the additional implementation complexity of intrusive MOR is reasonable. Moreover, the retraining step of the low-fidelity model should be neglected if the precision levels are similar.

Even if the second optimisation study shows a very suitable application of GPR, an expanded training data set could cause reduced efficiency. As in GPR the inverse of the covariance matrix must be calculated, classical GPR reaches its limits for large data sets.

Overall, the two robust optimisation schemes illustrated the general applicability of the multi-fidelity scheme. Not only for uncertainty propagation, as presented in Chapter 7, but also for optimisation algorithms, the combination of intrusive and non-intrusive MOR approaches can efficiently enable these cost-intensive analyses.

Part V

Conclusion

Chapter 9

Conclusion

9.1. Conclusion

This thesis presented a novel bi-fidelity architecture based on data-driven and projection-based MOR for analysis under uncertainties. Snapshots from full-order FE analysis are evaluated via POD to identify an underlying lower dimensional representation. The Galerkin projection transforms the system of equations into the subspace with fewer unknowns. This is complemented by a hyper-reduction step constructed through ECSW or ECM to further reduce the analysis cost. We add a non-intrusive approach to the intrusive MOR, which is based on the identical subspace. Therefore, the basis vectors are combined within a weighted sum, whereby the unknown weights are determined through a regression model. The low implementation complexity and evaluation cost extend the intrusive approach forming a multi-fidelity scheme to improve the efficiency of multi-query analysis.

From a model management point of view, the low-fidelity model follows the principle of adaptation. In particular, the non-intrusive low-fidelity model can be updated after additional high-fidelity results are available. The snapshot-based approach allows the combination of full-order and intrusive MOR results, such that the non-intrusive model is retrained when additional high-fidelity results are available. We could show that this improves the accuracy of the low-fidelity model by adding insignificant additional costs.

With a range of example studies, the modularity of the proposed architecture is highlighted.

Optimisation under uncertainties and uncertainty propagation have been presented as suitable double-loop examples, leading to a generally applicable scheme. The multi-fidelity strategy was adopted for the control variate approach, blending high-fidelity and low-fidelity models to estimate second-order statistics. The global MOR method is especially beneficial for uncertainty propagation, as the entire design space is required to statistically evaluate the output quantity. Using an example study, we could show that the presented algorithm can achieve significant efficiency gains. In addition, we demonstrated the proposed multi-fidelity scheme for robust optimisation studies. The low- and high-fidelity models are interchangeable for the evaluation of objective function and robustness criterion. As the loops are recursively executed, costs significantly increase. For large-scale FE analyses, the multi-fidelity scheme enables optimisation under uncertainties that would otherwise be prohibitively expensive.

With application to multiple example studies, intrusive and non-intrusive MOR techniques for structural multi-query analysis were investigated in detail. The MOR methods are analysed for parametric problems with nonlinearities in material, geometry, and boundary conditions through the varying application cases. Concerning the projection-based reduced order models, the following statements can be summarised for application in structural optimisation and uncertainty propagation.

To identify the subspace of the MOR techniques, snapshots from previously computed full-order simulations are collected. The main advantage of snapshot-based POD is that the scheme is widely applicable. Training simulations can be easily created for different parameter spaces, such as varying boundary conditions or material properties. Furthermore, the approach is extendable to more complex parametric problems, as shown for random fields describing material inhomogeneities. Another advantage of the presented intrusive and non-intrusive technique is the seamless extension to transient analysis. For the intrusive scheme with Galerkin projection and ECM hyper-reduction, an implicit or explicit time integration scheme can be used. The time parameter was taken as an additional input parameter for the non-intrusive approach. This results in different natured parameters within the regression model, which was not observed as a major challenge. For example, in GPR an anisotropic kernel can account for the parameter indifference.

When discussing the scheme's overall efficiency, the trade between accuracy and speedups must be judged. For the evaluation of intrusive MOR, we can conclude on Galerkin projected schemes with the closely related hyper-reduction schemes ECSW and ECM. In general, this trade is particularly good for large models with small parameter changes and a low degree of nonlinearity within the manifold. This is expected as the POD approach is a linear projection technique. It was observed that the limits of the global POD technique are reached when the parameter space is enlarged. A good indication is the snapshot matrix's low decaying rate of singular values. Then, the accuracy level of the intrusive model is significantly reduced. This

became especially apparent for the crash box optimisation and the analysis with two independent heterogeneous material fields. Furthermore, the appearance of local phenomena, such as highly localised damage behaviour, also reveals the limits of the global approach.

For all applications, an overall speedup could be achieved. To reasonably evaluate the cost, also the construction phase must be considered. The main expenses of the construction cost usually correspond to the number of training simulations, which vary for every problem. For non-intrusive models, one can estimate that the online phase must at least contain the number of training simulations to create an efficient scheme. On the other hand, the intrusive framework shows a significant range of speedups, which prohibits a general conclusion. Here, a few hundred evaluations were needed for the presented multi-query analysis with gradient-free optimisation and uncertainty propagation. In these cases, the intrusive MOR scheme resulted in an accelerated workflow, also considering the offline phase.

The non-intrusive schemes show speedups (without construction phase) of magnitude 10^4, which is a significant reduction in computational time. Its implementation effort is relatively low compared to the intrusive method through openly available ML libraries. Surprisingly, for the crash box and airfoil wing optimisation study, the non-intrusive model, similarly performed or even outperformed the intrusive models. This becomes especially apparent when a large parameter space should be covered. Gaussian process regression achieved the highest accuracy measures when choosing between different regression models. For k-nearest neighbours, its simplicity is valuable, especially for validation purposes, as no overfitting can occur. A polynomial regression function lies in between the other two approaches, whereby the very fast online evaluation of the regression function is its main advantage.

In summary, intrusive and non-intrusive projection-based MOR techniques can successfully evaluate structural analysis under uncertainties. The proposed multi-fidelity scheme as a modular framework allows the application to varying double-loop problems. Extending the intrusive MOR by the non-intrusive model adds little additional cost, with a significant advantage for the presented analyses. An apparent drawback is the accuracy and acceleration inconsistency of the intrusive scheme on which the architecture is mainly constructed. The following section provides a critical reflection and suggests improvements for future work.

9.2. Outlook and critical reflection

With the major conclusion summarised in the last section, we critically discuss the proposed techniques and evaluation methods. The first paragraphs concentrate on the intrusive and non-intrusive schemes individually, followed by the multi-fidelity scheme and its specific application.

Projection-based model order reduction techniques

In this thesis, the projection-based MOR uses a global POD approach, combining snapshots from different time instances and parameter configuration to create a global reduced basis. An apparent limitation of the presented intrusive MOR approach can be traced back to the global subspace. The linear projection reaches its limits for problems with low decaying eigenvalue rates, resulting in lower accuracy (Amsallem et al, 2015b; Zimmermann, 2021). This phenomenon was observed for large parameter spaces and localised behaviour. To ensure certain accuracy tolerance, an error measure for the reduced order models should be introduced, see e.g. (Soize and Farhat, 2017; Nurtaj Hossain and Ghosh, 2020).

In the literature, multiple approaches exist that extend the projection capabilities of the intrusive method. A common approach introduces multiple local affine subspaces that define different clusters of behaviour, such as (Amsallem et al, 2012; Vlachas et al, 2021). During the online phase, an algorithm selects the subspace corresponding to the state of the system. The more fundamental idea is to exchange linear projection with a nonlinear method, see e.g. Lee and Carlberg (2020); Fresca and Manzoni (2022). For nonlinear projection methods, the back-and-forth projection cannot be realised with a simple matrix multiplication, which leads to a change of the workflow. Contributions to related problems, such as Touzé et al (2021) on nonlinear projection methods for structural problems with simulation-free approaches, could also be investigated.

One can notice a wide range of speed-ups for the intrusive MOR scheme when comparing the different application cases. To further analyse the processing time, a detailed evaluation of the algorithm would be required. The reduced cost depends on the specific implementation, as the intrusive MOR is embedded in the FE solver. Moreover, the different nonlinearities invoke additional costs to the solver, which are difficult to compare. Therefore, every step of the computation should be quantified, also during the construction phase, to provide an accurate evaluation of the processing time. Two different hyper-reduction algorithms are employed within the theses, as the crash example was conducted using a different solver environment. A general comparison of speedups is difficult as the surrounding implementation restrictions of the FE solver are not comparable. Moreover, we are missing a direct comparison of the two hyper-reduction techniques.

The non-intrusive MOR performs with similar levels of accuracy within different example studies. The most promising regression approach is GPR, as also observed by Kneifl et al (2021). A disadvantage of GPR is its poor scalability for large data sets, as the inverse of the covariance matrix must be performed for each prediction step. Modifications such as sparse Gaussian processes (Snelson and Ghahramani, 2005) or recursive cokriging (Gratiet, 2012) are available that handle large data sets more efficiently. Furthermore, other sophisticated

non-intrusive techniques based on auto-encoder, such as Partin et al (2023) open the potential for further improvement.

Multi-fidelity model management

This thesis's multi-fidelity scheme merges non-intrusive and intrusive methods, with the latter as the high-fidelity model. The intrusive MOR approach as a high-fidelity model can be critically discussed, as it already contains a simplification and, thus, an approximation error. As an additional fidelity level, full-order analysis could be incorporated into the multi-fidelity architecture to circumvent this approximation step.

An obvious choice is to reuse the training simulations from snapshot-based approaches within the multi-query scheme. Therefore, a sampling strategy already adapted to the online phase would be beneficial. The idea is particularly suitable for control variate estimators, as the theoretical concept is derived for multiple numbers of fidelity levels.

In the proposed scheme, we assumed that the intrusive level reaches higher accuracy than the non-intrusive one. As the intrusive and non-intrusive methods have similar accuracy for some use cases, automated error measures are necessary to quantify and assure this assumption. In these cases, enhancing the intrusive scheme is inevitable to ensure high accuracy levels. Through the modular structure of the multi-fidelity architecture a straightforward integration of multiple affine subspaces would be possible.

Furthermore, estimators that quantify the correlation between models should be implemented to improve the model management strategy, such as proposed by Peherstorfer et al (2016). It would also be interesting to apply the proposed multi-fidelity scheme to other areas of multi-fidelity analysis, such as inference.

Model order reduction tailored to optimisation studies

The proposed multi-fidelity scheme consists of varying modules to create a general workflow suitable to different double-loop algorithms. Modularity is an advantage, enabling the application to diverse problems, but simultaneously a disadvantage, as solutions specifically tailored to the analysis are often more efficient.

For example, the global POD creates a reduced basis for the entire design space, which is required for the uncertainty propagation problem. In contrast, only the optimum and its neighbourhood are essential for robust optimisation, and the rest of the design space is of minor interest. The optimisation algorithm evaluates points in the entire design space to find the minimum. However, the exact system answer is only demanded at the minimum of the objective function. The multi-fidelity model management strategy should consider this fact when creating efficient reduced-order models, especially with the apparent accuracy issues of the global POD. One idea is the combination of multi-fidelity approaches with trust region

optimisation (Zahr et al, 2019; Wen and Zahr, 2023). Another strategy is to develop a two-step optimisation scheme, first identifying the domain of interest before performing a precise optimisation, as proposed, e.g. by Li et al (2018). To better explore the specific attributes of the population-based algorithm, one could also investigate the inherent robustness of the optimisation strategies (Beyer and Sendhoff, 2006).

In future work, the multi-fidelity scheme could also optimise multi-scale design problems. Publications, such as Zahr et al (2017); Hernández (2020); Caicedo et al (2019), proposed MOR techniques in the scope of multi-scale analysis. An interesting combination could be a multi-fidelity scheme for multi-scale optimisation algorithms, which are commonly based on linear structural analysis (Murphy et al, 2021).

Appendix

Appendix A

Following, the detailed equations for the calculation of the control variate estimators for the mean $\hat{\mu}_1^{CV}$ and variance $\hat{\mu}_2^{CV}$ are given. The control variate estimator of the mean $\hat{\mu}_1^{CV}$ can be formulated according to Eq. (2.22) with the variables $A_1 - A_4$:

$$\begin{aligned} A_1 &= \frac{\hat{\mu}_{2,0}(y,\tilde{y},\Theta_n)}{n}, \quad A_2 = \frac{\hat{\mu}_{1,1}(y,\tilde{y},\Theta_n)}{n}, \\ A_3 &= \frac{\hat{\mu}_{0,2}(y,\tilde{y},\Theta_n)}{n}, \quad A_4 = \frac{\hat{\mu}_{0,2}(y,\tilde{y},\Theta_m)}{m}, \end{aligned} \tag{9.1}$$

with high-fidelity y and low-fidelity $\tilde{y}$ responses and sample sets θ_n and θ_m.

The control variate estimator of the variance $\hat{\mu}_2^{CV}$ is given in Eq. (2.28) with the variables $B_1 - B_4$:

$$\begin{aligned} B_1 &= \frac{\hat{\mu}_{4,0}(y,\tilde{y},\Theta_n)}{n} - \frac{(n-3)\hat{\mu}_{2,0}^2(y,\tilde{y},\Theta_n)}{(n-1)n}, \quad B_2 = \frac{2\hat{\mu}_{1,1}^2(y,\tilde{y},\Theta_n)}{(n-1)n} + \frac{\hat{\mu}_{2,2}(y,\tilde{y},\Theta_n)}{n} - \frac{\hat{\mu}_{2,0}\hat{\mu}_{0,2}(y,\tilde{y},\Theta_n)}{n}, \\ B_3 &= \frac{\hat{\mu}_{0,4}(y,\tilde{y},\Theta_n)}{n} - \frac{(n-3)\hat{\mu}_{2,0}^2(y,\tilde{y},\Theta_n)}{(n-1)n}, \qquad B_4 = \frac{\hat{\mu}_{0,4}(y,\tilde{y},\Theta_m)}{m} - \frac{(m-3)\hat{\mu}_{2,0}^2(y,\tilde{y},\Theta_m)}{(m-1)m}, \end{aligned} \tag{9.2}$$

The corresponding estimations of the co-moments $\hat{\mu}_{p,q}$ are stated in Eq. (9.3) - (9.13) and formulated in a general way depending on the sample set θ_l, including l number of samples. The co-moments are given dependent on $s_{p,q}$:

$$s_{p,q} = \sum_{i=1}^{l} (y(\theta_i))^p (\tilde{y}(\theta_i))^q, \tag{9.3}$$

with θ_i, the i-th sample of the sample set θ_l. The required co-moments are depicted in the equations below (González et al, 2019).

$$\hat{\mu}_{1,1} = \frac{l s_{1,1} - s_{0,1} s_{1,0}}{(l-1)l}. \tag{9.4}$$

$$\hat{\mu}_{2,0} = \frac{l s_{2,0} - s_{1,0}^2}{(l-1)l}. \tag{9.5}$$

$$\hat{\mu}_{0,2} = \frac{l s_{0,2} - s_{0,1}^2}{(l-1)l}. \tag{9.6}$$

$$\hat{\mu}_{2,2} = \frac{1}{(l-3)(l-2)(l-1)l}((-2l^2+4l-6)s_{2,1}s_{0,1} + (-2l^2+4l-6)s_{1,0}s_{1,2} + (l^3-2^2+3l)s_{2,2} + ls_{2,0}s_{0,1}^2 + 4ls_{1,0}s_{1,1}s_{0,1} + ls_{0,2}s_{1,0}^2 + (6-4l)s_{1,1}^2 + (3-2l)s_{0,2}s_{2,0} - 3s_{1,0}^2s_{0,1}^2) \tag{9.7}$$

$$\hat{\mu}_{4,0} = \frac{1}{(l-3)(l-2)(l-1)l}((-4l^2+8l-12)s_{3,0}s_{1,0} + (l^3-2l^2+3l)s_{4,0} + 6ls_{2,0}s_{1,0}^2 + (9-6l)s_{2,0}^2 - 3s_{1,0}^4) \tag{9.8}$$

$$\hat{\mu}_{0,4} = \frac{1}{(l-3)(l-2)(l-1)l}((-4l^2+8l-12)s_{0,3}s_{0,1} + (l^3-2l^2+3l)s_{0,4} + 6ls_{0,2}s_{0,1}^2 + (9-6l)s_{0,2}^2 - 3s_{0,1}^4) \tag{9.9}$$

$$\hat{\mu}_{1,1}^2 = \frac{1}{(l-3)(l-2)(l-1)l}((l^2-3l+2)s_{1,1}^2 + (l-l^2)s_{2,2} + (2-2l)s_{1,0}s_{1,1}s_{0,1} + (2l-2)s_{2,1}s_{0,1} + (2l-2)s_{1,0}s_{1,2} + s_{1,0}^2s_{0,1}^2 - s_{2,0}s_{0,1}^2 - s_{0,2}s_{1,0}^2 + s_{0,2}s_{2,0}) \tag{9.10}$$

$$\hat{\mu}_{2,0}^2 = \frac{(l^2-3l+3)s_{2,0}^2 + (l-l^2)s_{4,0} - 2ls_{2,0}s_{1,0}^2 + (4l-4)s_{3,0}s_{1,0} + s_{1,0}^4}{(l-3)(l-2)(l-1)l} \tag{9.11}$$

$$\hat{\mu}_{0,2}^2 = \frac{(l^2-3l+3)s_{0,2}^2 + (l-l^2)s_{0,4} - 2ls_{0,2}s_{0,1}^2 + (4l-4)s_{0,3}s_{0,1} + s_{0,1}^4}{(l-3)(l-2)(l-1)l} \tag{9.12}$$

$$\hat{\mu}_{2,0}\hat{\mu}_{0,2} = \frac{1}{(l-3)(l-2)(l-1)l}((l^2-3l+1)s_{0,2}s_{2,0} + (l-l^2)s_{2,2} + (2-l)s_{2,0}s_{0,1}^2 + (2l-2)s_{2,1}s_{0,1} + (2-l)s_{0,2}s_{1,0}^2 + (2l-2)s_{1,0}s_{1,2} + s_{1,0}^2s_{0,1}^2 - 4s_{1,0}s_{1,1}s_{0,1} + 2s_{1,1}^2) \tag{9.13}$$

Abbreviations

CDF	Cumulative Distribution Function
DE	Differential Evolution
DEIM	Discrete Empirical Interpolation Method
DOE	Design of Experiments
EA	Evolutionary Algorithm
ECM	Empirical Cubature Method
ECSW	Energy Conserving Sampling and Weighting Technique
FE	Finite Element
FEM	Finite Element Method
FOM	Full-Order Model
GPR	Gaussian Process Regression
HBM	Human Body Model
HROM	Hyper-reduced Order Model with Galerkin projection
KL	Karhunen Loève
kNN	k-Nearest Neighbour
MC	Monte Carlo
MFM	Multi-fidelity Model
MFMC	Multi-fidelity Monte Carlo
ML	Machine Learning
MOR	Model Order Reduction
NiROM	Non-intrusive Reduced Order Model
PCA	Principal Component Analysis
PDF	Probability Density Function
POD	Proper Orthogonal Decomposition
PolyR	Polynomial Regression
QoI	Quantity of Interest
ROM	Reduced order model with Galerkin projection
SVD	Singular Value Decomposition
UQ	Uncertainty Quantification

List of Symbols

Error measures

ε_{GMRE} Global mean relative error summed for all time steps

ε_{NMSE} Normalised mean squared error for scalar values

e_{GMRE} Global mean relative error

Multi-fidelity Monte Carlo analysis

Θ_m Model response vector of numerical analysis with m samples

Θ_n Model response vector of numerical analysis with n samples

$\hat{\mu}_i$ Approximated statistical moment of i-th order

μ_i Statistical moment of i-th order

$\tilde{y}$ QoI evaluated with low-fidelity model

m Number of samples for high-fidelity evaluations

n Number of samples for low- and high-fidelity evaluations

y QoI evaluated with high-fidelity model

Optimisation

W Random design or noise variable

$\mathbf{x}_d$ Vector of design variables

f Objective function

g Constraint

Random field

C Covariance function

λ Eigenvalue of auto-covariance function

H Random field $H(z,\theta)$ of the spatial variable z and θ indicating the random aspect

ϕ Eigenvector of auto-covariance function

$\hat{H}$ Approximated random field $\hat{H}(z,\theta)$ of spatial variable z and θ indicating random aspect

Random variables and processes

Cov	Covariance
$E[\cdot]$	Expectation operator
F_X	Cumulative distribution function of continuous random variable X
K	Correlation matrix
$P(\cdot)$	Probability
V	Variance
κ	Correlation function
S	Sample space of random variable X
X	Random variable
$\mathbf{X}$	Random vector $\mathbf{X} = [X_1, X_2, .., X_d]$ with dimension d
x	Realisation of random variable X
μ_X	Mean value of X
ρ	Correlation coefficient
σ_X	Standard deviation of X
$f_X(x)$	Probability density function of continuous random variable X
l_c	Correlation length
z	Parameter of random function $X(z)$

Reduced order models

Σ	Diagonal matrix of SVD transformation, containing singular values σ
$\mathbf{A}$	Snapshot matrix
$\mathbf{U}$	Left-singular vector matrix of SVD transformation
$\mathbf{V}$	Projection matrix
$\mathbf{Z}$	Right-singular vector matrix of SVD transformation
$\mathbf{u}_r$	Displacement vector in reduced space
k	Dimension of reduced space
n	Number of snapshots

Structural Finite Element analysis

E Young's modulus

N Number of degrees of freedom

$\mathbf{M}$ Mass matrix

$\mathbf{f}$ Internal force vector

$\mathbf{g}$ External force vector

$\mathbf{u}$ Displacement vector with the corresponding velocity $\dot{\mathbf{u}}$ and acceleration $\ddot{\mathbf{u}}$ vector

ν Poisson's ratio

ρ Mass density

List of Figures

List of Tables

Bibliography

Acar E, Bayrak G, Jung Y, Lee I, Ramu P, Ravichandran SS (2021) Modeling, analysis, and optimization under uncertainties: a review. Struct Multidiscip Optim 64(5):2909–2945, doi:10.1007/s00158-021-03026-7

Amsallem D, Zahr MJ, Farhat C (2012) Nonlinear model order reduction based on local reduced-order bases. Int J Numer Methods Eng 92(10):891–916, doi:10.1002/nme.4371

Amsallem D, Zahr MJ, Choi Y, Farhat C (2015a) Design optimization using hyper-reduced-order models. Struct Multidiscip Optim 51(4):919–940, doi:10.1007/s00158-014-1183-y

Amsallem D, Zahr MJ, Washabaugh K (2015b) Fast local reduced basis updates for the efficient reduction of nonlinear systems with hyper-reduction. Adv Comput Math 41(5):1187–1230, doi:10.1007/s10444-015-9409-0

Arsenyev I (2018) Efficient Surrogate-based Robust Design Optimization Method. PhD thesis, Technical University of Munich, Munich, Germany

Avramidis AN, Wilson JR (1993) A splitting scheme for control variates. Oper Res Lett 14(4):187–198, doi:10.1016/0167-6377(93)90069-S

Bach C (2020) Data-driven model order reduction for nonlinear crash and impact simulations. PhD thesis, Technical University of Munich, Munich, Germany

Bach C, Song L, Erhart T, Duddeck F (2018) Stability conditions for the explicit integration of projection based nonlinear reduced-order and hyper reduced structural mechanics finite element models. arXiv Prepr 1806.11404

Bach C, Ceglia D, Song L, Duddeck F (2019) Randomized low-rank approximation methods for projection-based model order reduction of large nonlinear dynamical problems. Int J Numer Methods Eng 118(4):209–241, doi:10.1002/nme.6009

Bak C, Gaudern N, Zahle F, Vronsky T (2014) Airfoil design: Finding the balance between design lift and structural stiffness. J Phys Conf Ser 524:012017, doi:10.1088/1742-6596/524/1/012017

Balokas G, Kriegesmann B, Czichon S, Rolfes R (2021) A variable-fidelity hybrid surrogate approach for quantifying uncertainties in the nonlinear response of braided composites. Comput Methods Appl Mech Eng 381:113851, doi:10.1016/j.cma.2021.113851

Belytschko T, Liu WK, Moran B, Elkhodary KI (2014) Nonlinear finite elements for continua and structures, 2nd edn. John Wiley & Sons, Ltd, Chichester, UK

Benner P, Gugercin S, Willcox K (2015) A Survey of Projection-Based Model Reduction Methods for Parametric Dynamical Systems. SIAM Rev 57(4):483–531, doi:10.1137/130932715

Benner P, Grivet-Talocia S, Quarteroni A, Rozza G, Schilders W, Silveira LM (2021a) Model Order Reduction, Volume 2: Snapshot-Based Methods and Algorithms, vol 2. Walter de Gruyter GmbH, Berlin/Boston, doi:10.1515/9783110671490

Benner P, Grivet-Talocia S, Quarteroni A, Rozza G, Schilders W, Silveira LMS (2021b) Model Order Reduction, Volume 1: System- and Data-Driven Methods and Algorithms. Walter de Gruyter GmbH, Berlin/Boston, doi:10.1002/9781119294474

Benner P, Grivet-Talocia S, Quarteroni A, Rozza G, Schilders W, Silveira LMS (2021c) Model Order Reduction, Volume 3: Applications. Walter de Gruyter GmbH, Berlin/Boston, doi:10.1515/9783110499001

Bentley JL (1975) Multidimensional binary search trees used for associative searching. Commun ACM 18(9):509–517, doi:10.1145/361002.361007

Betz W, Papaioannou I, Straub D (2014) Numerical methods for the discretization of random fields by means of the Karhunen–Loève expansion. Comput Methods Appl Mech Eng 271:109–129, doi:10.1016/j.cma.2013.12.010

Beyer HG, Sendhoff B (2006) Evolution Strategies for Robust Optimization. In: 2006 IEEE Int. Conf. Evol. Comput., pp 1346–1353, doi:10.1109/CEC.2006.1688465

Beyer HG, Sendhoff B (2007) Robust optimization – A comprehensive survey. Comput Methods Appl Mech Eng 196(33-34):3190–3218, doi:10.1016/j.cma.2007.03.003

Bishop CM (2006) Pattern Recognition and Machine Learning. Springer Science+Business Media, New York, NY, USA

Blonigan P, Geraci G, Rizzi F, Eldred MS (2020) Towards an integrated and efficient framework for leveraging reduced order models for multifidelity uncertainty quantification. AIAA Scitech 2020 Forum 1 PartF:1–21, doi:10.2514/6.2020-0420

Boyaval S (2012) A fast Monte-Carlo method with a reduced basis of control variates applied to uncertainty propagation and Bayesian estimation. Comput Methods Appl Mech Eng 241-244:190–205, doi:10.1016/j.cma.2012.05.003

Boyaval S, Bris CL, Maday Y, Nguyen NC, Patera AT (2009) A reduced basis approach for variational problems with stochastic parameters: Application to heat conduction

with variable Robin coefficient. Comput Methods Appl Mech Eng 198(41-44):3187–3206, doi:10.1016/j.cma.2009.05.019

Boyd S, Vandenberghe L (2004) Convex optimization. Cambridge University Press, Cambridge, UK

Brandner R, Schickhofer G (2014) Spatial correlation of tensile perpendicular to grain properties in Norway spruce timber. Wood Sci Technol 48(2):337–352, doi:10.1007/s00226-013-0606-z

Bui-Thanh T, Willcox K, Ghattas O (2008) Model Reduction for Large-Scale Systems with High-Dimensional Parametric Input Space. SIAM J Sci Comput 30(6):3270–3288, doi:10.1137/070694855

Bulleit WM, Chapman RA (2004) Characterization of the correlation structure of lumber strength properties. Wood Sci Technol 38(4):285–296, doi:10.1007/s00226-004-0234-8

Caicedo M, Mroginski JL, Toro S, Raschi M, Huespe A, Oliver J (2019) High Performance Reduced Order Modeling Techniques Based on Optimal Energy Quadrature: Application to Geometrically Non-linear Multiscale Inelastic Material Modeling. Arch Comput Methods Eng 26(4):771–792, doi:10.1007/s11831-018-9258-3

Carlberg K, Farhat C, Cortial J, Amsallem D (2013) The GNAT method for nonlinear model reduction: Effective implementation and application to computational fluid dynamics and turbulent flows. J Comput Phys 242:623–647, doi:10.1016/j.jcp.2013.02.028

Carlberg K, Barone M, Antil H (2017) Galerkin v. least-squares Petrov–Galerkin projection in nonlinear model reduction. J Comput Phys 330:693–734, doi:10.1016/j.jcp.2016.10.033

Chaturantabut S, Sorensen DC (2010) Nonlinear Model Reduction via Discrete Empirical Interpolation. SIAM J Sci Comput 32(5):2737–2764, doi:10.1137/090766498

Chen P, Quarteroni A, Rozza G (2017) Reduced Basis Methods for Uncertainty Quantification. SIAM/ASA J Uncertain Quantif 5(1):813–869, doi:10.1137/151004550

Chen W, Allen JK, Tsui K, Mistree F (1996) A Procedure for Robust Design: Minimizing Variations Caused by Noise Factors and Control Factors. J Mech Des 118:478–485

Chen Y, Xu F, Zhang Z, Wu K, Z D (2019) Discrete optimization design of tailor-welded blanks (TWBs) thin-walled structures under dynamic crashing. Int J Automot Technol 20(2):265–275, doi:10.1007/s12239-019-0026-7

Cicci L, Fresca S, Manzoni A (2022) Deep-HyROMnet: A Deep Learning-Based Operator Approximation for Hyper-Reduction of Nonlinear Parametrized PDEs. J Sci Comput 93(2):57, doi:10.1007/s10915-022-02001-8

Conti P, Guo M, Manzoni A, Hesthaven JS (2023) Multi-fidelity surrogate modeling using long short-term memory networks. Comput Methods Appl Mech Eng 404:115811, doi:10.1016/j.cma.2022.115811

Czech C, Kaps A, Duddeck F (2022a) Robust multi-fidelity optimization approach exploiting data-driven , non-linear model order reduction. In: Beer M, Zio E, Phoon KK, Ayyub BM (eds) Proc. 8th Int. Symp. Reliab. Eng. Risk, Research Publishing, Singapore, Hannover, Isrerm, pp 357–363, doi:10.3850/978-981-18-5184-1_MS-12-041-cd, URL https://rpsonline.com.sg/rps2prod/isrerm2022/epro/pdf/MS-12-041.pdf

Czech C, Lesjak M, Bach C, Duddeck F (2022b) Data-driven models for crashworthiness optimisation: intrusive and non-intrusive model order reduction techniques. Struct Multidiscip Optim 65(7):1–15, doi:10.1007/s00158-022-03282-1

Dababneh O, Kipouros T, Whidborne J (2018) Application of an Efficient Gradient-Based Optimization Strategy for Aircraft Wing Structures. Aerospace 5(1):3, doi:10.3390/aerospace5010003

Dadvand P, Rossi R, Oñate E (2010) An Object-oriented Environment for Developing Finite Element Codes for Multi-disciplinary Applications. Arch Comput Methods Eng 17:253–297, doi:10.1007/s11831-010-9045-2

Dadvand P, Rossi R, Gil M, Martorell X, Cotela J, Juanpere E, Idelsohn S, Oñate E (2013) Migration of a generic multi-physics framework to HPC environments. Comput Fluids 80:301 – 309, doi:10.1016/j.compfluid.2012.02.004

Duan L, Sun G, Cui J, Chen T, Cheng A, Li G (2016) Crashworthiness design of vehicle structure with tailor rolled blank. Struct Multidiscip Optim 53(2):321–338, doi:10.1007/s00158-015-1315-z

Eckart C YG (1936) The approximation of one matrix by another of lower rank. Psychometrika 1(3):211–218, doi:10.1007/BF02288367

Fang J, Sun G, Qiu N, Kim NH, Li Q (2017) On design optimization for structural crashworthiness and its state of the art. Struct Multidiscip Optim 55(3):1091–1119, doi:10.1007/s00158-016-1579-y

Farhat C, Avery P, Chapman T, Cortial J (2014) Dimensional reduction of nonlinear finite element dynamic models with finite rotations and energy-based mesh sampling and weighting for computational efficiency. Int J Numer Methods Eng 98(9):625–662, doi:10.1002/nme.4668

Farhat C, Chapman T, Avery P (2015) Structure-preserving, stability, and accuracy properties of the energy-conserving sampling and weighting method for the hyper reduction of

nonlinear finite element dynamic models. Int J Numer Methods Eng 102(5):1077–1110, doi:10.1002/nme.4820

Farhat C, Grimberg S, Manzoni A, Quarteroni A (2020) 5 Computational bottlenecks for PROMs: precomputation and hyperreduction. In: Model Order Reduction, Vol. 2 Snapshot-Based Methods Algorithms, Walter de Gruyter GmbH, Berlin/Boston, pp 181–244, doi:10.1515/9783110671490-005

Feoktistov V (2006) Differential evolution: In search of solutions, vol. 5 edn. Springer Science+Business Media, New York, NY, USA

Fina M, Faes MGR, Valdebenito MA, Wagner W, Broggi M, Beer M, Freitag S (2022) Estimation of Second-order Statistics of Buckling Loads Applying Linear and Nonlinear Analysis. In: Beer M, Zio E, Phoon KK, Ayyub BM (eds) Proc. 8th Int. Symp. Reliab. Eng. Risk, Research Publishing, Singapore, Hannover, pp 502–507, doi:10.3850/978-981-18-5184-1_-MS-15-145-cd

Fink G, Frangi A, Kohler J (2015) Probabilistic approach for modelling the load-bearing capacity of glued laminated timber. Eng Struct 100:751–762, doi:10.1016/j.engstruct.2015.06.015

Fishman GS (1996) Monte Carlo: Concepts, Algorithms, and Applications. Springer Science+Business Media, New York, NY, USA

Fresca S, Manzoni A (2022) POD-DL-ROM: Enhancing deep learning-based reduced order models for nonlinear parametrized PDEs by proper orthogonal decomposition. Comput Methods Appl Mech Eng 388:114181, doi:10.1016/j.cma.2021.114181

Friedman JH, Bentley JL, Finkel RA (1977) An Algorithm for Finding Best Matches in Logarithmic Expected Time. ACM Trans Math Softw 3(3):209–226, doi:10.1145/355744.355745

García DA, Rosales MB (2017) Deflections in sawn timber beams with stochastic properties. Eur J Wood Wood Prod 75(5):683–699, doi:10.1007/s00107-016-1124-0

Gerbrands JJ (1981) On the relationships between SVD, KLT and PCA. Pattern Recognit 14(6):375 – 381

Go L, Jehle JS, Rees M, Czech C, Peldschus S, Duddeck F (2023) Model order reduction techniques to identify submarining risk in a simplified human body model. Comput Methods Biomech Biomed Engin pp 1–12, doi:10.1080/10255842.2023.2165879

Go LS (2021) Non-Intrusive Model Order Reduction Approaches for Crash Applications. Master's thesis, Technical University of Munich, Munich, Germany

Göhler MS, Eifler T, Howard TJ (2016) Robustness Metrics: Consolidating the Multiple Approaches to Quantify Robustness. J Mech Des 138(111407), doi:10.1115/1.4034112

Golub GH, Van Loan CF (2013) Matrix Computations, 4th edn. The Johns Hopkins University Press, Baltimore, Maryland, USA

González I, Valdebenito M, Correa J, Jensen H (2019) Calculation of second order statistics of uncertain linear systems applying reduced order models. Reliab Eng Syst Saf 190:106514, doi:10.1016/j.ress.2019.106514

Gorodetsky AA, Geraci G, Eldred MS, Jakeman JD (2020) A generalized approximate control variate framework for multifidelity uncertainty quantification. J Comput Phys 408:109257, doi:10.1016/j.jcp.2020.109257

Gratiet LL (2012) Recursive co-kriging model for Design of Computer experiments with multiple levels of fidelity with an application to hydrodynamic. Int J Uncertain Quantif 4(5):365–386, doi:10.1615/Int.J.UncertaintyQuantification.2014006914

Grigoriu M (2002) Stochastic Calculus: Application in Science and Engineering. Springer Science+Business Media, LLC, New York, NY, USA, doi:10.1007/978-0-8176-8228-6

Guo M, Hesthaven JS (2017) Reduced order modeling for nonlinear structural analysis using Gaussian process regression. Comput Methods Appl Mech Eng 341:807–826, doi:10.1016/j.cma.2018.07.017

Guo M, Hesthaven JS (2019) Data-driven reduced order modeling for time-dependent problems. Comput Methods Appl Mech Eng 345:75–99, doi:10.1016/j.cma.2018.10.029

Guo M, Manzoni A, Amendt M, Conti P, Hesthaven JS (2022) Multi-fidelity regression using artificial neural networks: Efficient approximation of parameter-dependent output quantities. Comput Methods Appl Mech Eng 389(February), doi:10.1016/j.cma.2021.114378

Han ZH, Görtz S (2012) Hierarchical kriging model for variable-fidelity surrogate modeling. AIAA J 50(9):1885–1896, doi:10.2514/1.J051354

Harzheim L (2014) Strukturoptimierung : Grundlagen und Anwendungen, 2nd edn. Europa Lehrmittel, Berlin, Germany

Hernández J (2020) A multiscale method for periodic structures using domain decomposition and ECM-hyperreduction. Comput Methods Appl Mech Eng 368:113192, doi:10.1016/j.cma.2020.113192

Hernández J, Caicedo M, Ferrer A (2017) Dimensional hyper-reduction of nonlinear finite element models via empirical cubature. Comput Methods Appl Mech Eng 313:687–722, doi:10.1016/j.cma.2016.10.022

Hesthaven JS, Pagliantini C, Rozza G (2022) Reduced basis methods for time-dependent problems. Acta Numer 31(June):265–345, doi:10.1017/S0962492922000058

Hu C, Huang G, Li C (2021) Experimental and Numerical Study of Low-Velocity Impact and Tensile after Impact for CFRP Laminates Single-Lap Joints Adhesively Bonded Structure. Materials (Basel) 14(4):1016, doi:10.3390/ma14041016

Huang B, Du X (2007) Analytical robustness assessment for robust design. Struct Multidiscip Optim 34(2):123–137, doi:10.1007/s00158-006-0068-0

Isaksson T (1999) Modelling the Variability of Bending Strength in Structural Timber. PhD thesis, Lund University, Lund, Sweden

Iwamoto M, Kisanuki Y, Watanabe I, Furusu K, Miki K (2002) Development of a finite element model of the total human model for. IRCOBI Conf pp 31–42

Jurecka F (2007) Robust Design Optimization Based on Metamodeling Techniques. PhD thesis, Technical University of Munich, Munich, Germany

Kandler G, Füssl J (2017) A probabilistic approach for the linear behaviour of glued laminated timber. Eng Struct 148:673–685, doi:10.1016/j.engstruct.2017.07.017

Kandler G, Füssl J, Eberhardsteiner J (2015) Stochastic finite element approaches for wood-based products: theoretical framework and review of methods. Wood Sci Technol 49(5):1055–1097, doi:10.1007/s00226-015-0737-5

Kandler G, Lukacevic M, Zechmeister C, Wolff S, Füssl J (2018) Stochastic engineering framework for timber structural elements and its application to glued laminated timber beams. Constr Build Mater 190:573–592, doi:10.1016/j.conbuildmat.2018.09.129

Kaps A, Czech C, Duddeck F (2022) A hierarchical kriging approach for multi-fidelity optimization of automotive crashworthiness problems. Struct Multidiscip Optim 65(4):114, doi:10.1007/s00158-022-03211-2

Kast M, Guo M, Hesthaven JS (2020) A non-intrusive multifidelity method for the reduced order modeling of nonlinear problems. Comput Methods Appl Mech Eng 364, doi:10.1016/j.cma.2020.112947

Kennedy MC, O'Hagan A (2000) Predicting the output from a complex computer code when fast approximations are available. Biometrika 87(1):1–13, doi:10.1093/biomet/87.1.1

Khaloian Sarnaghi A, van de Kuilen JW (2019) Strength prediction of timber boards using 3D FE-analysis. Constr Build Mater 202:563–573, doi:10.1016/j.conbuildmat.2019.01.032

Khatouri H, Benamara T, Breitkopf P, Demange J (2022) Metamodeling techniques for CPU-intensive simulation-based design optimization: a survey. Adv Model Simul Eng Sci 9(1):1–31, doi:10.1186/s40323-022-00214-y

Kilimtzidis S, Kotzakolios A, Kostopoulos V (2023) Efficient structural optimisation of composite materials aircraft wings. Compos Struct 303:116268, doi:10.1016/j.compstruct.2022.116268

Klinke N, Schumacher A (2018) Parameterization Setup for Metamodel Based Optimizations of Tailor Rolled Blanks. Adv Struct Multidiscip Optim 1:1833–1850, doi:10.1007/978-3-319-67988-4_137

Kneifl J, Grunert D, Fehr J (2021) A nonintrusive nonlinear model reduction method for structural dynamical problems based on machine learning. Int J Numer Methods Eng pp 1–13, doi:10.1002/nme.6712

Knight NF (2006) User-Defined Material Model for Thermo-mechanical Progressive Failure Analysis. Tech. rep., NASA Langley Research Center, NASA Langley Research Center, Hampton, VA, USA

Kochenderfer MJ, Wheeler TA (2019) Algorithms for Optimization. The MIT press, Cambridge, Massachusetts, USA, doi:10.1109/MCS.2019.2961589

Komeilizadeh K, Kaps A, Duddeck F (2023) Isovolumetric adaptations to space-filling design of experiments. Optim Eng 24(2):1267–1288, doi:10.1007/s11081-022-09731-6

Kutz JN, Brunton SL, Brunton BW, Proctor JL (2016) Dynamic Mode Decomposition. Society for Industrial and Applied Mathematics, Philadelphia, PA, USA, doi:10.1137/1.9781611974508

Lee J, Cho M (2018) Efficient design optimization strategy for structural dynamic systems using a reduced basis method combined with an equivalent static load. Struct Multidiscip Optim 58(4):1489–1504, doi:10.1007/s00158-018-1976-5

Lee K, Carlberg KT (2020) Model reduction of dynamical systems on nonlinear manifolds using deep convolutional autoencoders. J Comput Phys 404, doi:10.1016/j.jcp.2019.108973

Leichsenring F, Jenkel C, Graf W, Kaliske M (2018) Numerical simulation of wooden structures with polymorphic uncertainty in material properties. Int J Reliab Saf 12(1-2):24–45, doi:10.1504/IJRS.2018.092499

Li CC, Der Kiureghian A (1993) Optimal Discretization of Random Fields. J Eng Mech 119(6):1136–1154

Li J, Cai J, Qu K (2018) Adjoint-based two-step optimization method using proper orthogonal decomposition and domain decomposition. AIAA J 56(3):1133–1145, doi:10.2514/1.J055773

Lloret-Cabot M, Fenton GA, Hicks MA (2014) On the estimation of scale of fluctuation in geostatistics. Georisk 8(2):129–140, doi:10.1080/17499518.2013.871189

Lu C, Zhu X (2021) Bifidelity Data-Assisted Neural Networks in Nonintrusive Reduced-Order Modeling. J Sci Comput 87(1):8, doi:10.1007/s10915-020-01403-w

Lu L, Pestourie R, Johnson SG, Romano G (2022) Multifidelity deep neural operators for efficient learning of partial differential equations with application to fast inverse design of nanoscale heat transport. Phys Rev Res 4(2):023210, doi:10.1103/PhysRevResearch.4.023210

Lüders C (2020) Nonlinear-Elastic Orthotropic Material Modeling of an Epoxy-Based Polymer for Predicting the Material Behavior of Transversely Loaded Fiber-Reinforced Composites. J Compos Sci 4(2):46, doi:10.3390/jcs4020046

Lukacevic M, Kandler G, Hu M, Olsson A, Füssl J (2019) A 3D model for knots and related fiber deviations in sawn timber for prediction of mechanical properties of boards. Mater Des 166:107617, doi:10.1016/j.matdes.2019.107617

Luo Y, Zhan J, Xing J, Kang Z (2019) Non-probabilistic uncertainty quantification and response analysis of structures with a bounded field model. Comput Methods Appl Mech Eng 347:663–678, doi:10.1016/j.cma.2018.12.043

Mataix Ferrándiz V, Bucher P, Rossi R, Cotela J, Carbonell JM, Zorrilla R, ... Tosi R (2020) KratosMultiphysics (Version 8.1). Zenodo doi:10.5281/zenodo.3234644

Messmer M (2020) Uncertainty Quantification in Structural Stability Analysis using Monte Carlo Method. Master's thesis, Technical University of Munich, Munich, Germany

Mirsky L (1960) Symmetric gauge functions and unitarily invariant norms. Q J Math 11(1):50–59, doi:10.1093/qmath/11.1.50

Montáns FJ, Chinesta F, Gómez-Bombarelli R, Kutz JN (2019) Data-driven modeling and learning in science and engineering. Comptes Rendus Mécanique 347(11):845–855, doi:10.1016/j.crme.2019.11.009

Murphy R, Imediegwu C, Hewson R, Santer M (2021) Multiscale structural optimization with concurrent coupling between scales. Struct Multidiscip Optim 63(4):1721–1741, doi:10.1007/s00158-020-02773-3

NASA (2022) Common Research Model, accessed 28.05.2023. URL https://commonresearchmodel.larc.nasa.gov/

Ng LWT, Willcox KE (2014) Multifidelity approaches for optimization under uncertainty. Int J Numer Methods Eng 100(10):746–772, doi:10.1002/nme.4761

Niemz P, Soneregger WU (2017) Holzphysik: Physik der Holzes und der Holzwerkstoffe. Fachbuchverlag Leipzig im Carl Hanser Verlag, München, doi:10.3139/9783446445468

Nurtaj Hossain M, Ghosh D (2020) Adaptive reduced order modeling for nonlinear dynamical systems through a new a posteriori error estimator: Application to uncertainty quantification. Int J Numer Methods Eng 121(15):3417–3441, doi:10.1002/nme.6365

Oguz EA, Huvaj N, Griffiths DV (2019) Vertical spatial correlation length based on standard penetration tests. Mar Georesources Geotechnol 37(1):45–56, doi:10.1080/1064119X.2018.1443180

Oller S, Oñate E, Miquel J, Botello S (1996) A plastic damage constitutive model for composite materials. Int J Solids Struct 33(17):2501–2518, doi:10.1016/0020-7683(95)00161-1

Oxberry GM, Kostova-Vassilevska T, Arrighi W, Chand K (2017) Limited-memory adaptive snapshot selection for proper orthogonal decomposition. Int J Numer Methods Eng 109(2):198–217, doi:10.1002/nme.5283

Papaioannou I (2020) Stochastic Finite Element Method, Script. Technische Universität München, Munich, Germany

Partin L, Geraci G, Rushdi AA, Eldred MS, Schiavazzi DE (2023) Multifidelity data fusion in convolutional encoder/decoder networks. J Comput Phys 472:111666, doi:10.1016/j.jcp.2022.111666

Peherstorfer B, Willcox K (2016) Data-driven operator inference for nonintrusive projection-based model reduction. Comput Methods Appl Mech Eng 306(July):196–215, doi:10.1016/j.cma.2016.03.025

Peherstorfer B, Butnaru D, Willcox K, Bungartz HJ (2014) Localized Discrete Empirical Interpolation Method. SIAM J Sci Comput 36(1):A168–A192, doi:10.1137/130924408

Peherstorfer B, Willcox K, Gunzburger M (2016) Optimal Model Management for Multifidelity Monte Carlo Estimation. SIAM J Sci Comput 38(5):A3163–A3194, doi:10.1137/15M1046472

Peherstorfer B, Willcox K, Gunzburger M (2018) Survey of multifidelity methods in uncertainty propagation, inference, and optimization. SIAM Rev 60(3):550–591, doi:10.1137/16M1082469

Phalippou P, Bouabdallah S, Breitkopf P, Villon P, Zarroug M (2020) Sparse POD modal subsets for reduced-order nonlinear explicit dynamics. Int J Numer Methods Eng 121(4):763–777, doi:10.1002/nme.6243

Pretsch L, Arsenyev I, Czech C, Duddeck F (2023) Interdisciplinary design optimization of compressor blades combining low- and high-fidelity models. Struct Multidiscip Optim 66(4):70, doi:10.1007/s00158-023-03516-w

Rais A, Bacher M, Khaloian-Sarnaghi A, Zeilhofer M, Kovryga A, Fontanini F, Hilmers T, Westermayr M, Jacobs M, Pretzsch H, van de Kuilen JW (2021) Local 3D fibre orientation for tensile strength prediction of European beech timber. Constr Build Mater 279, doi:10.1016/j.conbuildmat.2021.122527

Rasmussen CE, Williams CK (2006) Gaussian Processes for Machine Learning. The MIT press, Cambridge, Massachusetts, USA

Reid J (2000) Crash box LS-Dyna simulation, accessed 17.01.22. URL https://www.dynaexamples.com/introduction/intro-by-j.-reid/crashbox

Rocha I, van der Meer F, Sluys L (2020) An adaptive domain-based POD/ECM hyper-reduced modeling framework without offline training. Comput Methods Appl Mech Eng 358:112650, doi:10.1016/j.cma.2019.112650

Rutzmoser JJB (2018) Model Order Reduction for Nonlinear Structural Dynamics Simulation-free Approaches. PhD thesis, Technical University of Munich, Munich, Germany

Ryckelynck D (2009) Hyper-reduction of mechanical models involving internal variables. Int J Numer Methods Eng 77(1):75–89, doi:10.1002/nme.2406

Sandhaas C, Van De Kuilen JW (2013) Material model for wood. Heron 53(2-3):179–200

Scheffold D, Bach C, Duddeck F, Müller G, Buchschmid M (2018) Vibration Frequency Optimization of Jointed Structures with Contact Nonlinearities using Hyper-Reduction. IFAC-PapersOnLine 51(2):843–848, doi:10.1016/j.ifacol.2018.04.019

Schietzold FN, Graf W, Kaliske M (2018) Polymorphic Uncertainty Modeling for Optimization of Timber Structures. PAMM 18(1):1–4, doi:10.1002/pamm.201800426

Schietzold FN, Schmidt A, Dannert MM, Fau A, Fleury RM, Graf W, Kaliske M, Könke C, Lahmer T, Nackenhorst U (2019) Development of fuzzy probability based random fields for the numerical structural design. GAMM Mitteilungen 42(1):1–19, doi:10.1002/gamm.201900004

Scikit-learn (2022) Python library, accessed 28.02.22. URL https://scikit-learn.org

SciPy (2022) Python library, accessed 28.02.22. URL https://scipy.org/

Seeber F, Khaloian-Sarnaghi A, Rais A, van de Kuilen JW (2023) A numerical strength prediction approach for wood using element-wise local fiber directions from laser scanning. Mater Des 226(January):111578, doi:10.1016/j.matdes.2022.111578

Sella V, Pham J, Chaudhuri A, Willcox KE (2023) Projection-based multifidelity linear regression for data-poor applications. In: AIAA SCITECH 2023 Forum, American Institute of Aeronautics and Astronautics, Reston, Virginia, February, doi:10.2514/6.2023-0916

Sirovich L (1987) Turbulence and the dynamics of coherent structures. I. Coherent structures. Q Appl Math 45(3):561–571, doi:10.1090/qam/910462

Snelson E, Ghahramani Z (2005) Sparse Gaussian Processes using. In: Weiss Y, Platt J, Schölkopf B (eds) Adv. Neural Inf. Process. Syst., MIT Press, vol 18, URL http://www.gatsby.ucl.ac.uk/$\sim$snelson/SPGP_up.pdf

Soize C, Farhat C (2017) A nonparametric probabilistic approach for quantifying uncertainties in low-dimensional and high-dimensional nonlinear models. Int J Numer Methods Eng 109(6):837–888, doi:10.1002/nme.5312

Song DH, Tartakovsky DM (2021) Transfer Learning on Multi-Fidelity Data. J Mach Learn Model Comput 3(1):31–47, doi:10.1615/JMachLearnModelComput.2021038925

Storn R, Price K (1997) Differential Evolution - A Simple and Efficient Heuristic for Global Optimization over Continuous Space. J Glob Optim 11:341 –359, doi:10.1023/A:1008202821328

Sudret B, Der Kiureghian A (2000) Stochastic Finite Element Methods and Reliability: A State-of-the-Art Report. Tech. rep., Department of Civil and Environmental Engineering, Univ. of California, Berkeley, USA

Sullivan T (2015) Introduction to Uncertainty Quantification, Texts in Applied Mathematics, vol 63. Springer International Publishing, Switzerland, doi:10.1007/978-3-319-23395-6

Sun G, Zhang H, Fang J, Li G, Li Q (2017) Multi-objective and multi-case reliability-based design optimization for tailor rolled blank (TRB) structures. Struct Multidiscip Optim 55(5):1899–1916, doi:10.1007/s00158-016-1592-1

Swischuk R, Mainini L, Peherstorfer B, Willcox K (2019) Projection-based model reduction: Formulations for physics-based machine learning. Comput Fluids 179:704–717, doi:10.1016/j.compfluid.2018.07.021

Tao J, Sun G (2019) Application of deep learning based multi-fidelity surrogate model to robust aerodynamic design optimization. Aerosp Sci Technol 92:722–737, doi:10.1016/j.ast.2019.07.002

Tiso P, Rixen DJ (2013) Discrete Empirical Interpolation Method for Finite Element Structural Dynamics. In: Kerschen G, Adams D, Carrella A (eds) Top. Nonlinear Dyn. Vol. 1. Conf. Proc. Soc. Exp. Mech. Ser., vol 35, Springer, New York, NY, USA, pp 203–212, doi:10.1007/978-1-4614-6570-6_18

TNA ESWIRP ETW (2014) European Strategic Wind Tunnels Improved Research Potential, accessed 28.05.23. URL https://w3.onera.fr/ESWIRP-TNA-ETW-CRM-2014/

Toal DJJ (2014) On the Potential of a Multi-Fidelity G-POD Based Approach for Optimization and Uncertainty Quantification. In: Vol. 2B Turbomach., American Society of Mechanical Engineers, doi:10.1115/GT2014-25184

Touzé C, Vizzaccaro A, Thomas O (2021) Model order reduction methods for geometrically nonlinear structures: a review of nonlinear techniques. Nonlinear Dyn 105(2):1141–1190, doi:10.1007/s11071-021-06693-9

Ullah S, Wang H, Menzel S, Sendhoff B, Bäck T (2022) A Systematic Approach to Analyze the Computational Cost of Robustness in Model-Assisted Robust Optimization. In: Rudolph G, Kononova AV, Aguirre H, Kerschke P, Ochoa G, Tušar T (eds) Parallel Probl. Solving from Nat. – PPSN XVII. PPSN 2022. Lect. Notes Comput. Sci., vol 13398, Springer, Cham, Switzerland, doi:10.1007/978-3-031-14714-2_5

Uriot J, Potier P, Baudrit P, Trosseille X, Petit P, Richard O, Compigne S, Masuda M, Douard R (2015) Reference PMHS Sled Tests to Assess Submarining. In: SAE Tech. Pap., (No. 2015-22-0008). SAE Technical Paper, November, doi:10.4271/2015-22-0008

Vanmarcke EH (2010) Random Fields: Analysis and Synthesis. World Scientific Publishing Co. Pte. Ltd., Singapore

Vassberg J, DeHaan M, Rivers M, Wahls R (2008) Development of a Common Research Model for Applied CFD Validation Studies. 26th AIAA Appl Aerodyn Conf doi:10.2514/6.2008-6919

Vlachas K, Tatsis K, Agathos K, Brink AR, Chatzi E (2021) A local basis approximation approach for nonlinear parametric model order reduction. J Sound Vib 502:116055, doi:10.1016/j.jsv.2021.116055, 2003.07716

Weißinger P (2023) Robust design optimization employing multi-fidelity reduced order models. Master's thesis, Technical University of Munich, Munich, Germany

Wen T, Zahr MJ (2023) A globally convergent method to accelerate large-scale optimization using on-the-fly model hyperreduction: Application to shape optimization. J Comput Phys 484:112082, doi:10.1016/j.jcp.2023.112082

Willcox K (2006) Unsteady flow sensing and estimation via the gappy proper orthogonal decomposition. Comput Fluids 35(2):208–226, doi:10.1016/j.compfluid.2004.11.006

Wriggers P (2008) Nichtlineare Finite-Element-Methoden. Springer, Berlin, Germany, doi:10.1007/978-3-642-56865-7

Wu SR, Gu L (2012) Introduction to the Explicit Finite Element Method for Nonlinear Transient Dynamics. John Wiley & Sons, Inc., Hoboken, New Jersey, USA, doi:10.1002/9781118382011

Xiao D, Fang F, Pain C, Hu G (2015) Non-intrusive reduced-order modelling of the Navier-Stokes equations based on RBF interpolation. Int J Numer Methods Fluids 79(11):580–595, doi:10.1002/fld.4066

Xu F, Sun G, Li G, Li Q (2014) Experimental study on crashworthiness of tailor-welded blank (TWB) thin-walled high-strength steel (HSS) tubular structures. Thin-Walled Struct 74:12–27, doi:10.1016/j.tws.2013.08.021

Yu J, Yan C, Guo M (2019) Non-intrusive reduced-order modeling for fluid problems: A brief review. Proc Inst Mech Eng Part G J Aerosp Eng 233(16):5896–5912, doi:10.1177/0954410019890721

Yu T, Khaloian A, van de Kuilen JW (2022) An improved model for the time-dependent material response of wood under mechanical loading and varying humidity conditions. Eng Struct 259:114116, doi:10.1016/j.engstruct.2022.114116

Zahr MJ, Farhat C (2015) Progressive construction of a parametric reduced-order model for PDE-constrained optimization. Int J Numer Methods Eng 102(5):1111–1135, doi:10.1002/nme.4770

Zahr MJ, Avery P, Farhat C (2017) A multilevel projection-based model order reduction framework for nonlinear dynamic multiscale problems in structural and solid mechanics. Int J Numer Methods Eng 112(8):855–881, doi:10.1002/nme.5535

Zahr MJ, Carlberg KT, Kouri DP (2019) An efficient, globally convergent method for optimization under uncertainty using adaptive model reduction and sparse grids. SIAM-ASA J Uncertain Quantif 7(3):877–912, doi:10.1137/18M1220996

Zhang J (2021) Modern Monte Carlo methods for efficient uncertainty quantification and propagation: A survey. Wiley Interdiscip Rev Comput Stat 13(5):1–23, doi:10.1002/wics.1539

Zhu C, Byrd RH, Lu P, Nocedal J (1997) Algorithm 778: L-BFGS-B: Fortran Subroutines for Large-Scale Bound-Constrained Optimization. ACM Trans Math Softw 23(4):550–560, doi:10.1145/279232.279236

Zimmermann R (2021) 7 Manifold interpolation. In: Syst. Data-Driven Methods Algorithms, Walter de Gruyter GmbH, Berlin/Boston, pp 229–274, doi:10.1515/9783110498967-007